

**Development of tools to study human hair follicle biology  
in vitro - focus on hair follicle stem cells and their potential  
application in Vitiligo therapy**

**Maria Marques Adegas Bairrão Henriques**

Thesis to obtain the Master of Science Degree in

**Biomedical Engineering**

Supervisor(s): Professor João António Augusto Ferreira and Professor Cláudia  
Alexandra Martins Lobato da Silva

**Examination Committee**

Chairperson: Professor João Pedro Estrela Rodrigues Conde

Supervisor: Professor João António Augusto Ferreira

Members of the Committee: Doctor José Miguel Rino Henriques

**November 2017**



# Acknowledgments

I would like to start by thanking to Professor Joaquim Cabral for giving me the opportunity to developing my master thesis in Instituto de Medicina Molecular/IMM- João Lobo Antunes, in collaboration with the Stem Cell Bioengineering and Regenerative Medicine Laboratory at Instituto Superior Técnico campus of Tagus Park.

I would like to thank to my supervisors Professor João Ferreira, Professor Cláudia Lobato da Silva and Professor Paulo Filipe. Professor João Ferreira for teaching and guiding me throughout this 9 months. Thank you for all the availability on discussing the project, clarifying doubts and helping me find ways to enrich my work. Professor Cláudia Lobato da Silva thank you for all the guidance, sympathy and immediate availability when I needed. Professor Paulo Filipe, thank you for all the advices and readiness of obtaining the biopsies needed during the project.

I also would like to thank some people that I have had the pleasure to meet during my research internship. Dr. Daniela Cunha, for all the kindness and helpful discussions about the project. Members of Bioimaging Facility, for the time spent with me and all the useful suggestions. Pedro Fonseca, for the friendship and help whenever I needed.

I am truly grateful to my parents, for all the unconditional support during all my life and for giving me the opportunity to become Biomedical Engineer. Your strength and motivation was crucial. I also would like to thank to my brothers, Manel and Pedro, for all the patience with me, for cooking me dinner when my time was scarce, for the friendship and for all silly thinks at the right moments.

I would like to thank my grandparents, uncles and cousins for always believing in me, and my friends from Ponte de Sor for listening and always be there for me no matter what. Also, to my IST friends, thank you for all the endless help, friendship and for making this 5 years much more amazing.

Lastly, my acknowledgements also go to Serviço de Dermatologia, Hospital de Santa Maria (Lisbon), and Serviço de Dermatologia, Hospital CUF Descobertas (Lisbon), for the collaboration with this project.



# Abstract

The study of human hair follicle (HF) dynamics is a key point to find more effective treatments for skin disorders such as Vitiligo. Human HF cycle and skin stem cells are a particularly interesting field, since HFs cycle continuously and stem cells have a crucial role in this phenomenon. Most of the studies addressing HF dynamics were performed in animals, so these results cannot be directly translated to humans. The present master thesis aims to contributing to fill-in this gap through the development of tools to study human HF biology. In this context, a tool for cell cycle quantification using microscopy was successfully developed using HCT-116 cells exposed to 5-Ethynyl-2'-deoxyuridine (EdU), whose signal was measured using *CellProfiler* software. S-phase was estimated to last 6/7h, G1-phase 4/5h and G2-phase 4/5h. Additionally, a method for analyzing human HF dynamics was established and EdU-positive cells were quantified in diverse HF regions. As expected, the bulb region showed the highest labeling index, but replication in outer root sheath cells was also documented and quantified. Lastly, the initial steps to obtain isolated HF stem cells were also performed. The protocol for obtaining HF epithelial cell suspensions from human biopsies was established after an optimization process, with CnT-07 medium proving appropriate for culture of these cells. The tools developed in this master thesis will be used in the future to pursue our aim of implementing cell therapies for patients suffering from Vitiligo.

**Keywords:** Skin stem cells; Cell cycle; Hair follicle; Proliferation; Microscopy



# Resumo

O estudo da dinâmica do folículo piloso (FP) é um tema chave na procura de tratamentos eficazes para doenças de pele, como Vitiligo. Particularmente, o ciclo do FP e as células estaminais da pele constituem uma área de interesse pois estas células têm um papel fundamental nesse evento. A maioria dos estudos nesta área foram realizados em animais, logo os seus resultados não podem ser diretamente transpostos para a espécie humana. A presente dissertação tem como objetivo contribuir para o aumento de conhecimento nesta área, através do desenvolvimento de ferramentas para estudar a biologia do FP humano. Nomeadamente, foi desenvolvida com sucesso uma ferramenta para quantificação do ciclo celular através de microscopia, usando células HCT-116 expostas a 5-Ethynyl-2'-deoxyuridine (EdU), cujo sinal foi medido através do software *CellProfiler*. Estimaram-se durações de 6/7h, 4/5h e 4/5h para as fases S, G1 e G2 respectivamente. Além disso, foi desenvolvido um método para analisar as dinâmicas do FP humano, onde as células EdU positivas foram quantificadas em diversas regiões. Como era esperado, a região do bulbo apresentou o maior numero de células EdU positivas, apesar de também se ter documentado replicação na bainha externa. Por fim, o isolamento das células estaminais foi iniciado. O protocolo para a obtenção da suspensão de células do FP foi estabelecido após um processo de otimização, concluindo-se que o meio de cultura mais adequado é o CnT-07. As ferramentas desenvolvidas nesta dissertação poderão ser usadas no futuro para implementar terapias celulares eficazes em pacientes com Vitiligo.

**Palavras Chave:** *Células estaminais da pele; Ciclo celular; Folículo piloso; Proliferação; Microscopia.*



# Table of Contents

<b>Acknowledgments .....</b>	<b>iii</b>
<b>Abstract .....</b>	<b>v</b>
<b>Resumo.....</b>	<b>vii</b>
<b>Table of Contents .....</b>	<b>ix</b>
<b>List of figures.....</b>	<b>xiii</b>
<b>List of Tables.....</b>	<b>xvii</b>
<b>List of Abbreviations .....</b>	<b>xix</b>
<b>I. Introduction .....</b>	<b>1</b>
I.1. Skin Disorders – Vitiligo.....	1
I.1.1. Pathophysiology .....	1
I.1.2. Treatments.....	3
I.1.2.1. Topical therapies: corticosteroids and calcineurin inhibitors.....	3
I.1.2.2. Phototherapies.....	3
I.1.2.2.1. Photochemotherapies (PUVA and KUVA) .....	4
I.1.2.2.2. Narrow Band (NB) - UVB and target phototherapies .....	5
I.1.2.2.3. Oral treatments.....	5
I.1.2.2.4. Surgical treatments.....	6
I.2. Skin.....	6
I.2.1. Anatomy.....	6
I.2.1.1. Epidermis.....	6
I.2.1.2. Dermis and Hypodermis .....	7
I.2.1.3. Skin Appendages: Hair follicles .....	8
I.2.2. Hair follicle morphogenesis and cycle .....	8
I.2.3. Skin Stem Cells .....	10
I.2.3.1. Epidermal Stem Cells .....	10
I.2.3.2. Epithelial stem cells .....	11
I.2.3.3. Melanocyte Stem Cells .....	11
I.3. Useful tools for human hair follicle characterization .....	12

I.3.1.	Markers .....	12
I.3.1.1.	Cytokeratins .....	12
I.3.1.2.	CD-Markers .....	13
I.3.1.3.	Other markers .....	13
I.3.2.	Cell cycle Dynamics .....	14
I.3.2.1.	Cell cycle - background .....	14
I.3.2.2.	Cell cycle quantification .....	15
I.3.2.3.	Quantification of cell cycle using Flow Cytometry vs Microscopy .....	16
I.3.2.3.1.	Widefield Fluorescent Microscopy, Point Scanning Confocal Microscopy and Spinning Disk Confocal Microscopy .....	16
I.3.2.4.	Cell cycle dynamics of hair follicle cells .....	18
I.4.	Isolation of Hair Follicle Stem Cells and their application on Vitiligo therapy .....	20
<b>II.</b>	<b>Aims of the study and Motivation .....</b>	<b>23</b>
<b>III.</b>	<b>Materials and Methods .....</b>	<b>25</b>
III.1.	Cell cycle quantification using 5-Ethynyl-2'-deoxyuridine (EdU) .....	25
III.1.1.	Cell culture .....	25
III.1.2.	EdU incorporation .....	26
III.1.3.	EdU staining (EdU detection system) .....	26
III.1.4.	Whole DNA staining .....	27
III.1.4.1.	Propidium Iodine .....	27
III.1.5.	Image acquisition using Widefield Fluorescence Microscopy .....	28
III.1.6.	Image acquisition using SD confocal microscopy .....	30
III.1.7.	CellProfiler software and RStudio for image analysis .....	30
III.1.7.1.	CellProfiler Project 1 - Measuring intensity of EdU-positive cells .....	31
III.1.7.2.	CellProfiler Project 2 - Measuring intensity of EdU negative cells .....	33
III.1.7.2.1.	Preliminary Project .....	33
III.1.7.2.2.	Main Projects .....	35
III.1.7.3.	RStudio .....	37
III.1.8.	Statistical analysis .....	37
III.2.	Hair follicle characterization .....	38
III.2.1.	EdU incorporation .....	38

III.2.2.	Preparation of samples, inclusion and sectioning .....	38
III.2.3.	EdU staining and Immunofluorescence.....	39
III.2.4.	Image acquisition using Confocal Point-Scanning Microscopy.....	39
III.2.5.	Image analysis and quantification using Fiji .....	40
III.2.6.	Orcein-Gimsa protocol.....	40
III.2.7.	Statistical analysis .....	40
III.3.	Preparation of hair follicle cell suspension from human biopsies.....	41
<b>IV. Results and Discussion .....</b>	<b>43</b>	
IV.1.	Cell cycle quantification using Microscopy .....	43
IV.1.1.	Outline .....	43
IV.1.2.	Experiments sum-up.....	44
IV.1.2.1.	Estimation of S phase duration time.....	45
IV.1.2.2.	Estimation of G1 and G2 phases duration times.....	49
IV.1.2.3.	Influence of cell number in the estimation of S phase duration time.....	55
IV.1.2.4.	Influence of cell number in the estimation of G1 and G2 duration time .....	56
IV.1.2.5.	Estimation of S phase duration time using SD confocal microscopy .....	58
IV.2.	Hair follicles characterization using EdU .....	60
IV.2.1.	Outline .....	60
IV.2.2.	Qualitative analysis.....	60
IV.2.3.	Quantitative analysis: Bulb and Sub-bulge.....	65
IV.3.	Preparation of hair follicle cell suspension from human biopsies – Initial work of isolation hair follicle stem cells .....	68
<b>V. Conclusions and Future Trends.....</b>	<b>71</b>	
<b>VI. References.....</b>	<b>75</b>	
<b>VII. Annexes .....</b>	<b>83</b>	



# List of figures

Figure I-1: Skin layers and appendages <sup>38</sup> .....	7
Figure I-2: (A) Hair follicle structure <sup>43</sup> (B) Hair follicle layers and sub-layers <sup>41</sup> . (APM: arrector pili muscle; DP: dermal papilla; m: matrix; HS: hair shaft, IRS: inner root sheath; ORS: outer root sheath; SG: sebaceous gland) .....	8
Figure I-3: Hair follicle morphogenesis and cycle. APM: arrector pili muscle; DC, dermal condensate; DP: dermal papilla; HS: hair shaft; IRS: inner root sheath; MC: melanocytes; ORS: outer root sheath; SC: sebocytes; SG: sebaceous gland <sup>41</sup> .....	9
Figure I-4: Regions of hair follicle ORS established by Ohyama and colleagues to characterize surface markers expression <sup>65</sup> .....	13
Figure I-5: Cell cycle of proliferating cells. (M: mitosis; G1: interphase or post-mitotic growth phase; S: DNA synthesis; G2: resting or pre-mitotic phase; G0: stem cells not proliferating (quiescence); D: cells differentiating) <sup>38</sup> .....	14
Figure I-6: Cell cycle curve, presenting G1 and G2 populations (G1 and G2 peaks, respectively) <sup>69</sup> ..	15
Figure I-7: Light paths of (A) standard widefield fluorescent microscopy <sup>77</sup> and (B) point scanning confocal microscopy <sup>79</sup> .....	17
Figure I-8: EdU incorporation (a) (b) (bii) alone and (c) double stain with pH3 or (d) (dii) Ki-67 <sup>67</sup> .....	19
Figure III-1: (A) Structure of 5-Ethynyl-2'-deoxyuridine (EdU); (B) Reaction between alkyne group of EdU and the fluorochrome-conjugated azide <sup>71</sup> .....	25
Figure III-2: EdU incorporation procedure in experiments with 8 time-points. Cells incorporated EdU for incremental periods of time, from 0h to 8h/10h. In this case, cells corresponding to time-point T8h were pulsed on 0h and incorporated EdU continuously for 8h. In contrast, T1h cells were just pulsed on 7h, incorporating EdU for 1h.....	26
Figure III-3: Excitation and emission spectra of Alexa Fluor 488, Hoechst 33342, and filtersets DAPI and HE GFP <sup>96</sup> .....	29
Figure III-4: Excitation and emission spectra of Alexa Fluor 488, PI, and filtersets DAPI and HE DsRed <sup>96</sup> . .....	29
Figure III-5: Excitation and emission spectra of Alexa Fluor 488, DAPI, and filtersets DAPI and HE GFP <sup>96</sup> .....	29
Figure III-6: Environment of <i>CellProfiler</i> Software.....	31
Figure III-7: Images Metadata.....	32
Figure III-8: Display window of IdentifyPrimaryObjects module. ....	34

Figure III-9 Zooms of figure III-9 with cells discarded: (A) in the borders outlined in yellow, and (B) based on size outlined in magenta. The values of intensities present in the bottom bar correspond to the pixels pointed out with the red crosses. In this example the threshold is 0.035, the pixel intensity in (A) is higher (0.0823 – classified as foreground), and the pixel intensity in (B) is lower (0,0153 – classified as background).....	34
Figure III-10: Display window of ImageMath Module – operation And.....	36
Figure IV-1: EdU incorporation principal <sup>100</sup> .....	45
Figure IV-2: (A) Widefield microscopy image of experiment 9 (T2h), containing EdU-positive cells. (B) Correspondent output image with EdU-positive cells identified, obtained after running project 1. Scale: 50 µm.....	46
Figure IV-3: Histogram fraction of cells vs EdU Integrated Intensities of time-point T4h, experiment 9. ....	46
Figure IV-4: Graph Cumulative fraction of cells vs EdU Integrated Intensity, time-point T4h, experiment 9.....	47
Figure IV-5: Maximum EdU Integrated Intensities along time-points (experiments 2, 4, 5, 6, 7, 9, 10 and 12). (A) Actual values of each experiment; (B) Average values (n=8); The tendency line (dashed line) represents the linear increase of maximum Integrated Intensity until T6h; Values displayed as mean ± standard deviation. ....	49
Figure IV-6: (A) Widefield microscopy image of experiment 7 (T7h), stained for Hoechst and EdU. (B)Correspondent output image obtained after running project 2. Scale: 50 µm.....	51
Figure IV-7: Histograms fraction of cells vs Integrated Intensity (T1h) of (A) experiment 7 (left image) and (B) experiment 8 (right image).....	51
Figure IV-8: Percentage of G2 cells in total population (%G2_tp) along time-points (experiments 7, 8 and 9). (A) Actual values of each experiment; (B) Average values (n=3); The tendency line (dashed line) represents the linear decrease of the percentage G2 cells in total population until T4h; Values displayed as mean ± standard deviation. ....	53
Figure IV-9: Percentage of G1 cells in total population (%G1_tp) vs time points (experiments 7, 8 and 9). (A) Actual values of each experiment; (B) Average values (n=3); The tendency line (dashed line) represents the linear decrease of the percentage of G1 cells in total population since T5h; Values displayed as mean ± standard deviation. ....	54
Figure IV-10: Percentage of (A) G2 and (B) G1 cells in total population (%G2_tp and %G1_tp) vs time points (experiments 11 and 12; n=3). Values displayed as mean ± standard deviation. ....	54
Figure IV-11: Maximum Integrated Intensity along time-points using different sets of input images (2, 4, 6, 9, 12 and 18 images) of experiment 4.....	55
Figure IV-12: Maximum Integrated Intensities along time-points and respective standard deviations (Experiments 13, 14 and 15; n=3). The tendency line (dashed blue line) represents the linear increase	

of maximum Integrated Intensity until T6h. Orange values highlight the stabilization trend. Values displayed as mean ± standard deviation .....	59
Figure IV-13: Hair follicle regions <sup>43</sup> . (APM: arrector pili muscle; DP: dermal papilla; m: matrix; HS: hair shaft, IRS: inner root sheath; ORS: outer root sheath; SG: sebaceous gland).....	61
Figure IV-14: Image of bulge region stained with Gimsa and acquired using the brightfield microscope Leica DM2500. Blue arrow represents the sebaceous gland, green arrow represents the arrector pili muscle and red arrows represent bulge ORS. Scale: 50µm.....	63
Figure IV-15: Labeling index (%) in the hair bulb (A) below AL, (B) above AL and (C) ORS of HFs #1, #2 and #3 (n=5, 4 and 5 respectively). Values displayed as mean ± standard deviation. ....	66
Figure IV-16: (A) Labeling Index (%) and (B) Number of EdU positive cells in 200 micrometers of the sub-bulge ORS, of HFs #1, #2 and #3 (n=20, 4 and 18 respectively). Values displayed as mean ± standard deviation. ....	67
Figure IV-17: Colony of epithelial cells formed after 9 days of culture. Image acquired using the Phase Contrast microscope Zeiss Primovert. Scale:50µm. ....	69
FigurVII-1: Graph containing the number of identified cells (EdU positive) along time-points, for each set of input images (2, 4, 6, 9, 12 and 18 images). ....	92
Figure VII-2: Images of hair follicle in catagen obtained on Confocal Point-Scanning Microscope Zeiss LSM 710. (A) represents the overwall structure (channel: DAPI). (B) an (C) represent bulge and bulb respectively (multichannel acquisition: DAPI and Alexa 488). The red crosses identifies EdU-positive cells. Scale: 50µm .....	95
Figure VII-3: Images of (A) epidermis and (B) HF bulge bulge stained with Gimsa and acquired using the brightfield microscope Leica DM2500. B) represents a para-sagital section of HF which do not contain dermal papilla. The melanin is present is localized on matrix Scale: 50µm. ....	95
Figure VII-4: Images of HFs stained with Gimsa and acquired using the brightfield microscope Leica DM2500. They present the endothelium destroyed by SDS when any protective structure as acrylamide was used. (A) epidermis; (B) bulb. Scale: 50µm. ....	96
Figure VII-5: Human hair follicles before (A) and after (B) collagenase/dispase incubation. Images acquired using the Phase Contrast microscope Zeiss Primovert. ....	97
Figure VII-6: R code .....	97



# List of Tables

Table III-1: Components to prepare the reaction cocktail, to a final volume of 500 $\mu$ L .....	27
Table III-2: Concentration of DNA stains.....	27
Table III-3: Wavelength ranges of excitation and emissions of filtersets on Zeiss Axio Observer <sup>98</sup> .....	28
Table III-4: Set of Analysis Modules. <sup>100</sup> .....	32
Table III-5: Main Settings of IdentifyPrimaryObjects module.....	32
Table III-6: Sum-up of Inputs and Outputs used in each Module of Main project - part 1.....	36
Table III-7: Functions used to establish the inputs .....	37
Table IV-1: Experiments sum-up. ....	44
Table IV-2: Frequencies of cells for each bin value present on: CellCycle_BinnedFrequencies_table.txt. ....	47
Table IV-3: Number of cells identified on T1h and T4h for each set of input images. ....	57
Table IV-4: Histograms (Fraction of cells vs Hoechst Integrated Intensity) of experiment T (T1h and T4h), for two sets of input images (12 and2 images).....	57
Table IV-5: Representative HF images of experiment 1 and 2 (columns) with merged channels, where blue fluorescence represent all nuclei (DAPI staining), green fluorescence represents replicating DNA (EdU staining) and red fluorescence represents bulge cells (CK-15 staining). Rows represent different anatomical regions (epidermis, supra-bulge, bulge, sub-bulge and bulb). Images were acquired in Confocal Microscope Zeiss LSM 710. Scale: 50 $\mu$ m.....	61
Table IV-6: EdU-positive cells (% or number) in HF regions obtained through quantification of n images. ....	67
Table VII-1: Values of threshold selected on Preliminary Project for DAPI or Hoechst channel (whole DNA stain) and Alexa 488 Channel .....	83
Table VII-2: Graphs fraction of cells vs EdU Integrated Intensity and cumulative fraction of cells vs EdU Integrated Intensity of each time-point (T1h-T8h), Experiment 9.....	84
Table VII-3: Graphs Maximum Integrated Intensity vs time-points of each experiment (1-12). ....	87
Table VII-4: Histograms (Fraction of cells vs DAPI Integrated Intensity) of each time-point (T1h-T8h), experiment 8 .....	88
Table VII-5: Histograms (Fraction of cells vs DAPI Integrated Intensity) of time-point (T9h-T10h), experiments 11 and 12 .....	90
Table VII-6: Range of G1 and G2 intensities selected based on histograms.....	90

Table VII-7: Sum-up of values used to estimate the percentage of G1 and G2 cells in total population.	91
Table VII-8: Number of identified cells (EdU positive) along time-points (rows), for each set of input images (columns; 2, 4, 6, 9, 12 and 18 images).	92
Table VII-9: Histograms (Fraction of cells vs Hoechst Integrated Intensity) of experiment 7 (T1h and T4h), for different sets of input images (2, 4, 6, 9, 12 images)	93
Table VII-10: Images exported from cell counter plugin of Fiji, where different types of counters (with different colors) were used to distinguish quantified areas and channels	96

# List of Abbreviations

<b>AL</b>	Auber's Line
<b>CK</b>	Cytokeratin
<b>DAPI</b>	4',6-Diamidino-2-Phenylindole
<b>DMSO</b>	Dimethylsulfoxide
<b>DOPA</b>	Dihidroxifenilalanina
<b>DP</b>	Dermal Papilla
<b>EdU</b>	5-Ethynyl-2'-deoxyuridine
<b>E-CFI</b>	EdU-coupled fluorescence intensity analysis
<b>eID</b>	experiment ID
<b>eSCs</b>	Epithelial Stem Cells
<b>FA</b>	formaldehyde
<b>FBS</b>	Foetal bovine serum
<b>HF</b>	Hair Follicle
<b>HFSCs</b>	Hair Follicle Stem Cells
<b>HVA</b>	Homovanillic acid
<b>LI</b>	Labeling index
<b>LRCs</b>	Label Retaining Cells
<b>MSCs</b>	Melanocytes Stem Cells
<b>NB</b>	Narrow Band
<b>NFAT</b>	Nuclear factor of activated T cells
<b>NSV</b>	Non-segmental Vitiligo
<b>PI</b>	Propidium Iodide
<b>PUVA</b>	Psoralens and Ultra Violet A
<b>SCF</b>	Stem cell factor
<b>SCs</b>	Stem Cells
<b>SD</b>	Spinning Disk
<b>SGs</b>	Sebaceous Glands

<b>SV</b>	Segmental Vitiligo
<b>TA</b>	Transit-amplifying
<b>VMA</b>	Vanillmandelic acid
<b>UV</b>	Ultraviolet

# I. Introduction

## I.1. Skin Disorders – Vitiligo

Vitiligo is a chronic pigmentary disorder which manifests as circumscribed white macules or patches in the skin and in mucous membranes, in areas where there was loss of melanocytes<sup>1</sup>.

This disorder is divided in two main classes: non-segmental Vitiligo (NSV) and segmental Vitiligo (SV). NSV is the most common. In NSV lesions are bilateral and can present an acrofacial pattern or can be symmetrical over the entire body, progressing in size over time. The lesions of SV are unilateral and segmental. This last class is characterized by an early age of onset and a fast stabilization<sup>2;3;1</sup>.

According to Vitiligo Global Issues Consensus Conference, besides NSV and SV, there are two more classes: Mixed Vitiligo (coexistence of NSV and SV) and Unclassified (cases that cannot be classified as NSV, SV or Mixed Vitiligo)<sup>2</sup>.

Vitiligo is considered progressive if during the observation period there are changes in the lesions or/and new lesions appear. Otherwise, vitiligo is considered stable<sup>4</sup>.

### I.1.1. Pathophysiology

Over time, several pathophysiological theories emerged, with the aim of explaining the cause of Vitiligo, and more specifically the loss of melanocytes<sup>1;5</sup>.

Strong evidence supports the autoimmune theory<sup>3;1</sup>. In 1992, Hann and colleagues studied the histology of skin biopsies taken from areas of active Vitiligo and observed clear infiltrations of lymphocytes in perilesional areas<sup>6</sup>. Later, in 1996, Le Poole and colleagues analyzed by immunohistochemistry the inflammatory infiltrations of perilesional skin biopsies from three Vitiligo patients. They verified an increase in the expression of interleukin-2 on perilesional areas of dermis, when compared to healthy controls. Interleukine-2 is a protein produced by helper T cells which acts as a general activator for proliferation of lymphocytes including resting T cells (both helper and cytotoxic cells). This evidence highlighted the possibility of an autoimmune reaction at the basis of Vitiligo<sup>7;8</sup>.

In 1995, Cui and co-workers studied the antibodies circulating in Vitiligo patients. These antibodies were mainly directed to antigens with 40-45, 75 and 90 kDa of molecular weight. They verified that those antibodies were quite frequent on Vitiligo patients: 83% of Vitiligo patients had antibodies to one or more of the antigens mentioned before compared to 7% in controls<sup>9</sup>. Even though most of the antigens were not specific for pigment cells, they were shown to be more toxic to melanocytes than to keratinocytes and fibroblasts<sup>1</sup>.

Another pathophysiological theory originated from the field of Genetics. In 1994, researchers studied 194 families, each one with an affected proband (first person of a family that participated in the research<sup>10</sup>), and verified that 20% of probands had at least one first-degree relative affected with Vitiligo<sup>11</sup>. Then, the study of the relationships between genetics and immune diseases followed. In 2003, Alkhateeb and colleagues analyzed the prevalence of several immune disorders in Vitiligo probands and in their first-degree relatives. In 1802 caucasian probands affected with Vitiligo, approximately 20% also presented autoimmune thyroid disease. This value is significantly higher than the population frequency of self-reported cases, that is approximately 2,4%. This evidence suggested etiologic links between immune disorders and a underlying genetic susceptibility to immunologic diseases<sup>1;12</sup>. This susceptibility was studied in 2010 by Jin and co-workers through genome-wide association studies. Researchers genotyped 579146 single-nucleotide polymorphisms in 1514 Vitiligo patients and compared with the genotypes of 2813 healthy people (controls). They verified associations between single-nucleotide polymorphisms of vitiligo patients at loci already associated to other autoimmune diseases, what corroborates the genetic susceptibility hypothesis mentioned before. Besides that, they verified associations at other loci, such as the locus of TYR. TYR is a gene which encodes tyrosinase, an enzyme which catalyses the rate-limiting steps of melanin biosynthesis<sup>3;13</sup>.

The neurohumoral hypothesis is another relevant theory which has been addressed experimentally. Since melanocytes derive from neural crest cells, a perturbation on the nervous system may affect these cells<sup>1</sup>. In 1992 Morrone and co-workers measured the levels of catecholamines from 24 hours urine samples of 150 Vitiligo patients and 50 healthy people. The levels of homovanillic acid (HVA) and vanillmandelic acid (VMA) were increased in Vitiligo patients. These overproduced catecholamines promote vasoconstriction, hypoxia and consequently the generation of oxygen radicals which are toxic to melanocytes<sup>3;14</sup>. Immunohistochemical studies, performed by Al' Abadie and colleagues in 1994, showed an increase of intra and perilesional neuropeptide Y, a neurotransmitter that can, as well, be cytotoxic to melanocytes<sup>1;15</sup>. In 2000, the levels of neuropeptide Y in Vitiligo patients were also analyzed by Lazarova and colleagues, through immunochemical techniques. Their findings corroborated the hypothesis of Al' Abadie, that neuropeptide Y can be considered a neurochemical marker in Vitiligo pathogenesis<sup>16</sup>.

Another theory, named Intrinsic theory, is related to the intrinsic defects detected on cells that can promote their death. The stem cell factor (SCF) has the role of regulating the growth and survival of melanocytes. During a study conducted in 2005 by Lee and colleagues, the levels of SCF expression were measured from unpigmented and pigmented epidermis of 19 Vitiligo patients. The levels of SCF in unpigmented epidermis were reduced when compared to the levels of SCF in pigmented epidermis. This reduction can be a cause of melanocyte death in Vitiligo patients<sup>17</sup>.

In fact, the exact cause(s) of Vitiligo remain(s) elusive. However, it is clear that these theories are not mutual exclusive. Further research is needed to understand the connections between all of them<sup>1;5</sup>.

## **I.1.2. Treatments**

The lack of information regarding the exact pathophysiology of Vitiligo makes the disease management harder. Nowadays, there are diverse types of treatment which can be applied, separately or combined, depending on factors as the type of Vitiligo, diseases state, medical history and psychological profile<sup>3</sup>.

The members of Vitiligo European Task Force and colleagues established the guidelines for Vitiligo management, based on evidence and on experts knowledge<sup>18</sup>.

### **I.1.2.1. Topical therapies: corticosteroids and calcineurin inhibitors**

Topical therapies are the first line of treatment. Both corticosteroids and calcineurin inhibitors are used as anti-inflammatory agents<sup>18</sup>. In general, corticoids can switch off inflammatory genes that are active during inflammation process, inhibiting the action of immune cells and most of the inflammatory process<sup>19;20</sup>. Calcinerium has a very important role in T-cell function, the dephosphorylation of nuclear factor of activated T cells (NFAT) transcription factor, which become active and translocate to the nucleus. In the nucleus, NFAT will change the transcription of target genes, as interleukin-2 upregulation. Calcineurin inhibitors are used to block this mechanism, in order to avoid the proliferation of immune cells<sup>21</sup>.

In 2010 one study conducted by Köse and colleagues tested the efficacy of topical mometasone cream and pimecrolimus cream on children with Vitiligo. The first one is a corticosteroid, while the second is a calcineurin inhibitor. Patients were divided in two groups, and each group applied one of the creams for 3 months. Researchers verified a reduction of the lesion sizes in both groups. More specifically, the rate of repigmentation in mometasone group was 65% and in pimecrolimus group was 42%<sup>22</sup>.

Along time, these studies have been shown that topical therapies promote skin repigmentation, however further studies need to be done in order to understand how to increase repigmentation ratios.

### **I.1.2.2. Phototherapies**

Phototherapies are the second line of treatment, and include ultraviolet (UV)-based therapy (UVA or UVB) and target phototherapy. The mechanism of action of UV radiation in these treatments is not completely clear, however along time some clues have emerged. It is believed that phototherapies have not only a immunosuppressive effect, but also a stimulatory effect on melanocytes<sup>23</sup>.

Although the significant results obtained over the years, there is no consensus on the optimum duration of phototherapy. Also, treatments are far away from achieving a efficacy of 100% in every patient<sup>3</sup>.

### I.1.2.2.1. Photochemotherapies (PUVA and KUVA)

The phototherapy with Psoralens or khellin and ultraviolet A (PUVA or KUVA) combines long wave (320-340 nm) UVA with the photosensitizers Psoralens or khellin<sup>18;23</sup>. Both therapies can be systemic or localized, depending if the photosensitizer is applied orally or in a topical cream. The systemic KUVA therapy has been abandoned because induces liver toxicity<sup>18</sup>.

Along time, several researchers tried to test these treatments and clarify their mechanisms. In 2003, Carlie and co-workers tested the effect of KUVA on melanogenesis and melanocyte proliferation. For this purpose, cultured melanocytes were treated with KUVA. It was verified that khellin induced some extent of proliferation of melanocytes. Then, when the khrellin-treated melanocytes were exposed to UVA, the proliferation effect increased, which evidenced the repigmentation capacity of KUVA treatment<sup>24</sup>.

Later, in 2007, Wu and colleagues studied the effects of PUVA on cultured melanocytes and on Vitiligo patients. The activity of metalloproteinase (MMP)-2, an enzyme which influences cell migration, was measured on PUVA-treated melanocytes. They verified an increase of MMP-2 activity on PUVA-treated melanocytes, when comparing with control (non-treated melanocytes). Also, during this study the melanocyte mitogens/growth factors serum levels of healthy donors, Vitiligo patients, and patients treated with PUVA (with repigmenting Vitiligo) were analyzed. Mitogens are factors that stimulate cell division, while growth factors stimulate cell growth<sup>25</sup>. Only PUVA-treated patients presented high serum levels of melanocyte mitogens/growth factors. Those findings highlighted the capacity of PUVA to slow down the melanocyte destruction<sup>26</sup>.

Several researchers conducted studies to compare both therapies. In 2004, Valkova and colleagues published a research where the effectiveness of local KUVA was tested and compared with systemic PUVA therapy. In patients treated with local KUVA khrelin was applied in water/oil emulsion, on lesional areas. On the other hand, patients treated with systemic PUVA received psoralen orally. Both treatments promoted a comparable degree of repigmentation although the number of patients with repigmentation above 60% was higher in PUVA than in KUVA. However, treatment duration, number of procedures and total UVA dose were higher values in PUVA, what is negative for PUVA-treated patients. No side effects were observed in KUVA-treated patients. However, some patients treated with PUVA presented side effects as erythema, itch, pain and dizziness. Researchers concluded that KUVA treatment is less toxic to patients than PUVA and is able to induce significant repigmentation<sup>27</sup>. Nevertheless, further research must be done to better define the efficacy of topical KUVA in comparison with PUVA.

UVA therapies use long wave radiation, which means that UVA rays penetrate deeply into the tissues. This represents a problem and, for a long time, researchers have mentioned carcinogenesis has a possible long-term side effect on UVA treatments. For instance, in 1996 Buckley and colleagues reported the case of a Vitiligo patient treated with PUVA who presented carcinomas 5 years after treatment<sup>28</sup>.

### **I.1.2.2.2. Narrow Band (NB) - UVB and target phototherapies**

The phototherapy NB-UVB radiation (311nm) is widely used in Vitiligo treatments<sup>18</sup>. Along time, several researchers conducted studies where they compared different Vitiligo treatments, such as NB-UVB and PUVA. In 2015 Xiao and colleagues published a systematic review in which they evaluated the efficacy and safety of NB-UVB. For this purpose, they analyzed seven randomized controlled trials and concluded that the efficacy of NB-UVB is almost equivalent to PUVA, but with fewer side-effects<sup>29</sup>. Besides this, numerous studies obtained better repigmentation values with the NB-UVB treatment. This was the case of a double-blind randomized study published in 2007 by Yones and co-workers, where NB-UVB therapy was compared with local PUVA. 64% of patients treated with NB-UVB presented a repigmentation greater than 50%, while just 36% of patients treated with PUVA presented a repigmentation greater than 50%. Researchers concluded that this therapy can produce the best repigmentation results in Vitiligo patients<sup>30</sup>.

In target phototherapies are used devices as excimer laser or lamp, whose radiation is, as well, in the UVB range<sup>18</sup>. In 2006, Hadi and colleagues analyzed the repigmentation of Vitiligo patients treated with 308-nm xenon chloride excimer laser. They verified that 50,6% of patients presented 75% of repigmentation or more and even 25,5% of patient achieved a repigmentation of 100%. The only side-effect was the appearance of skin burns which was easily solved by changing the dose of radiation. Researchers concluded that this treatment is very effective and safe to the patients<sup>31</sup>.

### **I.1.2.2.3. Oral treatments**

Oral treatments include steroids and immunosuppressants. According to *Guidelines for the management of vitiligo: the European Dermatology Forum consensus*, there is no enough evidences to prove the efficacy of this treatment. Although studies showed that systemic steroids can stop Vitiligo activity, they cannot promote repigmentation and long-term intake of these substances can lead to serious side-effects<sup>18</sup>. As an example, one study conducted by Radakovic-Fijan in 2001 tested the efficacy and safety of a corticosteroid (dexamethasone) oral treatment. 28 vitiligo patients (24 with progressive vitiligo and 4 with stable vitiligo) were subjected to this treatment. Researchers verified an arrest of vitiligo activity in 88% of patients with progressive vitiligo. However, just 6,9% of patients presented repigmentation and 69% presented side effects as insomnia, acne, weight gain, agitation, menstrual disturbance and hypertrichosis<sup>32</sup>.

In fact, the experts that established the guidelines stated that the side-effects do not justify the use of these treatments on patients<sup>18</sup>.

#### **I.1.2.2.4. Surgical treatments**

Surgical treatments consist in autologous transplanting of normally pigmented sites into stable vitiligo regions. There are diverse surgical treatments, such as punch grafting, epidermal blister grafting, ultrathin epidermal sheet grafting and cellular grafts. The first one is not indicated for large lesions. It consists in harvesting a punch graft from the donor site and transplanting it to the local where a similar punch graft was removed (lesion area). Epidermal blister grafting cannot be used, as well, in large lesions and consists in creating an epidermal blister in the depigmented area using liquid nitrogen or PUVA, which is removed after two days and replaced by another epidermal blister previously created in the donor skin. Ultrathin epidermal sheet grafting is a technique applicable for large areas. The unpigmented skin suffers dermabrasion and a thin skin graft from donor is transplanted into the lesion area. Finally, cellular grafting consists in the transplantation of an autologous suspension of melanocytes and keratinocytes<sup>18;33</sup>. Cellular grafting is a topic that will be discussed later.

In fact, not all patients are suitable to these surgical treatments. They are just applied in stable lesions, resistant to other medical treatments mentioned before<sup>33</sup>.

## **I.2. Skin**

### **I.2.1. Anatomy**

The skin is the larger organ of the human body and it acts as a barrier between the organism and the exterior environment. Besides limiting the input and output of water and other important substances, it provides protection against micro-organisms, ultraviolet radiation, mechanical damages and toxic agents<sup>34;35;36</sup>.

The skin is composed by three main layers: epidermis, dermis and hypodermis (or subcutis), and by appendages: hair follicles (HFs), sebaceous glands (SGs) and sweat glands, which are crucial for body protection and regulation of temperature<sup>37</sup> (Figure I-1).

The human body has two kinds of skin, hairless or glabrous skin (for example in the palms and soles) and hairy or hair-bearing skin. The first one is characterized by a thick epidermis and a lack of hair follicles and sebaceous glands. On the other hand, the hairy skin has a thinner epidermis with hair follicles and sebaceous glands<sup>38</sup>. The present master thesis aims to study hairy skin.

#### **I.2.1.1. Epidermis**

The epidermis, the outer layer of the skin, consists of a keratinized stratified squamous epithelium. It has several avascular layers each with a specific substructure (Figure I-1). The deepest layer, named basal layer, contains diverse types of cells: a small portion are melanocytes (producers of melanin) and

Merkel cells (involved in light touch sensation), and the majority are columnar cells with the capacity to divide (dividing keratinocytes). After dividing by mitosis, the daughter cells move to the spinous layer, differentiate, and lose their capacity to divide. These differentiated cells are keratinocytes, the main cells of epidermis, which synthesize specific keratins. The spinous layer is also the main location of the Langerhans cells, whose role is very important in skin immune reactions. The process proceeds to the granular layer, where the cells undergo apoptosis, becoming flatter than the ones in spinous layers, with a granular cytoplasm and a degenerative nucleus. Lastly, the epidermis outer layer, stratum corneum, is composed by layers of dead and flattened keratinocytes. These keratocytes are named corneocytes, and they are filled with keratin protein filaments and the intercellular spaces are filled by lipids. This combination gives rise to a strong physical barrier<sup>35;37</sup>.

All this process, starting in the deepest layer of the epidermis (basal layer), and ending in the outer layer of epidermis (stratum corneum), allows for the continuous renewal of skin cells by shedding off the surface cells and replacing them with new ones coming from the layer immediately below<sup>34</sup>.

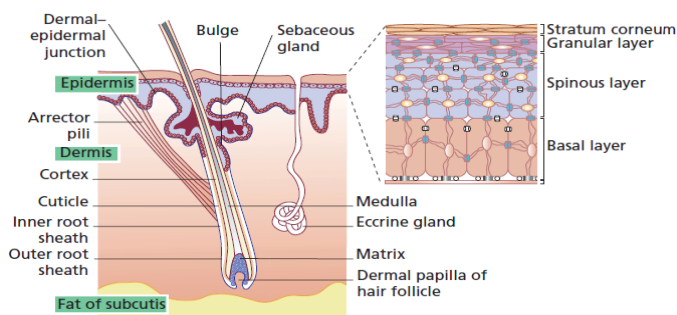


**Figure I-1: Skin layers and appendages<sup>38</sup>.**

### I.2.1.2. Dermis and Hypodermis

The dermis is the connective tissue layer that underlies the epidermis<sup>37</sup>. The dermal-epidermal junction, where the ridges of the epidermis are projected into the dermis, represents a separation between epidermis and dermis and acts as a physical barrier against exchange of cells and large molecules between these layers<sup>38</sup>.

The superficial part of the dermis, papillary layer, is composed by areolar connective tissue with thin collagen fibres, while the deepest layer of the dermis, reticular layer, is composed by irregular connective tissue with thicker bundles of collagen<sup>37</sup>. Unlike epidermis, the dermis has a rich blood supply with origin in the boundary between papillary and reticular layers<sup>35;36</sup>.

Collagen fibres are approximately 70% of the dry weight of the dermis, granting a high tensile strength - mechanical property that represents the maximum stress beyond which the tissue will fail<sup>39</sup>-, and consequently avoiding skin tearing. On the other hand, the dermis also harbours elastic fibres which allow the return of the skin to its original shape<sup>36</sup>.

The hypodermis or subcutis, which lies below the dermis, is the deepest layer of the skin and consists of loose connective tissue and fat<sup>35</sup>.

### I.2.1.3. Skin Appendages: Hair follicles

The hair follicle represents an essential component of mammalian skin that promotes the continuous renewal of the hairs, by undergoing through cycles of rapid grow, regression and resting (hair cycle – section I.2.2). The presence of stem cells (SCs) with high regenerative and proliferative capacities is crucial for the success of hair renewal<sup>40</sup>.

Hair follicles comprise eight epithelial layers: outer root sheath (ORS), the inner root sheath (IRS) composed by four layers (Companion layer, Henle's layer, Huxley's layers and IRS cuticle) and the hair shaft consisting of three layers (Hair cuticle, Cortex and Medulla) (Figure I-2 (B) )<sup>41</sup>. Besides that, it is divided into three segments: the infundibulum, the isthmus and the inferior segment (Figure I-2 (A)). The first one extends from the surface to the opening of the sebaceous gland. The isthmus extends from the infundibulum to the insertion of the arrector pili muscle. Lastly, the inferior segment is composed by the bulb and supra-bulb areas. In the base of this segment is localized the dermal papilla, a vascularized loose connective tissue with inductive properties<sup>42</sup>.

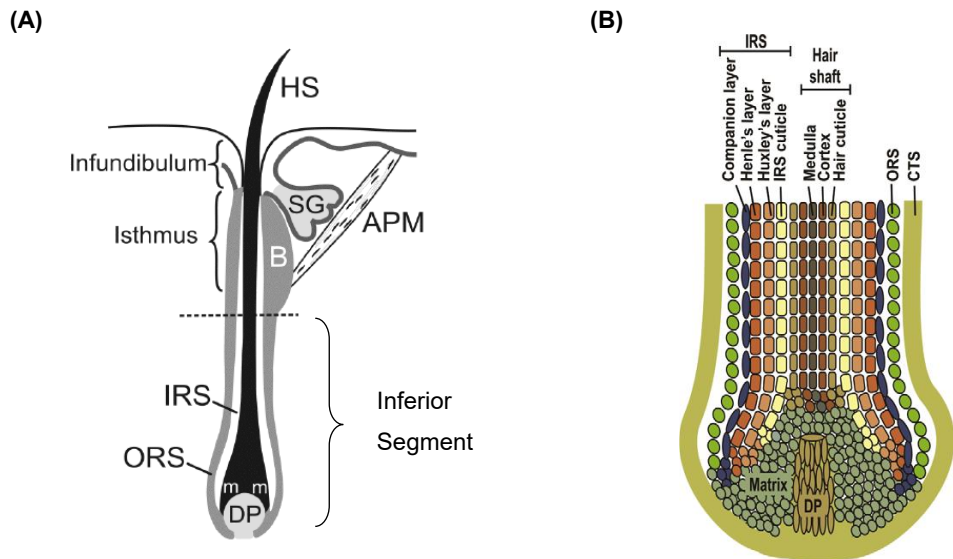


*Figure I-2: (A) Hair follicle structure<sup>43</sup> (B) Hair follicle layers and sub-layers<sup>41</sup>. (APM: arrector pili muscle; CTS: connective tissue sheath; DP: dermal papilla; m: matrix; HS: hair shaft, IRS: inner root sheath; ORS: outer root sheath; SG: sebaceous gland)*

### I.2.2. Hair follicle morphogenesis and cycle

The morphogenesis of the hair follicle occurs through several interactions between the surface epithelium and the underlying dermis (mesenchyme)<sup>44,45</sup>. Firstly, the dermal cue signals promote the

placode formation, a thickening in the embryonic ectoderm. After placode formation, the epithelial cells produce signals that promote the organization of mesenchymal cells into a dermal condensate (DC) which will give rise to the dermal papilla (DP), a permanent part of the hair follicle. Then, dermal signals promote the proliferation and downgrowth of follicular epithelial cells into the dermis. These epithelial cells will form the outer root sheath. Lastly, signals from DP cells will regulate the formation of the inner root sheath and the differentiation of the hair shaft, giving rise to mature hair follicles. The hair follicles are completely mature when the bulb approaches the lower dermis<sup>45,46</sup>.

After hair follicle morphogenesis, the cycling part of the HF undergoes through continuous cycles, to ensure the hair renewal; the permanent part of the HF, ie infundibulum and isthmus, will not change. These cycles comprise three main phases: anagen (growing phase), catagen (regression phase) and telogen (resting phase)<sup>41,47</sup>. Figure I-3 illustrates the process of hair follicle morphogenesis and cycle.

During anagen, the increased metabolic activity of matrix keratinocytes promotes active hair growth, including the production of the inner root sheath and hair shaft. On the other hand, outer root sheath growth does not have origin on matrix cells<sup>40</sup>. According to experiments in mouse models, ORS displays a regional growth, and their progenitors are dispersed in the ORS<sup>48</sup>.

Anagen is divided into six sub-phases, where the set of sub-phases I-V constitute the pro-anagen. Sub-phase Anagen VI ends when the hair follicle stops growing and achieves total differentiation. Then, HF enters in catagen and starts regressing. Herein, begins a process of apoptosis that gives rise to several morphological and molecular changes. This phase is characterized by the end of two important events, namely proliferation of keratinocytes and melanin production by melanocytes. The last phase of the hair cycle is telogen, in which the hair follicle undergoes a rest phase in terms of proliferation and activity<sup>40</sup>.

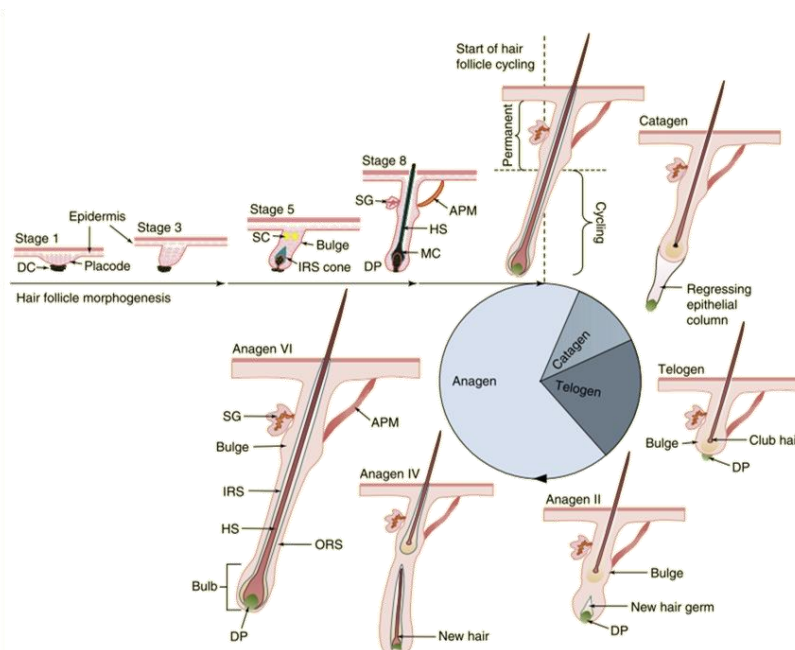


**Figure I-3: Hair follicle morphogenesis and cycle.** APM: arrector pili muscle; DC, dermal condensate; DP: dermal papilla; HS: hair shaft; IRS: inner root sheath; MC: melanocytes; ORS: outer root sheath; SC: sebocytes; SG: sebaceous gland<sup>41</sup>.

### I.2.3. Skin Stem Cells

Stem cells are cells with the capacities of renewing themselves and give rise to differentiated cell types<sup>49</sup>. The skin is one of the human body structures where stem cells have been identified. They consist in adult stem cells that generate progenitor cells, whose function is to ensure the periodic turnover of the tissues. Also, these cells are able to repair or replace injured, destroyed or death cells<sup>50</sup>.

The location of skin stem cells has been studied over time, using several identification methods. One method of identification used is the incorporation of nucleotide analogs such bromodeoxyuridine (BrdUrd) or tritiated [<sup>3</sup>H]thymidine into newly synthesized DNA. Stem cells are characterized by a slow cycling nature, thus by studying the retention of label within these cells allows their identification since only cells that divide rarely will retain the label (Label Retaining Cells – LRCs)<sup>51</sup>. In 1990 Cotsarelis and colleagues published a study where LRCs were identified in mice. For this purpose mice were allowed to incorporate tritiated [<sup>3</sup>H]thymidine, promoting an initial 100% nuclei labeling. One week later, researchers identified labeled cells in a specific area of the hair follicle, the ORS of the midfollicle corresponding to the bulge area<sup>52</sup>.

Another commonly used method consists in studying the proliferative capacity of cells through clonogenic assays. Stem cells are characterized by having a great proliferative capacity. So, through these methods it was possible to identify these cells<sup>51</sup>. In 1994, Rochat and co-workers studied the location of colony-forming cells within the human hair follicle through a clonal analysis. To do so, researchers classified the cloning-forming cells as holoclones and meroclones - derived from stem cells and transit-amplifying (TA) cells respectively<sup>53</sup> -, and verified that most of holoclones derived from an area corresponding to the bulge<sup>54</sup>.

Nowadays several types of skin stem cells are known, as Epidermal Stem Cells and Hair Follicle Stem Cells (HFSCs). HFSCs comprise Melanocytes Stem Cells (MSCs) and Epithelial Stem Cells (eSCs)<sup>55</sup>.

The theme of skin stem cells has been a focus of many studies, however there are still some doubts related to their behavior during the cell cycle and remodeling events<sup>55</sup>.

#### I.2.3.1. Epidermal Stem Cells

As mentioned before, the epidermis undergoes constant renewal during life. Besides that, it is re-epithelialized in case of wound injury. Epidermal Stem Cells have a crucial role during the processes of skin renewal and repair<sup>56</sup>. These stem cells can give rise to a stem cell daughter or a transit-amplifying daughter, that is a cell that is very proliferative but undergoes through a limited number of cell cycles<sup>51;55</sup>. So, this cell will divide typically a few times (two to four times) and then will perform a program of terminal differentiation<sup>51</sup>.

### **I.2.3.2. Epithelial stem cells**

The eSCs are HFSCs that reside in the bulge region and migrate downwards to participate in the HF renewal during each hair cycle<sup>57</sup>. More specifically, it is known that eSCs can give rise to a population of cells which rapidly divide in the matrix, named the transit-amplifying (TA) cells<sup>52</sup>. So, eSCs migrated out of the bulge and colonize the matrix, in the form of TA cells, which proliferate and differentiate, giving rise to hair shaft and inner root sheath<sup>41</sup>.

In addition, further roles of these stem cells in the skin have been studied. Animal studies were performed to assess the need of eSCs in epidermis homeostasis<sup>58</sup>. For instance, some investigators analyzed the response of epidermis to bulge ablation. In 2005 Ito and co-workers analyzed the role of eSCs in epidermal renewal. For this purpose, they performed the ablation of bulge cells, which led to the hair follicles loss but epidermal survival. Subsequently, this suggested that, under homeostasis, HFSCs do not contribute to epidermis renewal. Besides that, this hypothesis was also tested under different conditions, namely in wound healing. Researchers verified that, 8 days after wound excision approximately 26% of the reepithelialized wound cells derived from bulge cells, showing that during wound healing eSCs contribute to epidermis renewal<sup>58,59</sup>.

The role of these stem cells in the renewal of Sebaceous Glands (SGs) was studied as well. Several studies have addressed the response of SGs after hair and eSCs disintegration. Some evidenced the differentiation of SGs only when some hair follicles and respective eSCs were maintained, highlighting the contribution of these stem cells to SG homeostasis. Although intense cross-regulation between eSCs and SG seems to occur further studies need to be performed in order to understand how this process is controlled<sup>60</sup>.

### **I.2.3.3. Melanocyte Stem Cells**

MSCs derive from neural crest cells. First, neural crest cells commit into melanoblasts with the expression of certain genes and proteins as dopachrome tautomerase, tyrosine protein kinase KIT and microphthalmia-associated transcription factor (MITF). Then, the melanoblasts have two possible outcomes namely to continue differentiating into functional and mature melanocytes that produce melanin, or else become MSCs, with renewal capacity. In the case of MSCs, they keep the quiescence state until next hair cycle. When they are activated, loose this quiescence, become transit-amplifying cells and differentiate into melanocytes<sup>61</sup>.

Melanocytes are the pigment producing cells that provide color to the skin and hair. In each hair cycle, there is the proliferation and differentiation of melanocytes. They colonize the hair matrix and produce melanin pigment on melanosomes. Melanosomes are, at that point, transferred into adjacent keratinocytes in order to incorporate the hair shaft and originate pigmented hair<sup>62</sup>.

During catagen phase, melanocytes disappear from the hair matrix, and reappear in the growing phase of the next hair cycle. Actually, there is a clear synchronization between the life cycle of melanocytes (proliferation, differentiation and death) and hair cycle.<sup>62</sup>

The melanocyte stem cell population (also known as amelanotic melanocytes) was firstly reported in 1956 by Montagna and Chase when, after a treatment with ionizing irradiation, a cell population morphologically different from keratinocytes of ORS and without visible melanin pigments was identified. Since then, strong evidence has emerged that confirmed the existence of a population of amelanotic melanocytes in the HFs bulge<sup>62</sup>.

The present master thesis focuses on the hair follicle stem cells (eSCs and MSCs).

## I.3. Useful tools for human hair follicle characterization

The following sections aim to highlight useful tools used for better understand human hair follicle dynamics.

### I.3.1. Markers

As mentioned, methods have been developed to identify specific cell populations such as label-retaining methods and colony forming essays (Section I.2.3). However, these methods did not allow the identification of a wide range of cell populations, so several markers for specific HF regions and HF cell populations have also been utilized. In addition, these markers are nowadays widely used in the isolation of those cells<sup>50</sup>.

#### I.3.1.1. Cytokeratins

Cytokeratins are considered structural proteins<sup>42</sup>. In 1994, CK-19 was studied by Narisawa and colleagues. They tested the reactivity of the monoclonal antibody Ks19.1 against CK-19 in human HFs and observed that this antibody stained not only bulge cells but also cells of infundibulum region<sup>63</sup>.

In 1998 Lyle and colleagues studied the location of human HFSCs. For this purpose, they transplanted human skin into mice (a technique named xenotransplantation, discussed later in section I.3.2.4). Firstly, they performed immunohistochemistry using the monoclonal antibody C8/144B, which predominantly identified bulge cells. Then, they characterized the C8/144B antibody as specific for CK-15 of keratinocytes. Finally, they identified the presence of typical stem cell features on cells labeled with CK-15, as slowly cycling and proliferative behavior at the beginning of anagen. Those findings highlighted that CK-15 may be used as a marker of HFSCs<sup>64</sup>.

### I.3.1.2. CD-Markers

Cell surface markers with significant specificity have also been identified. In 2006, Ohyama and colleagues identified surface proteins which are candidates to be stem cells markers. More specifically, they performed a microarray analysis to obtain the gene expression profiles of bulge ORS cells. Then, these profiles were compared with those of other defined ORS cell populations, in order to find genes with specificity to bulge area. They identified CD200 as a surface marker with high specificity to bulge area, although the antibody anti-CD200 also stained the companion layer. In addition, other surface markers were identified as surface proteins that are overrepresented in certain ORS areas namely CD24 in the inner bulge, CD34 in suprabulbar region and CD71 in both sub-bulge and suprabulbar regions. The regions established by researchers are represented in Figure I-4<sup>65</sup>.

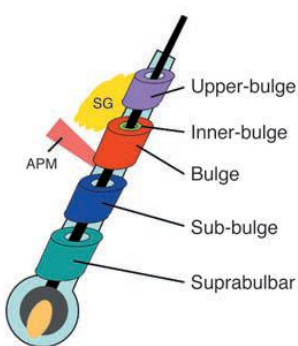


**Figure I-4: Regions of hair follicle ORS established by Ohyama and colleagues to characterize surface markers expression<sup>65</sup>.**

### I.3.1.3. Other markers

Other useful markers for hair follicle characterization have been identified.

As mentioned before, transit amplifying (TA) cells are relatively undifferentiated cells which have high proliferative capacity but go through limited number of cell cycles<sup>55</sup>. In 2003, Xu and colleagues analyzed the biological differences between TA cells and HFSCs in their respective compartments (bulb and bulge respectively). It is known that bulge stem cells maintain their quiescence for long periods of time, and only proliferate slightly in the beginning of the anagen phase. On the other hand, TA cells present in bulb matrix have a high proliferative rate. Researchers studied the expression of several genes, and verified that Cyclin D1 was highly expressed in bulge when compared to the bulb. Furthermore, they observed the presence of cyclin D1 in telogen bulge, but not in anagen bulb. This evidence strongly suggested that cyclin D1 may play an important role in the process of conversion of stem cells into TA cells, despite not contributing to hair follicle proliferation during anagen. Consequently, cyclin D1 can be used as a marker of HFSCs within the context of the HF.<sup>66</sup>.

Ki-67 is a proliferation marker useful to characterize hair follicles and their cells. As an example, in the study mentioned in I.3.1.1 conducted by Lyle and colleagues in 1998, researchers analyzed, as well,

the expression of ki-67 antigen in C8/144B positive cells (that is, HFSCs) during the hair cycle. It was shown that C8/144B positive cells were also ki-67 positives in early anagen. During mid-anagen, catagen or telogen C8/144B positive cells were ki-67 negative. It was concluded that these stem cells were highly proliferative only during early anagen, maintaining their quiescence in the remaining phases of hair cycle<sup>64</sup>.

### I.3.2. Cell cycle Dynamics

The cell cycle is an essential phenomenon for hair follicle growth during Anagen phase, which means that any cycle disturbance can bring serious consequences to hair follicle dynamics. Studying cell cycle regulation can expose details extremely important in, for example, hair follicle culture<sup>67</sup>. For instance, details like the number of cycling cells and their rate of progression can give relevant clues about cell growth rates and tumorigenicity<sup>68</sup>. In addition, in the case of a disease as Vitiligo, where aggressive approaches are used as treatment (section I.1.2), it is very important to study the cell cycle dynamics in order to better understand and deal with reactions after treatments<sup>67</sup>.

#### I.3.2.1. Cell cycle - background

Cell cycle is the set of events that happen between two mitoses. Proliferating cells are in cycle and pass through several cell cycle phases: the growth phase after mitosis or interphase (G1-phase), DNA synthesis (S-phase), resting or pre-mitotic growth phase (G2-phase) and mitosis. When cells are in G1, instead of entering in S-phase, they can enter in quiescence, named G0-phase, or can differentiate (Figure I-5). When cells are in G0, they can enter, once again, in cycle after stimuli<sup>38</sup>.

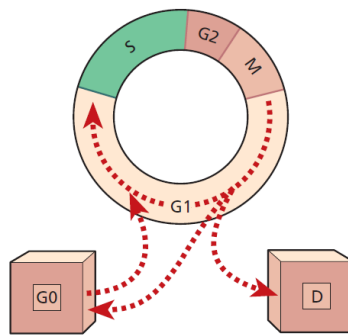


**Figure I-5: Cell cycle of proliferating cells.** (M: mitosis; G1: interphase or post-mitotic growth phase; S: DNA synthesis; G2: resting or pre-mitotic phase; G0: stem cells not proliferating (quiescence); D: cells differentiating)<sup>38</sup>.

### I.3.2.2. Cell cycle quantification

Cell cycle quantification relies on labeling cells with DNA stains and/or specific stains, as nucleosides analogues that label cells in specific cell cycle phases such as S-phase<sup>69</sup>.

Measurement of DNA content allows understanding the frequency of cells present in each cell cycle phase, since DNA content of G1 and G2 cells is respectively 2n and 4n (Figure I-6) <sup>69;70</sup>.

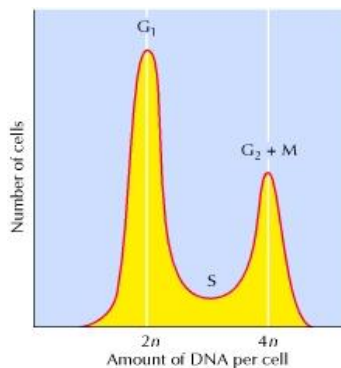


**Figure I-6: Cell cycle curve, presenting G1 and G2 populations (G1 and G2 peaks, respectively)** <sup>69</sup>.

[<sup>3</sup>H]thymidine and BrdU have been widely used in cell cycle studies to stain cells in S-phase. In the case of [<sup>3</sup>H]thymidine, the signal is detected through autoradiography, a technique in which the signal is acquired extremely slowly and is not simple to perform. Besides the low resolution of the obtained images, other disadvantages of the technique are the induction of DNA damage, with resulting interference with cell cycle progression through formation of DNA double-strand breaks<sup>71;72</sup>.

The detection of BrdU is much faster since anti-BrdU antibodies are used to accomplish immunologically the detection of the signal. Another advantage of BrdU over [<sup>3</sup>H]thymidine, is the higher resolution of the images<sup>71</sup>. However, investigators have shown that BrdU can promote cytostatic effects and, when exposed to UV light, BrdU-labeled DNA can, as well present, double-strand DNA breaks and suffer damage<sup>72</sup>. In a study published in 2003 by Diermeier and colleagues, the effect of BrdU in four cell lines was tested and compared with cells already described as BrdU sensitive. They observed that, although this treatment did not affect cell viability, cell cycle progression was affected in three cell lines, since proliferative activity was reduced in certain cell phases<sup>73</sup>. Another disadvantage is the need of DNA denaturation to allow anti-BrdU antibodies to reach BrdU epitopes. The desnaturation process is extremely harsh to DNA and can promote structure degradation.<sup>71</sup>

5-Ethynyl-2'-deoxyuridine (EdU) is an analogue of thymidine used as an alternative to [<sup>3</sup>H]thymidine and BrdU. EdU has the huge advantage of no need DNA denaturation (reaction details in section III.1), which makes it easier to use.

### **I.3.2.3. Quantification of cell cycle using Flow Cytometry vs Microscopy**

Flow cytometry is the gold standard technology used for cell cycle quantification, since it provides a fast and truthful cell cycle analysis<sup>68;70</sup>. Although many studies have been shown the feasibility and reproducibility of this method, some researchers have been struggling with the requirement of specific instrumentations, and knowledge and experience with this technology<sup>68</sup>. In order to overcome this issue, in the past years some investigators have tried to find an alternative to this technique. Quantification of cell cycle using Fluorescence Microscopy has been studied and seems to be an accurate alternative to flow cytometer<sup>68;74</sup>. One advantage of microscopy in the case of tissues is the possibility of maintain spatial context, that is, the natural architecture of samples in contrast to flow cytometry<sup>74</sup>. In one study published in 2015 by Roukos and co-works, these researchers developed a protocol for determining cell cycle staging through measuring DNA content, using two different fluorescence microscopies: High-throughput confocal microscopy and Widefield microscopy. They also describe a method for analyzing the images in order to obtain canonical “cell cycle curves” similar to those obtained by flow cytometry. In the end, the cell cycle profiles obtained with both microscopies were similar, evidencing the possibility of using either type of microscopy (high-throughput and widefield) for this analysis. In this study they applied the protocol to measure DNA content using DAPI but researchers highlighted the possibility of using this protocol with other stains<sup>68</sup>. In 2017, Ferro and colleagues also reported the use of microscopy to acquire DNA content but using a different method for image analysis. Since they used a different cell line, the values obtained cannot be compared, however this study is a evidence that cell cycle quantification using microscopy has been a focus of studies of numerous investigators in the past few years<sup>74</sup>. In the present master thesis, the protocol of Roukos published in 2015 was adapted for cell cycle quantification.

#### **I.3.2.3.1. Widefield Fluorescent Microscopy, Point Scanning Confocal Microscopy and Spinning Disk Confocal Microscopy**

This section contains a sum-up about microscopies used in the present master thesis: Widefield Fluorescent Microscopy, Point Scanning Confocal Microscopy and Spinning Disk (SD) Confocal Microscopy.

These microscopies are based in the phenomena of fluorescence that is when a molecule absorbs a photon with certain wavelength this promotes the excitation of an electron to a higher energy level. Then, the electron returns to the lowest energy level and emits a longer wavelength photon. The emitted photon has a longer wavelength due to the loss of energy when returns to the ground state. The spectrum of absorption and emission will have their peaks in different wavelengths and the difference between them is named the Stokes' shift<sup>75;76</sup>.

Not all specimens exhibit auto-fluorescence, so fluorochromes are used to stain specific tissue components. These fluorochromes are excited by radiation in a specific range of wavelengths<sup>75</sup>.

The microscope used in this thesis are different. The standard widefield microscopy is composed by the filter cube, which comprises an exciter filter, a beamsplitter and an emission or barrier filter (Figure I-7 (A)). The excitation light is emitted by the source and passes through the excitation filter which selects the wavelengths of interest to excite the specimen. After, the beamsplitter (dichroic mirror) reflects the excitation wavelengths in order to direct them to reach the specimen. Then, emitted light by the specimen passes again through the beamsplitter and reaches the emission filter, which selects the range of wavelengths that will pass towards the detector<sup>77</sup>. Widefield Microscopy is a type of fluorescent microscopy where a large volume of the specimen is illuminated by a wide cone<sup>78</sup>.

In confocal microscopy the excitation light source is a laser. The laser line reaches the dichroic mirror, which will reflect the light with wavelengths of interest (excitation wavelength). After, the laser passes through the objective, scans the specimen and emits light that passes back to the objective and the dichroic mirror. A pinhole (physical barrier) placed before the detector eliminates out-of-focus light. Just the light in the focal plane is detected, originating as image with higher resolution than standard fluorescent microscopy (Figure I-7 B))<sup>76;79</sup>.

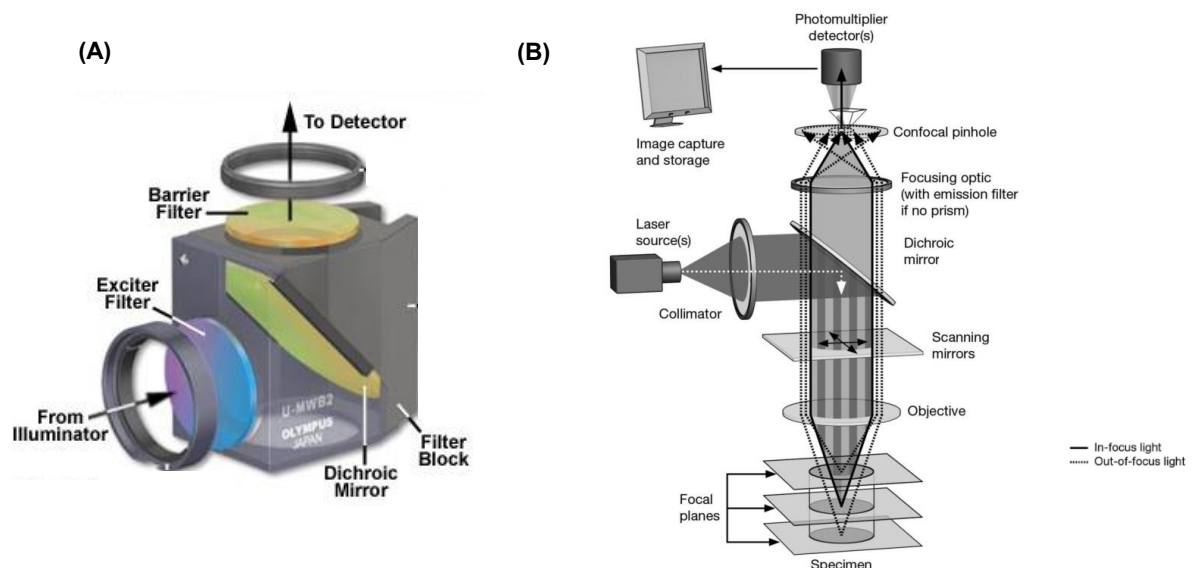


**Figure I-7: Light paths of (A) standard widefield fluorescent microscopy<sup>77</sup> and (B) point scanning confocal microscopy<sup>79</sup>.**

In the case of Point-Scanning microscopy, there is a single pinhole and focused spots are scanned one at a time. However in spinning disk microscopies has a different configuration, where the pinhole is replaced by the pinhole disk, which allow the simultaneous detection of multi points<sup>78</sup>. The second confocal microscopy performs a faster scan of the specimen, however has the disadvantage of presenting lower resolution, since some emitted light out of focus can still reach the detector, what creates artefacts and consequently reduces the resolution<sup>80</sup>.

#### I.3.2.4. Cell cycle dynamics of hair follicle cells

Besides using nucleosides analogues to study the cell cycle of specific isolated cells, as previously described, researchers have used these labels for characterizing proliferation patterns in biological tissues such as the HF.

In 1980, Weinstein and colleagues studied the cell proliferation kinetics of human matrix cells. For this purpose, the scalp of seven volunteers was injected with [<sup>3</sup>H]thymidine, and scalp biopsies were taken after specific time intervals. Autoradiography was used to acquire the signal and, subsequently, researchers determined the labeling index, that is, the percentage of cells labeled with [<sup>3</sup>H]thymidine. They performed this quantification just below the critical Auber's Line (AL), which is the line that crosses the widest part of dermal papilla. The mean value of labeling index 1 hour after injections was approximately 29%<sup>81</sup>.

More recently, in 2009, Klopper and colleagues developed a classification system for distinguish human HFs in anagen IV from early catagen. Subsequently, qualitative and quantitative criteria were established. These criteria consider the use of some markers such as DAPI (DNA stain), Ki-67 (to identify cycling cells) and TUNEL (which identifies apoptotic cells), to perform immunohistochemistry on anagen IV and catagen HF sections. Some of the criteria follow: higher value of DAPI positive cells below AL in anagen IV, than in catagen; higher percentage of Ki-67 positive cells below AL in anagen IV, than in catagen, higher percentage of cells TUNEL positive inside dermal papilla in catagen, than in anagen IV, and higher percentage of cells TUNEL positive below AL in catagen, than in anagen IV. This type of discrimination is extremely important in HF studies since the dynamics of anagen IV and catagen are completely different<sup>82</sup>.

In 2016, Purba and colleagues developed a primer for studying cell cycle dynamics in human HF and mentioned EdU as a useful S-phase marker. They used sections of human HFs, previously incorporated with EdU, to performed immunofluorescence experiments. They evidenced the potential of EdU alone or in a double stain with Ki-67 or phosphor-histone H3 (H3), which is present during mitoses. In figure I-8 (a), (b) and (bii) are represented the proliferative regions of (a) HF matrix and (b) (bii) ORS after EdU incorporation. Additional images on figure I-8 represent double staining with (c) EdU and pH3 or (d) (dii) EdU and Ki-67, which allow the simultaneous analysis of cell cycle phases. In figure I-6 (c) EdU-positive cells are in S-phase and pH3 positive cells are in M-phase. In figures I-8 (d) and (dii), since Ki-67 marks at all cell cycle phases, it is possible to distinguish EdU-positive cells from remaining populations, that is to distinguish cells in S-phase from cells in G1, G2 and Mitosis<sup>67</sup>.

Ki-67 seems to be very useful in the previous contexts, however the analysis of this marker alone is not enough to characterize cell cycle dynamics because Ki-67 protein is present in all active phases of cell cycle (G1, S, G2, M). This means that the signal of the antibody anti-ki-67 do not allow to distinguish cell cycle phases, allowing just the distinction between non-cycling/quiescent (G0; Ki-67 negative) and cycling cells<sup>67</sup>.

Therefore, the aforementioned information allows a better understanding of the reactivity of markers in specific HF regions. In addition, they are useful to compare HFs in different hair cycle stages and, and compare HFs of healthy people and patients with specific disease such as Vitiligo<sup>67</sup>.

EdU is the nucleotide analogue used in the present master thesis, either for cell cycle quantification and HF characterization.

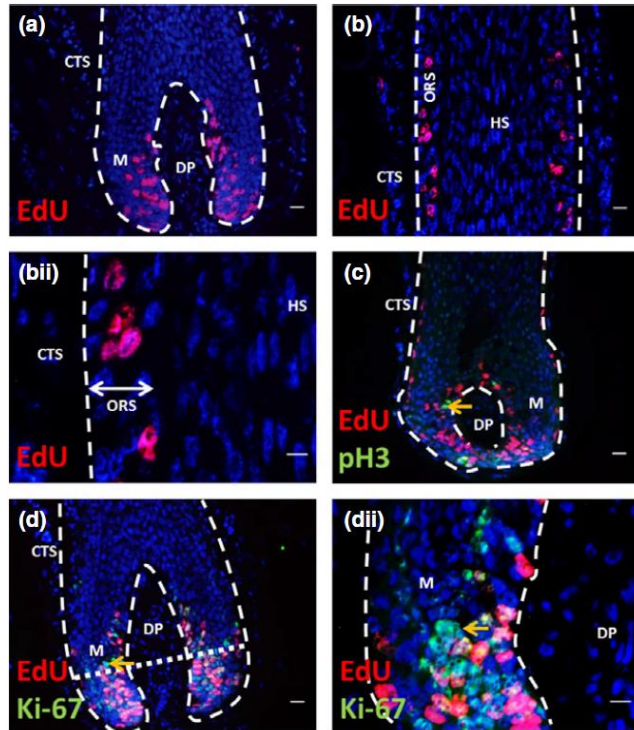


**Figure I-8: EdU incorporation (a) (b) (bii) alone and (c) double stain with pH3 or (d) (dii) Ki-67** <sup>67</sup>.

In the studies mentioned until now HF dynamics has been addressed utilizing microdissected human HFs. In these studies, the signaling between hair follicle and surrounding tissues is lost, what may interfere in cell cycle behavior since the microenvironment has been altered<sup>67</sup>. Numerous studies have used animal models, and although murine and human hair follicles have similar anatomy and cell populations, murine hair follicle dynamics cannot be directly translated to human hair follicle<sup>83</sup>. Xenotransplantation is a method that emerged in order to overcome this issue. It has been used to study human hair follicle cycle, and consists in transplanting human skin into a mice<sup>84</sup>. The xenograft model was introduced by Reed and colleagues in 1973, where they transplanted human skin into an athymic mice<sup>85</sup>. This model has since then been widely used. In 2016, Oh and co-workers developed an extensive guide for studying human hair follicle cycling based on human anagen HFs transplanted into immunocompromised mice. Besides this, the method has the disadvantage of being associated with events not present in normal hair cycle, as the process of surgery and healing. Therefore, there is not a complete understanding about which events observed in the xenograft model represent the normal hair cycle *in vivo*<sup>83</sup>.

## I.4. Isolation of Hair Follicle Stem Cells and their application on Vitiligo therapy

In 1991 Cui and co-workers proved the role of HFSCs, more specifically, Melanocyte stem cells on Vitiligo repigmentation. They observed the changes of melanocytes on skin from healthy donors and from patients with Vitiligo through dihidroxifenilalanina (DOPA) stain. Previously, the MSCs (or amelanotic melanocyte population) present on bulge region were described as DOPA negative. These inactive melanocytes just produce melanin when there is a stimulus, becoming active melanocytes. Researchers observed that DOPA-positive melanocytes were absent on Vitiligo patients, however the inactive melanocytes of bulge (DOPA-negative) were undamaged. This evidence suggested that DOPA-negative melanocytes, that is, MSCs, are the cells that potentiate repigmentation of Vitiligo lesions<sup>50;86</sup>. Consequently, due to the huge potential of HFSCs, their isolation has been investigated in order to develop clinical treatments based on regenerative medicine.

As mentioned before, specific markers have been widely used for this purpose. Namely, CD-markers, as CD200 which is highly expressed on bulge cells<sup>50</sup>. In addition, different culture media have been tested.

In 2006, Ohyama and colleagues used microarray analysis to identify CD-markers for human hair follicle cells, as mentioned before on section I.3.1.2. Besides that, they also isolate human HFSCs by combining positive and negative markers of bulge cells. So, for this purpose, they extracted the cells from human scalp biopsies through a series of incubation steps with solutions that promote connective tissue elimination and the disruption of epithelial cells from HFs. After filtration with a mesh filter, HFSCs were isolated using magnetic beads. First, they performed a negative selection, using negative markers of bulge cells and lastly, they positively selected cells CD200. For further assays, they cultured isolated cells in a mixture of DMEM and Ham's F12 Medium<sup>65</sup>.

More recently, Hilmi and colleagues developed a culture method for epithelial stem cells derived from human hair follicles (2013). Their protocol for obtaining cell suspension was very similar to the one performed in 2006 by Ohyama, comprising the series of incubations and the final filtration. However, they used a different culture media, the CnT07 which is a fully defined media developed by CellnTec for human keratinocyte culture<sup>87</sup>. In order to analyze HFSCs viability, they cultured cells in CnT07 without coating matrix and in KSFM media with coating matrix and verified, along days of culture, the presence of a larger number of cells on CnT07 cultures<sup>88</sup>. This paper highlighted the potential of CnT07 culture media, and actually we are using it in our protocol.

Creating a simple and effective method of HFSCs isolation and culture can bring significant progress on Vitiligo treatments. HFSCs culture can potentiate research progress. In addiction, there is a novel technique of cellular grafting for stable Vitiligo treatment, which uses cultured and non-cultured HF cell suspensions<sup>89</sup>. In 2011 Mohanty and colleagues tested the efficacy of this novel surgical technique, on 14 patients with stable Vitiligo. For this purpose, they applied the cell suspension on dermabraded recipient areas. They verified that 9 of 14 patients presented repigmentation above 75%. The mean

repigmentation was approximately 65.7%<sup>90</sup>. In 2017, a study conducted by El-Zawahry and colleagues, aimed to compare this technique with another which uses non-cultured epidermal cells instead of non-cultured HF cells. The cells number obtained from epidermis was significantly lower, although the repigmentation was similar. These results suggested that using HF cell suspensions is a more effective method<sup>91</sup>.

Cellular grafting seems not causing harmful effects on patients so far, what is an advantage over other treatments mentioned before as phototherapies or topic treatments<sup>92</sup>. However, the repigmentation rates are still not ideal. The improvement of this method can really make the difference on this issue.



## II. Aims of the study and Motivation

The prevalence of Vitiligo in most of the world's population is around 0.5 and 1%<sup>2</sup>. However, there are countries that have higher values such as India (8.8%) and Romania (2.3%) <sup>3;93</sup> This highlights the need for developing an effective treatment for this disease. Ideally, Vitiligo treatment should achieve two main goals: arresting of depigmentation and induction of repigmentation of affected skin. However main usual and novel treatments do not take into account these two aspects<sup>94</sup>. This project was developed in the context of a broader strategy aimed at implementing a cell therapy for Vitiligo using HF stem cells. Most studies on hair follicles have been performed in animal models. Since human HF do not show the same dynamics, the results of such studies cannot be directly translated to human HFs<sup>83</sup>. Given that stem cell populations of HFs comprise melanocyte precursors<sup>50</sup>, HF stem cells seem appropriate for amplification and subsequent manipulation in order to provide a rational treatment of Vitiligo.

The need for a novel therapy for Vitiligo combined with the obvious potential of HFSCs has motivated this research. This master thesis intents to contribute to fill-in this gap. For this purpose, the aims of the study are:

- 1) Developing a relatively fast and user-friendly tool for cell cycle quantification using microscopy, which can be applied to sectioned human HFs;
- 2) Development of a quantitative method for analyzing human HF dynamics in vitro, which can be applied to disease models such as Vitiligo and/or adapted to other labels to easily study other features besides proliferation;
- 3) Initiating the work leading to HFSCs isolation.

This master thesis was conducted at Instituto de Medicina Molecular/IMM-João Lobo Antunes, Lisbon, in collaboration with the Stem Cell Bioengineering and Regenerative Medicine Laboratory located at Instituto Superior Técnico/IST Tagus Park campus, Serviço de Dermatologia, Hospital de Santa Maria (Lisbon), and Serviço de Dermatologia, Hospital CUF Descobertas (Lisbon).



## III. Materials and Methods

### III.1. Cell cycle quantification using 5-Ethynyl-2'-deoxyuridine (EdU)

Human colorectal carcinoma HCT-116 cells were extensively used herein to develop a tool for cell cycle quantification by microscopy. For this purpose, these cells were exposed to 5-Ethynyl-2'-deoxyuridine (EdU), a thymidine analog that incorporates into cellular DNA during S-phase of cell cycle<sup>71</sup>. The EdU-coupled signal was measured after capture by fluorescence microscopy and analyzed to quantify cell cycle phases.

EdU has an alkyne group at the 5 position of the pyridine ring in contrast with thymidine which at the same position has a methyl group. This analog can be detected after its specific binding to a fluorochrome-conjugated azide through covalent bonding (Figure III-1)<sup>71</sup>.

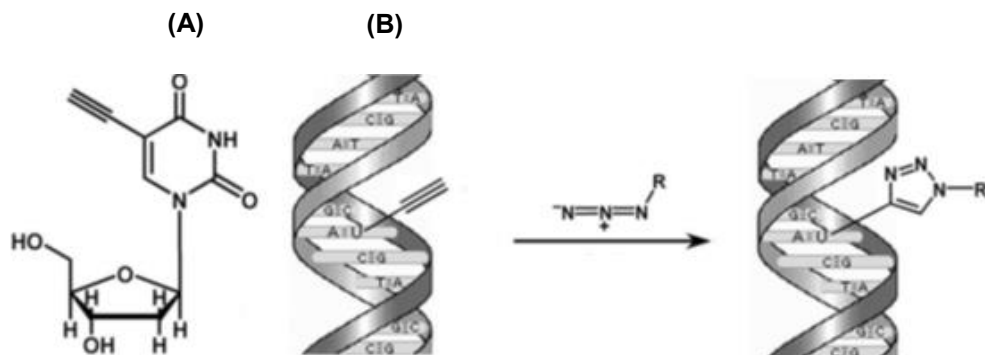


Figure III-1: (A) Structure of 5-Ethynyl-2'-deoxyuridine (EdU); (B) Reaction between alkyne group of EdU and the fluorochrome-conjugated azide<sup>71</sup>

For this set of experiments we have extensively used the Click-iT® EdU Alexa Fluor® 488 Imaging kit (Invitrogen), which contains not only the EdU but also all the needed components in the reaction including the azide-coupled fluorophore (Alexa Fluor 488).

#### III.1.1. Cell culture

Human colorectal carcinoma HCT-116 cells were cultured in RPMI 1640 (31870025; Gibco®) medium, supplemented with 10% foetal bovine serum (FBS), 2mM L-glutamine, 10 mM MEM non-essential amino acids and 100U/ml penicillin/streptomycin (all from Gibco®), and maintained at 37°C in a humidified incubator at 5%CO<sub>2</sub>. The medium was changed every 2-3 days, and cells were passaged

when sub-confluent to petri dishes containing glass coverslips. When cells growing onto coverslips reached a confluence of approximately 60-70% they were transferred to 30cm<sup>2</sup> petri before exposure to EdU.

### III.1.2. EdU incorporation

EdU was added to parallel cultures to a final concentration of 10µM, from a stock of 10mM in DMSO, for incremental periods of time (1h increments). In this way, the cell culture firstly pulsed with EdU presents the biggest incorporation time (8h or 10h). Figure III-2 corresponds to a schematic of the EdU incorporation procedure in the case of experiments with 8 time-points. Cells not exposed to EdU were used as controls (T0Ah and T0h). In this case, cells were exposed to fresh medium not containing EdU. Then, cells were fixed, for 16-72 hours with 4% formaldehyde (FA) in PBS, freshly prepared from a 37% formaldehyde stock (Sigma®).

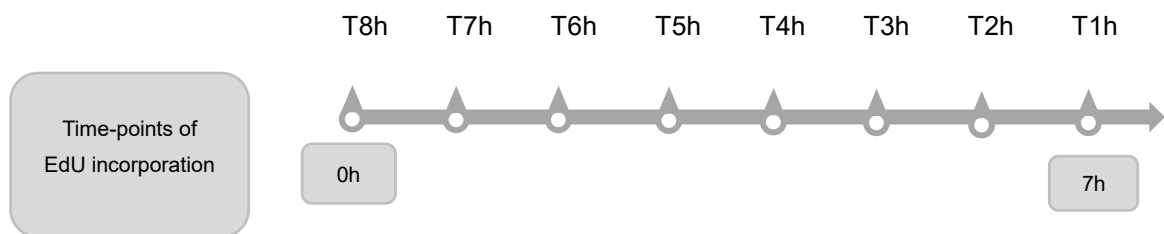


**Figure III-2: EdU incorporation procedure in experiments with 8 time-points. Cells incorporated EdU for incremental periods of time, from 0h to 8h/10h. In this case, cells corresponding to time-point T8h were pulsed on 0h and incorporated EdU continuously for 8h. In contrast, T1h cells were just pulsed on 7h, incorporating EdU for 1h.**

### III.1.3. EdU staining (EdU detection system)

Firstly, the cells were washed three times with Elix® water, and incubated 5 minutes with 70% Ethanol (EtOH) (Merck) at room temperature. Next, the cells were washed again three times with Elix® water and then incubated with PBS containing 1%SDS (sodium-dodecyl-sulphate) for 10 minutes at room temperature. After increasing the permeability of cells with ethanol followed by SDS, cells were washed three times with PBS plus 0.05%Triton X-100 (Sigma®) and incubated for 20 minutes with the reaction cocktail prepared from the Click-iT® EdU Alexa Fluor® 488 Imaging kit. Table III-1 shows the components used to prepare the reaction cocktail for a total volume of 500µL (added in the order listed in the table). One of the controls was incubated with the EdU detection system (T0h), unlike T0Ah which was not.

**Table III-1: Components to prepare the reaction cocktail, to a final volume of 500 µL.**

Reaction Components	Volume
1x Click-iT® EdU reaction buffer	430 µL
CuSO <sub>4</sub>	40 µL
Alexa Fluor® Azide	1.2 µL
1x Click.iT® EdU buffer additive	50 µL
TOTAL	500 µL

### III.1.4. Whole DNA staining

For staining of whole DNA, cells were washed three times with PBS/ 0.05% Triton X-100 and subsequently incubated with the DNA stain for approximately 4 hours in the dark in the case of 4',6-Diamidino-2-Phenylindole (DAPI, D9542, Sigma®), or Hoechst 33342 (Click-iT® EdU Alexa Fluor® 488 Imaging kit – Invitrogen) at room temperature, or in the case of Propidium Iodide (PI, P4170 ,Sigma®) overnight at 4°C. Table III-2 depicts the concentrations in PBS for each DNA stain.

**Table III-2: Concentration of DNA stains.**

DNA stains	Concentration
DAPI	1µg/mL
Hoechst 33342	1µg/mL
PI	10 µg/mL

Cells were then washed again three times with PBS/ 0.05% Triton X-100. Lastly, microscope slides were mounted in VECTASHIELD® medium (Vector Laboratories) and stored at -20°C until used.

#### III.1.4.1. Propidium Iodine

PI is not specific for DNA, it binds also to RNA<sup>95</sup>. In experiments where PI was used to stain exclusively DNA a step to remove RNA using RNase A (Sigma®) was also performed. To do so, after the steps for cellular permeabilization cells were washed three times with PBS/ 0.05% Triton X-100 and incubated with a solution of 500µg/mL RNase A in Tris 0.1M and 10mM MgCl<sub>2</sub> for 45min at 37°C. After washes with PBS/ 0.05% Triton X-100, 1%FA was added for 5 minutes to inactivate RNase A. We then proceeded for EdU detection and whole DNA staining (PI) as mentioned before.

### III.1.5. Image acquisition using Widefield Fluorescence Microscopy

Images of the cells were acquired using a Widefield fluorescence microscope *Zeiss Axio Observer*. Depending on the specific experience, either a single channel (Alexa 488) or a multi- channel (Alexa 488 and DAPI or Alexa 488 and Hoechst or Alexa 488 and PI) acquisition was utilized. The *ZEN 2* (blue edition) software was used to establish the appropriate settings for image acquisition, namely filters, light source intensities and exposure times. Those settings were established at the beginning of each acquisition with a microscope slide that featured the maximum intensity possible of EdU-coupled fluorescence, typically the time point T8h of EdU incorporation. During configuration of the settings, to avoid overexposure of the samples, the checkbox *range indicator* was activated, which displays a monochrome image with saturated pixels in red and pixels with zero value in blue. As mentioned before, widefield fluorescence microscope is composed by a filter cube, which comprises excitation and emission filters. These filters dictate the range of wavelengths that is excited and emitted. So, the filter cube choice was made using the ThermoFisher Scientific online tool: *Fluorescence Spectra Viewer*<sup>96</sup>, by analyzing not only the spectra of excitation and emission of the fluorophores, but also the wavelength ranges of excitation and emission of the available filtersets (or filter cube) of the microscope (Table III-3). This allowed to make sure that the excitation and emission spectra of the different fluorophores were correctly individualized, minimizing overlapping between Alexa 488 and whole DNA stains spectra. After this analysis, the spectra of excitation (dashed line) and emission (continuous line) of DAPI (blue), Hoechst (blue), Alexa Fluor 488 (green) and PI (orange) were obtained (Figure III-3, III-4 and III-5). The filters wavelengths are also represented in the figures with colored columns (numbers 1-3, EX: excitation and EM: emission).

After establishing image capture settings, 12 images per time-point were acquired with a magnification lens of 20x, resolution of 2252 × 2208 pixels (624,7 × 501,22 µm) and pixel size of 0,227µm.

**Table III-3: Wavelength ranges of excitation and emissions of filtersets on Zeiss Axio Observer**<sup>97</sup>.

Number	Filterset	Excitation (EX)	Emission (EM)
1	DAPI	335-383nm	420-470nm
2	HE GFP	450-490nm	500-550nm
3	HE DsRed	538-562nm	570-640nm

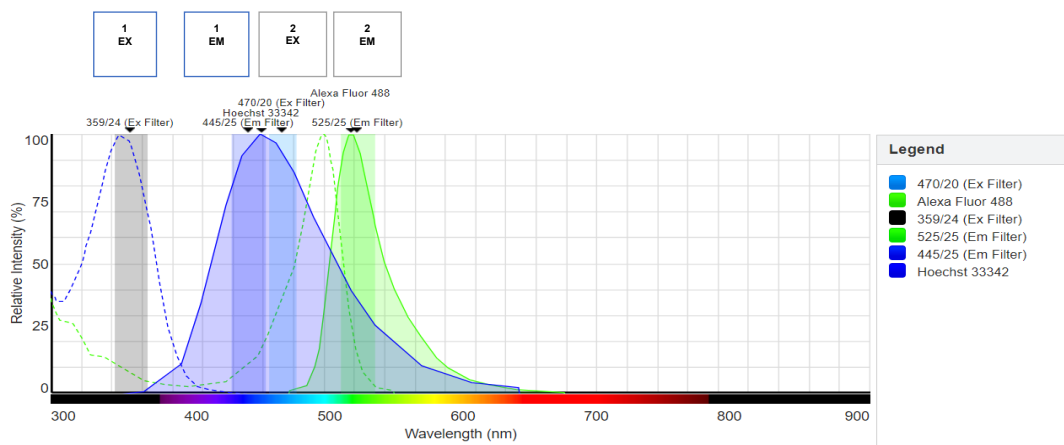


**Figure III-3: Excitation and emission spectra of Alexa Fluor 488, Hoechst 33342, and filtersets DAPI and HE GFP<sup>96</sup>.**

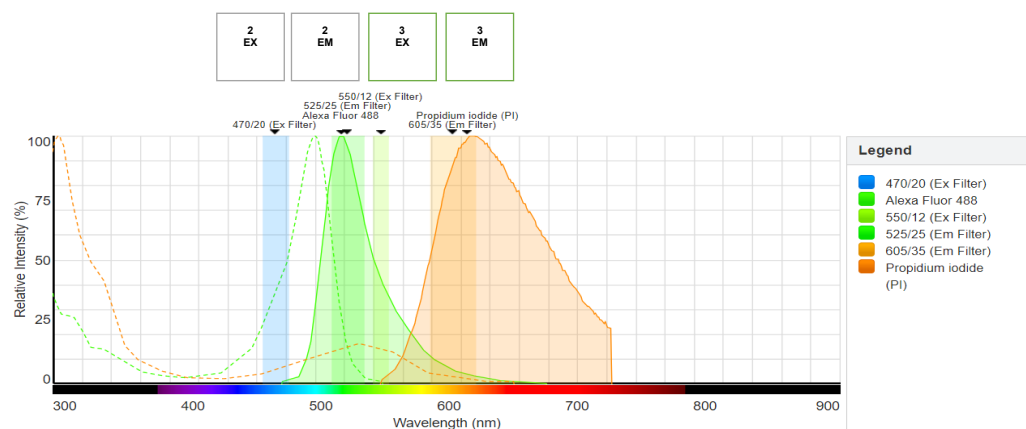


**Figure III-4: Excitation and emission spectra of Alexa Fluor 488, PI, and filtersets HE GFP and DsRed<sup>96</sup>.**

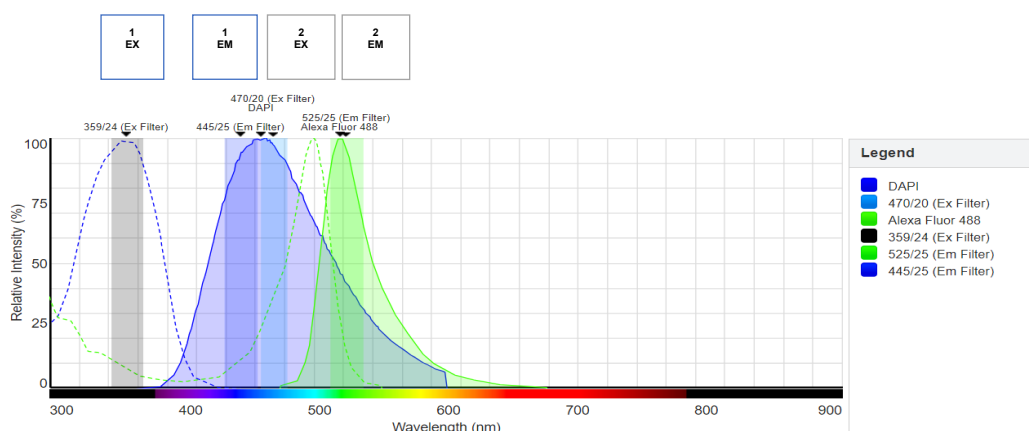


**Figure III-5: Excitation and emission spectra of Alexa Fluor 488, DAPI, and filtersets DAPI and HE GFP<sup>96</sup>.**

### **III.1.6. Image acquisition using SD confocal microscopy**

The SD Confocal Microscope 3i *Mariana SDC* was used to perform a single channel acquisition of Alexa 488. This type of microscopy was used for generating data to be compared with those obtained by widefield microscopy. For this purpose, all the settings regarding laser unit, laser intensity, exposition time and z stack were carefully established in the *SlideBook 6.0.4.* for a time point expected to feature maximum staining intensity for EdU (T8h), corresponding to the longest duration of EdU incorporation used in this set of experiments. The laser used to excite the sample was the laser unit: Laserstack 488.

Afterwards, 12 z-stacks per time-point were acquired with a magnification of 20x, resolution of  $512 \times 512$  pixels ( $341,33 \mu\text{m} \times 341,33 \mu\text{m}$ ) and pixel size of  $0,667 \mu\text{m}$ . Each z-stack comprised 49 slices whose maximum projections were also generated to be used later.

### **III.1.7. *CellProfiler* software and RStudio for image analysis**

The *CellProfiler*<sup>98</sup> software and *Rstudio* were used to analyze the microscope images, and obtain intensity histograms (Fraction of cells vs *Integrated Intensity*) of each time-point. Microsoft ® Excel was used to perform calculations and GraphPad Prism 7.03 to obtain the final graphs.

*CellProfiler* is a free, open-source software used to perform quantitative analysis of biological images. It works with projects that are composed by an image file list containing the images to be analyzed; a pipeline, the sequential set of modules that analyze input images; and optionally the metadata, that is the associated information about the images. The pipeline is divided in two groups of modules namely *Input modules* and *Analysis modules*. The former group contains the module *Images*, where the location of images to be analysed is specified; the module *Metadata*, that extracts the information about each image; the module *NamesAndTypes*, where a name can be given to all images, or to specific images with certain characteristic extracted from metadata (for example the C number, that is an index given to each channel); and the module *Groups*, where sets of images can be organized in groups. Finally, the *Analysis modules* performs the intended operations to input images<sup>99</sup>. Figure III-6 features the environment of the software. *CellProfiler* software was used to identify the cells and measure their intensities.

RStudio is an Integrated development environment for R language. After obtaining the intensities, a code adapted from *Cell cycle staging of individual cells by fluorescence microscopy* (2015)<sup>68</sup>, was used to obtain the frequency of cells with each intensity, create the histograms (Fraction of cells vs *Integrated Intensity*) and calculate the percentage of cells present in specific histogram regions.

It is important to mention that, in the case of SD Confocal Microscopy, the images analyzed corresponded to the maximum projections of z-stacks.

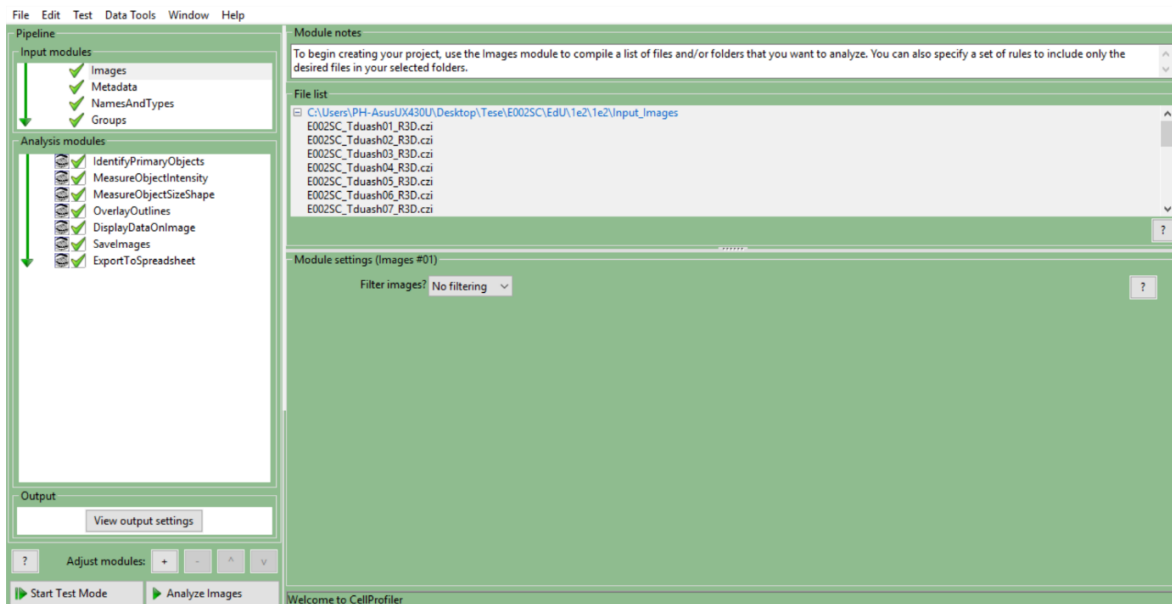


Figure III-6: Environment of CellProfiler Software.

### III.1.7.1. CellProfiler Project 1 - Measuring intensity of EdU-positive cells

We first assessed the duration of S phase (in units of time) according to the founder concept of the E-CFI technique – S phase duration equals the minimum time to reach maximum EdU-coupled fluoresce<sup>100</sup>. For this purpose, we quantified the fluorescence of EdU-positive cells for each time point of incorporation of EdU. After loading the images, the metadata was extracted using the method *Extract from image file headers*, to obtain the internal information of the files (Figure III-7). Then, in *NamesAndTypes* module, the channel of interest was chosen based on C number, present in images metadata. During this thesis the images were not organized in groups, so after *NamesAndTypes*, the next step was to construct the set of Analysis Modules. The set of modules was as follows: *IdentifyPrimaryObjects*, *MeasureObjectIntensity*, *MeasureObjectSizeShape*, *OverlayOutlines*, *DisplayDataOnImage*, *SaveImages* and *ExportToSpreadsheet*. In table III-4 the features of each module are shown. Here, the critical module for this project was the *IdentifyPrimaryObjects*, which performs the identification of cells in the images. Its settings were carefully analysed and optimized in order to obtain the most accurate identification. In table III-5 are the main settings of this module, such as the typical diameter of nuclei in pixels, the threshold strategy, the method to distinguish clumped objects and the method to draw dividing lines between clumped objects.

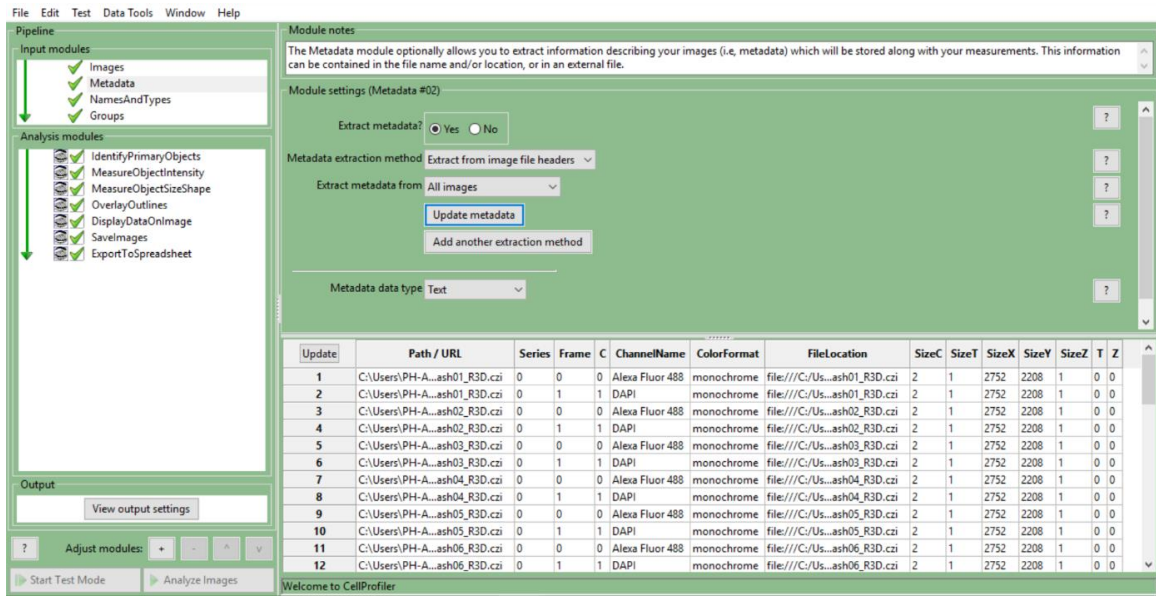


Figure III-7: Images Metadata.

Table III-4: Set of Analysis Modules.<sup>99</sup>

Modules	Features
<i>IdentifyPrimaryObjects</i>	Identifies objects according to several parameters.
<i>MeasureObjectIntensity</i> ,	Measures several intensity features of selected images and objects.
<i>MeasureObjectSizeShape</i>	Measures several area and shape features of selected objects.
<i>OverlayOutlines</i>	Places outlines over the desired images.
<i>DisplayDataOnImage</i>	Creates an image with a certain measure regarding the whole images or identified objects.
<i>SaveImages</i>	Saves the selected images on the output file location.
<i>ExportToSpreadsheet</i>	Exports the measurements into a file, to the output file location.

Table III-5: Main Settings of *IdentifyPrimaryObjects* module.

Settings	
Typical diameter of objects, in pixel units (Min,Max)	40-75
Discard objects outside the diameter range?	Yes
Discard objects touching the border of the image?	Yes
Threshold strategy	Global
Thresholding method	Otsu
Two-class or three-class thresholding?	Two classes
Method to distinguish clumped objects	Shape
Method to draw dividing lines between clumped objects	Shape
Retain outlines of the identified objects?	Yes

The threshold strategy dictates the type of input used to calculate the threshold value, while the thresholding method is the method to calculate the threshold value. The threshold strategy *Global* was used to calculate a single threshold value based on the pixels of the input images. The *Ostu* method calculates the value of the threshold separating the pixels in two classes, background and foreground, and minimizing the variance within each class.<sup>99</sup>

After identifying the cells, their intensities were measured using the module *MeasureObjectIntensity*, which records several measurements of intensity for each object such as, for example, *IntegratedIntensity*, *MeanIntensity*, *MaxIntensity*, among others. In the module *DisplayDataOnImage*, the measurement chosen to display on images was the *IntegratedIntensity* (in Integrated Intensity Units), that is the sum of pixel intensities within an object. Throughout this thesis work, *IntegratedIntensity* was the measurement used to analyze the signal within cells.

In the end of the project, images with the identified cells (outlines overlaid) and their respective *IntegratedIntensity* displayed were saved in the *Default Output Folder*, using the module *SaveImages*. Also, the data measured was exported to a .txt file, using the module *ExportToSpreadsheet*.

### **III.1.7.2. *CellProfiler* Project 2 - Measuring intensity of EdU negative cells**

The DNA stain intensity within cells EdU negative was measured in order to quantify duration times of G1 and G2-phases<sup>100</sup>. For this purpose, *CellProfiler* was used to eliminate EdU positive cells, and thus obtain images with the desired cells (DNA stain positive, EdU negative). A correct elimination requires an extremely well identification. This stringency was only achieved using the *Manual* strategy to establish the threshold value, since this allowed us to obtain the most accurate value for each time-point of each experiment. Therefore, the first step of this analysis was to obtain those values, using a Preliminary Project.

#### **III.1.7.2.1. Preliminary Project**

This Project was identical to the one in III.1.7.1 (*CellProfiler* Project 1), with the same set of modules namely *IdentifyPrimaryObjects*, *MeasureObjectIntensity*, *MeasureObjectSizeShape*, *OverlayOutlines*, *DisplayDataOnImage*, *SaveImages* and *ExportToSpreadsheet*. There were only differences in the *IdentifyPrimaryObjects* settings. For this specific module the Threshold Strategy used was *Manual* instead of *Global*, the range of typical diameter was broader (e.g. 38-90), and the method to distinguish clumped objects and the method to draw dividing lines between clumped objects were *Intensity* instead of *Shape*.

To help determining the threshold values, the display window of the module *IdentifyPrimaryObjects* was activated. This window is very useful because it shows not only the result of the module after

processing, but also some details about the process and data concerning the image. More specifically, the display window of *IdentifyPrimaryObjects* presents one table and three images (Figure III-8 and Figure III-9). The table shows several data about the image, as the threshold selected by the user and the number of accepted objects calculated by the module. The upper left image is the input image. The upper right image shows the objects identified with arbitrary colors to be easily distinguished, where the same color is assigned to pixels that belong to the same object. Finally, the lower left image shows the input image with colored outlines indicating the accepted objects (green outlines) and the discarded objects (magenta and yellow discarded due to, respectively, either size or object in the borders) <sup>99</sup>.

Figure III-9 A) and B) are zooms of figure III-8. Figure III-9 A) presents examples of cells discarded in the borders, outlined in yellow, while figure III-9 B) presents one example of a cell outlined in red, discarded based on size. In the bottom bar of the display window appears the value of intensity of the pointed pixel.

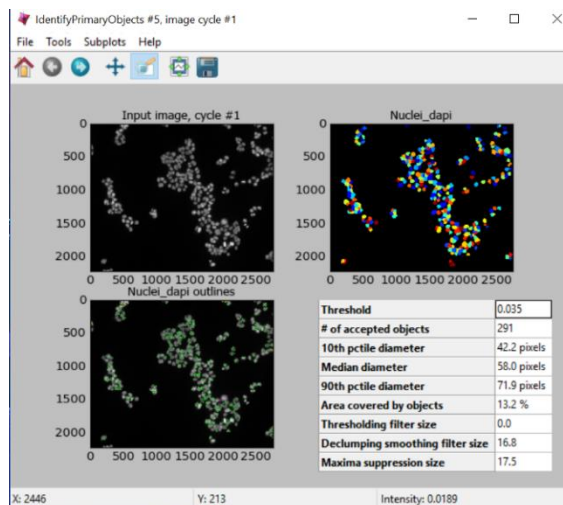


Figure III-8: Display window of *IdentifyPrimaryObjects* module.

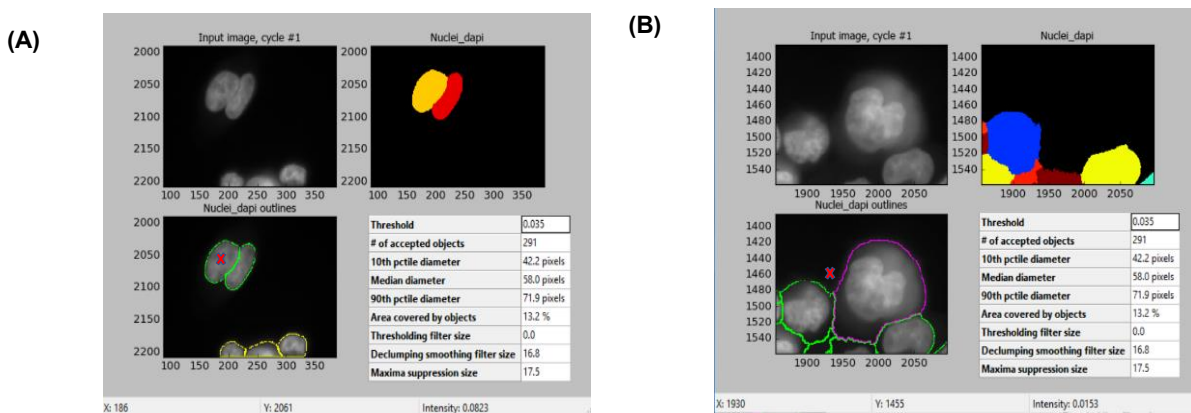


Figure III-9 Zooms of figure III-9 with cells discarded: (A) in the borders outlined in yellow, and (B) based on size outlined in magenta. The values of intensities present in the bottom bar correspond to the pixels pointed out with the red crosses. In this example the threshold is 0.035, the pixel intensity in (A) is higher (0.0823 – classified as foreground), and the pixel intensity in (B) is lower (0.0153 – classified as background).

Thus, this feature was used to understand whether with the chosen threshold values cells were correctly identified, and if there were cells that remained unidentified. In this way, values were optimized for each time-point of each experiment. This was performed for both channels, (EdU and the DNA stain

used) through adapting the value of C number in *NamesAndTypes*. Besides the alterations already mentioned, this Preliminary Project was performed exactly like the project in III.1.7.1, including the exporting of data to be used later.

### III.1.7.2.2. Main Projects

After obtaining the threshold values, the main project was constructed with two sub-projects (part 1 and part 2) which were run consecutively: part 1 where the images with the cells of interest (cells EdU negative) were created and part 2 where the intensities of those cells were measured and recorded. Starting with part 1, the set of modules was *IdentifyPrimaryObjects*, *IdentifyPrimaryObjects*, *MaskImage*, *MaskImage*, *ImageMath*, *ImageMath* and *SaveImages*. The modules *IdentifyPrimaryObjects* identified the cells of each channel with diameters similar to the ones selected on preliminary project (e.g. 30-95). As mentioned, the threshold strategy was *Manual* and the values of threshold were the ones established in the Preliminary Project (section III.1.7.2.1). The module *MaskImage* hides certain parts of the input image, creating a mask, while the module *ImageMath* performs mathematical operations on image intensities<sup>99</sup>. Two masked images were generated during this project, one for each channel. Both were created based on the objects previously identified, in order to mask out the portions of the images without those objects. After creating the mask on each channel, two *ImageMath* modules were used to finally eliminate EdU-positive cells. First an image with the cells to be eliminated was created, and then these cells were subtracted to the image with total cells. To do so, the first *ImageMath* module performed the operation *And*. This operation receives two input images (masked images obtained in the previous modules) and classifies the pixels of the output image as foreground only if the correspondent pixels of both input images are also foreground<sup>99</sup>. The output image obtained was a binary image, with background in black and foreground in white. Figure III-10 shows the display window of this module. The upper left and right images are the input images. The lower left image is the output obtained after the mathematical operation *And*.

In the second *ImageMath* module the operation *Subtract* was used, which receives two images and subtracts the second image from the first one<sup>99</sup>. The first one is an image with intensities between 0 and 1, while the second one is a binary image, whose foreground and background values are 1 and 0 respectively. So, this operation attributed the value zero (black pixels) to those pixels present in the second image with the value 1. In table III-6 is a sum-up of the Inputs and outputs used on each Module. The final module of part 1, *SaveImages*, saves the created images in the *Default Output Folder*.

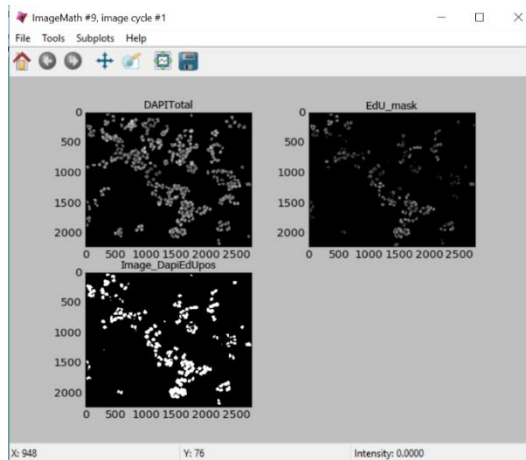


**Figure III-10: Display window of ImageMath Module – operation And.**

**Table III-6: Sum-up of Inputs and Outputs used in each Module of Main project - part 1.**

Modules	Inputs	Output
<i>IdentifyPrimaryObjects</i>	Input Image (channel1)	Objects (channel1)
<i>IdentifyPrimaryObjects</i>	Input Image (channel2)	Objects (channel2)
<i>MaskImage</i> ,	Input Image (channel1); Objects (channel1)	Mask (channel1)
<i>MaskImage</i> ,	Input Image (Channel2); Objects (channel2)	Mask (channel2)
<i>ImageMath (And)</i>	Mask (channel1); Mask (channel2)	Image (with cells to eliminate)
<i>ImageMath (Subtract)</i>	Mask (channel1); Image (with cells to eliminate)	Final image

The set of modules of part 2 is the same has in Preliminary Project (section III.1.7.2.1): *IdentifyPrimaryObjects*, *MeasureObjectIntensity*, *MeasureObjectSizeShape*, *OverlayOutlines*, *DisplayDataOnImage*, *SaveImages* and *ExportToSpreadsheet*. Regarding *IdentifyPrimaryObjects*, the range of typical diameter chosen became smaller again (e.g. 40-80), the value of threshold used was the same as used in part 1 for this channel and the method to distinguish clumped objects and the method to draw dividing lines between clumped objects were *Shape* instead of *Intensity*. In the end of part 2, the *Integrated Intensities* (among other measurements) of the identified cells were exported to be used later.

The values of threshold selected on Preliminary Project are depicted in Table VII-1 of annexes.

### **III.1.7.3. RStudio**

Rstudio was used to analyse the data obtained from *CellProfiler*. The code (Figure VII-8 of annexes) generated the histograms Fraction of cells vs *Integrated Intensity* for each time-point of each experiment. The data file created by *CellProfiler* has all the information organized as follows: each row represents a different object and each column represents a different measurement. The code reads this file and extracts the desired data, which in this case is the *Integrated Intensity* of each object. Sometimes the images of several time-points were analyzed together, so the code is also able to identify the time-point correspondent to the image (named as timepoint in the code), by extracting it from the image file name.

There were several inputs that needed to be established, such as the location of the data file, created by *CellProfiler*, with all the measurements, and some information about the histograms, including the maximum value of x axis, bin width and the dimensions of the output image. The code reads the data file, extracts the information and constructs the histograms, one for each time-point.

Besides histograms, the code also generates two .txt files with percentages of cell cycle distributions based on Histograms (CellCycle\_Percentages\_table) and the frequencies of cells for each binned value (CellCycle\_BinnedFrequencies\_table).

For each time-point, the directory of the file data was adapted, along with the corresponding time-point, indicated in the vector treat.levels. For each experiment, the name was also adapted. More specifically, this name was given to the images in the Main Project-part2. In table III-7 are some functions used to establish the inputs, where the *Name* is the name of the experiment mentioned.

**Table III-7: Functions used to establish the inputs**

Function	Description
Setwd()	Sets the working directory
Name.max	Sets the maximum value
Name.bin.width	Sets the bin width
Name.widht	Sets the width in inches for the histogram .png file
Name.height	Sets the height in inches for the histogram .png file

### **III.1.8. Statistical analysis**

Graphs with mean values present error bars which represent standard deviations. GraphPad Prism 7.03 does not draw the error bars when error bars were shorter than the height of the symbol.

## **III.2. Hair follicle characterization**

### **III.2.1. EdU incorporation**

Human scalp biopsies used throughout this work were obtained from *Hospital CUF Descobertas* (transplantation biopsy with 1-1.5 mm diameter – experiment 1) and *Hospital de Santa Maria* (punch biopsy with 3-4mm diameter – experiment 2), after obtaining informed consent from patients. Culture media containing EdU were prepared through dilution of a stock of 10mM EdU in DMSO to a final concentration of 10 or 15 µM (experiment 1 and 2 respectively), in ProCHO™ 4 medium (04-919Q, Bio Whittaker®, Lonza) supplemented with 2mM L-glutamine, and 100U/ml penicillin/streptomycin (both from Gibco®). Biopsies were incubated with the prepared culture medium during 12h or 4h (experiment 1 and 2, respectively), at 37°C in a humidified atmosphere containing 5% CO<sub>2</sub>. After incubation, biopsies were fixed in 4% FA in PBS at 4°C, for 8 weeks and 6 days (experiment 1 and 2, respectively).

### **III.2.2. Preparation of samples, inclusion and sectioning**

After several washes in PBS, human scalp biopsies were incubated at 4° C overnight in the hydrogel monomer solution A4P0 (4% (w/v) acrylamide in PBS), supplemented with 0.25% (w/v) photoinitiator 2,2'-Azobis(2-(2-imidazolin-2-yl) propane) dihydrochloride (VA-044, Wako Chemicals). Afterwards, the A4P0-infused samples were degassed with nitrogen for 1-5 minutes and incubated for 1-3 hours at 37°C to initiate polymerization. Then, biopsies were washed with PBS and transferred into 50 mL Falcon tubes containing 8% (w/v) SDS in PBS (ph7.5), and they were incubated for 5hours at room temperature and 1h at 37°C, with mild shaking. Biopsies were then incubated with 20% (w/v) sucrose (Sigma®) in PBS during 16-48h.

After preparing the biopsies, they were included and sectioned in the Histology and Comparative Laboratory of Instituto de Medicina Molecular/IMM-João Lobo Antunes, Lisbon. Biopsies were embedded in a solution of 7.5% (w/v) gelatin plus 15% (w/v) sucrose (both from Sigma®), in PBS and placed in a water bath at 37°C for 1-3h. After, biopsies were removed from the water bath and included between two layers of gelatin (Sigma®), which were added gradually, as follows: first layer of gelatin (takes 30 minutes to set), then the biopsy and finally the second layer of gelatin (30min to set). Afterwards, the obtained block was cut with a scalpel to choose the right orientation that is to allow sectioning of hair follicles mainly longitudinally. Subsequently, blocks were frozen with Isopentane, cooled with liquid nitrogen and stored at -80°C. Sections with an average thickness of 5µm were obtained using the cryostat Leica CM 3090S, and stored at -20°C until used.

### **III.2.3. EdU staining and Immunofluorescence**

Firstly, gelatin was removed by incubating the microscope slides inside of a closed container, immersed in a water bath at 42°C, for 30 minutes. This was not performed in experiment 1.

Subsequently, sections were washed three times with PBS/ 0.05%Triton X-100 and the water repelling (hydrophobic) DakoPen (Dako) was applied around the sections in order to create a barrier against the spreading of reaction solutions. Then sections were incubated 20 minutes with the reaction cocktail prepared from the Click-iT® EdU Alexa Fluor® 488 Imaging kit (section III-1.3; Table I-1).

After EdU staining, some sections were also stained with cytokeratin(CK)-15. For this purpose, they were incubated with a mouse primary antibody anti CK-15 (1:100, ab80522, abcam) for 1 hour at 37°C. Subsequently, sections were washed three times with PBS/ 0.05%Triton X-100 and incubated with a secondary antibody cy3 goat anti-mouse (1:100, abcam) for 1 hours at 37°C. After the incubations, they were washed again with PBS/ 0.05%Triton X-100 and the signal was fixed with 2% FA in PBS for 10 minutes.

Staining of DNA using DAPI or Hoechst 33342 was also performed using the concentrations indicated in table III.2 of section II.1.4. To this end, after immunostaining sections were washed in PBS 0.05%Triton X-100 and incubated in the dark, for at least 4 hours at room temperature.

Finally, after washing again with PBS/ 0.05%Triton X-100 microscope slides were mounted in VECTASHIELD® and stored at -20°C.

### **III.2.4. Image acquisition using Confocal Point-Scanning Microscopy**

The Confocal Point-Scanning Microscope Zeiss LSM 710 was used to acquire the images. A multi-channel acquisition was performed namely DAPI or Hoechst and Alexa 488, or DAPI or Hoechst and Alexa 488 and CK-15 (triple acquisition). The software ZEN 2 (black edition) was used to establish the appropriate settings for image acquisition. The set up was performed at the beginning of each acquisition session. More specifically, two or three tracks were established to acquire the images, depending in whether CK-15 was also included or not. For each track the main features established were the laser selection and the respective percentage of laser intensity to be used, the pinhole size and the gain. A pinhole size of  $2.1 \pm 0.1 \mu\text{m}$  was used throughout all acquisitions. DNA stain excitation was performed using a 405nm line from the laser unit Diode 405-30, Alexa 488 excitation was performed using a 488nm line from the laser unit Argon and CK-15 excitation was performed using a 561nm line from the laser unit DPSS 561-10.

The remaining parameters were adapted individually for each experiment. The choice of the laser was also supported by ThermoFisher Scientific online tool, *Fluorescence Spectra Viewer*.

Acquisition of images was performed for different anatomical areas of hair follicle (bulb, sub-bulge, bulge and supra-bulge), epidermis, and sebaceous gland, with a magnification of 20x or 10x, resolution of  $1024 \times 1024$  pixels ( $708.49 \times 708.49 \mu\text{m}$  or  $1416.99 \times 1416.99 \mu\text{m}$  respectively) and pixel sizes of  $0.60 \mu\text{m}$  and  $1.31 \mu\text{m}$  respectively.

### **III.2.5. Image analysis and quantification using Fiji**

After acquiring hair follicle images these were organized according to anatomical areas (bulb, sub-bulge, bulge and supra-bulge) before analysis. The image processing package Fiji<sup>101</sup> was utilized herein for image processing. As described, “Fiji is a distribution of ImageJ together with Java, Java 3D and several plugins organized into a coherent menu structure”<sup>102</sup>. The cell counter plug-in was used to count cells stained with EdU in the bulb and sub-bulge. The remaining areas were qualitatively analyzed, in the same way as the images of epidermis and sebaceous gland. To help in the analysis of these images some sections were subsequently stained with Orcein-Giemsa after immunostaining. Microsoft ® Excel was used to perform calculations and GraphPad Prism 7.03 to obtain the final graphs.

### **III.2.6. Orcein-Gimsa protocol**

Microscope slides previously subjected to immunostaining were disassembled and washed in Elix® water. Sections were then stained in Orcein (Merck) for 30 minutes, and the background was reduced by a short immersion in 95% EtOH (Merck). After washing the sections with running water for 10 minutes, they were stained in 1% Gimsa (Merck) for 1h at room temperature. The excess of blue shades was removed by placing the sections in a 95% EtOH with some drops of eosin (Merck). A Phase Contrast microscope (*Zeiss Primovert*) was used to observe the microscope slides throughout the procedure. In the end, they were mounted in DPX (gurr®) mounting medium.

Images were acquired using a brightfield microscope *Leica DM2500*, with a magnification lens of 20× (pixel size=0,3μm).

### **III.2.7. Statistical analysis**

Graphs with mean values display error bars which represent standard deviations. GraphPad Prism 7.03 does not draw the error bars when error bars were shorter than the height of the symbol.

### **III.3. Preparation of hair follicle cell suspension from human biopsies**

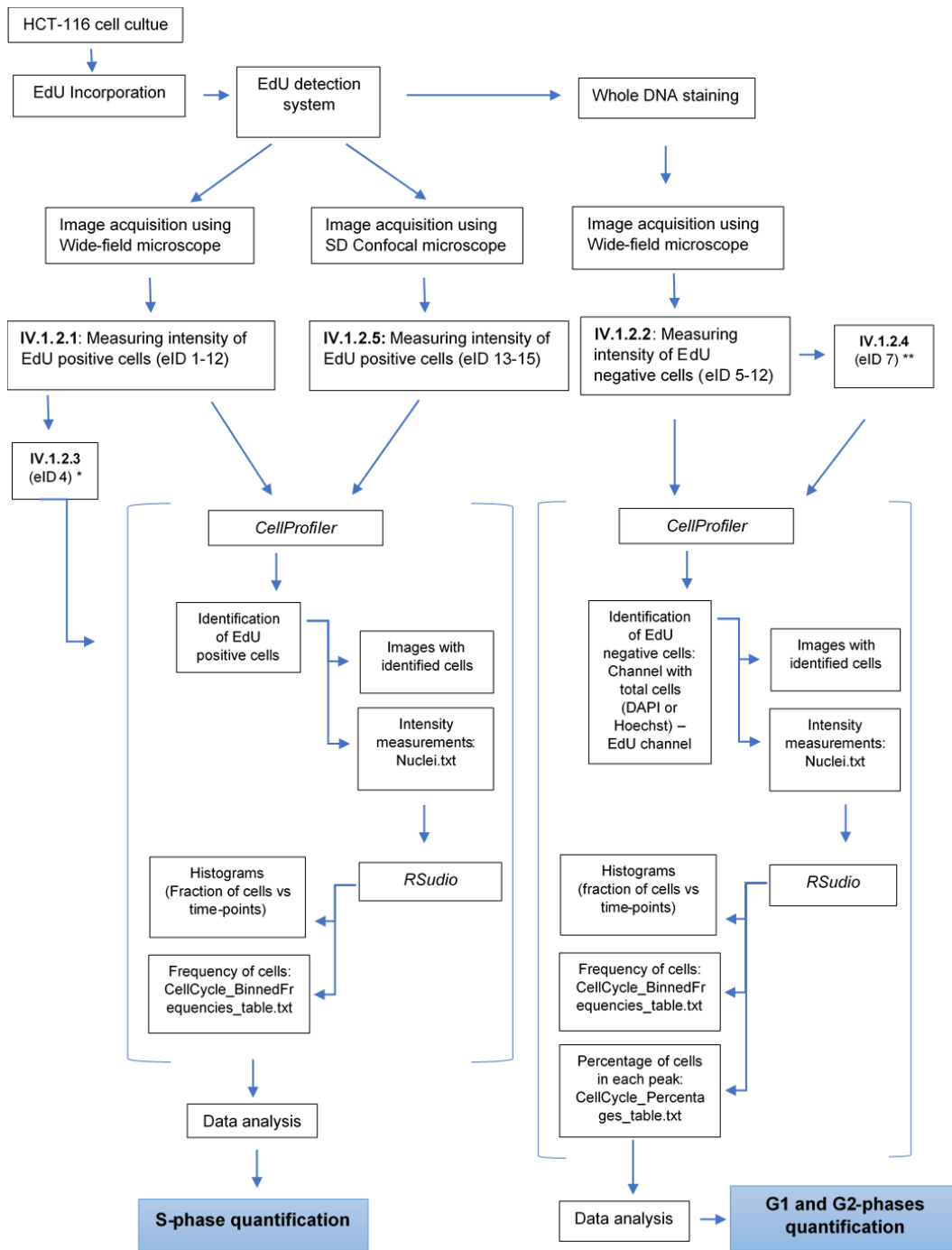
Human scalp biopsies used for HFSCs isolation were obtained from *Hospital de Santa Maria*, after obtaining informed consent from patients. HF biopsies were minced in approximately 1 mm fragments with the aid of a scalpel. Then the fragments were incubated in HBSS (Gibco®) supplemented with 1mg/mL collagenase/dispase (Sigma®), prepared from a stock of 10mg/mL in PBS, overnight at 37°C. Fragments disruptions was aided by vigorous pipetting, resulting in HFs separated from surrounding dermis. The excess of collagenase/dispase was removed by two washes in HBSS. The HFs were then incubated with trypLE™ Express for 20-30 minutes at 37°C. Afterwards, the disruption of epithelial cells from HFs was achieved by vigorous pipetting. TrypLE was quenched by adding of an equal volume of HBSS supplemented with 10% Fetal calf serum (Gibco®). Free cells and tissue debris were then centrifuged (350xg, 7 minutes) and subsequently resuspended in HBSS, passed through a 100 µM diameter mesh (cell strainer, Falcon®) and centrifuged again as above. Free cells and small aggregates were then resuspended in 5mL of fully supplemented (as per manufacturer instructions) CnT07 medium<sup>87</sup> (CellnTech), additionally supplemented with 100U/ml penicillin/streptomycin (Gibco®) and incubated at 37°C in atmosphere containing 5% CO<sub>2</sub>. The media was changed every three days and cells were passaged when sub-confluent.



# IV. Results and Discussion

## IV.1. Cell cycle quantification using Microscopy

### IV.1.1. Outline



\*Cell cumber Influence on S-phase quantification. Experiment 4 with different number of input images: 2,4,6,8,12,18.

\*\*Cell cumber Influence on G1 and G2-phases quantification. Experiment 7 with different number of input images: 2,4,6,9 and 12. On this analysis G1 and G2-phases were not quantified. The histograms were obtained for time-points for time-points T1h and T4h;

## IV.1.2. Experiments sum-up

The first part of Results and Discussion consists in adapting a tool developed previously for the quantitative assessment of the cell cycle by flow cytometry, termed E-CFI (EdU-coupled fluorescence intensity analysis)<sup>100</sup>, but for microscopy-based analyses. In addition, the method used for cell cycle quantification using microscopy was further adapted from a paper of Roukos et al. (2015), where they established a protocol for determining cell cycle staging through measuring DNA content using microscopy<sup>68</sup>.

The table IV-1 contains a sum-up of the experiments performed herein. In the present master thesis, the experiments were identified based on the experiment ID (eID). In all of the experiments discriminated below replicating DNA was labeled with EdU. Cellular population from experiments 5 to 12 in addition to EdU-labeling were also labeled for whole DNA with a DNA stain (PI, Hoechst or DAPI). Of note, experiments 11 and 12 comprise two additional time-points (9h and 10h of continuous EdU incorporation). Finally, images in experiments 1 to 12 were all acquired using widefield microscopy, while images of experiments 13, 14 and 15 were acquired using SD confocal microscopy.

**Table IV-1: Experiments sum-up.**

Experiments (eID)	Staining	Microscopy	Time-Points
1	EdU	Widefield	0-8
2	EdU	Widefield	0-8
3	EdU	Widefield	0-8
4	EdU	Widefield	0-8
5	PI + EdU	Widefield	0-8
6	PI + EdU	Widefield	0-8
7	Hoechst + EdU	Widefield	0-8
8	DAPI + EdU	Widefield	0-8
9	DAPI + EdU	Widefield	0-8
10	DAPI + EdU	Widefield	0-8
11	DAPI + EdU	Widefield	0-10
12	DAPI + EdU	Widefield	0-10
13	EdU	SD Confocal	0-8
14	EdU	SD Confocal	0-8
15	EdU	SD Confocal	0-8

After EdU incorporation and EdU detection and DNA staining procedures, images were acquired from areas where cells appeared as individualized as possible in order to facilitate their accurate identification. Therefore, areas with giant cells, cell clusters, image blurring or equivalent caveats were avoided. Despite these unavoidable constraints images were otherwise taken in an unbiased manner.

#### IV.1.2.1. Estimation of S phase duration time

Estimation of S-phase duration time was performed using staining for EdU, since, as already mentioned, this is an easily detectable thymidine analog that is incorporated into replicating DNA during S-phase of the cell cycle<sup>71</sup>. For this purpose we utilized cultured cells (HCT-116) growing asynchronous, which means they were not in the same cell cycle phase at any given time. These cultures were pulsed with EdU for incremental periods of time (1h increments), until a maximum incorporation time of 8h<sup>100</sup>.

In the following figure (Figure IV-1) a scheme regarding the principle of the E-CFI method is represented<sup>100</sup>.

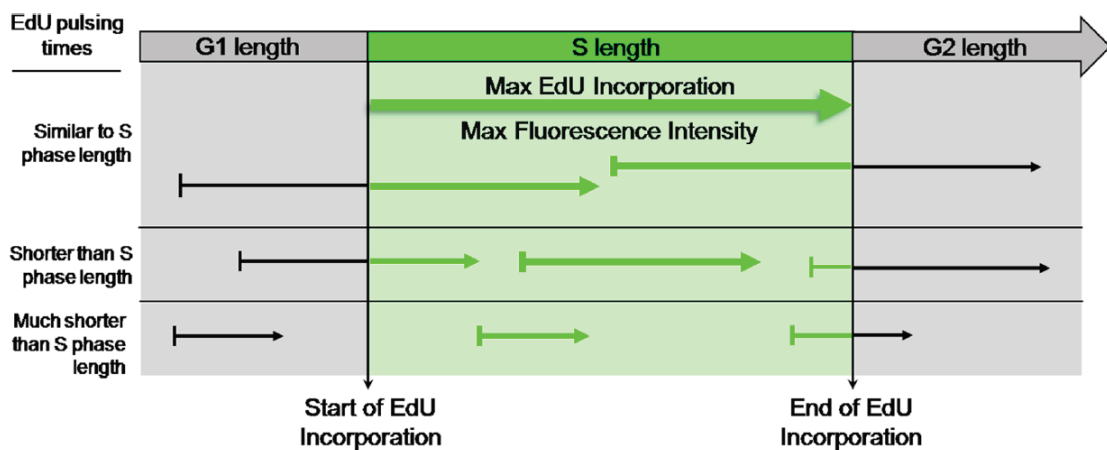


*Figure IV-1: EdU incorporation principal* <sup>100</sup>.

Arrows represent times of incorporation of EdU (pulsing times). In the scheme, these periods are divided in EdU pulsing times much shorter than S-phase, just shorter than S-phase and similar to S-phase. If the incorporation of EdU initiates, for example, in the middle of G1, even in cases of EdU pulsing times similar to S-phase duration time, cells only start incorporating EdU when they enter S-phase. As expected, these cells will not reach maxima of labeling with EdU. However, for cells that were initiating S phase at the beginning of the pulse, incorporation of EdU will encompass the full length of S phase. These cells will thus show maxima of EdU-coupled fluorescence (Figure IV-1: ticker arrow). Increasing EdU incorporation times will just increase the proportion of cells showing intensity maxima but not these maxima per se. Thus, the duration of S phase shall correspond to the minimum time of EdU incorporation to achieve maxima of intensity of EdU-coupled fluorescence<sup>100</sup>. In this master thesis, the duration of S-phase was quantified based on this principle.

The first task, after acquiring the images, was to optimize the settings of *CellProfiler* pipeline (Project 1 – section III.1.7.1). In this case the goal was the correct identification of EdU-positive cells. For this purpose, the typical diameter range chosen was quite restrict in order to just select the cells with typical sizes, and not cases of giant cells or even cell clusters. Another relevant setting was the method selected for distinguish clumped objects and draw dividing lines between them. In this case, the method *Shape* was chosen because the main goal of this analysis was to accurately identify the sufficient number of cells stained for EdU. *Shape* method distinguishes clumped objects and divides them just when defined

indentations separate the objects (rounded shape), avoiding, for example, cell clusters. In figure IV-2 is represented (A) an example of an input image (Alexa 488 channel) from experiment 9, T2h and (B) respective project 1 output image, whose identified cells have their outlines underlined. The red arrow represents an example of a giant cell, not identified by the project.

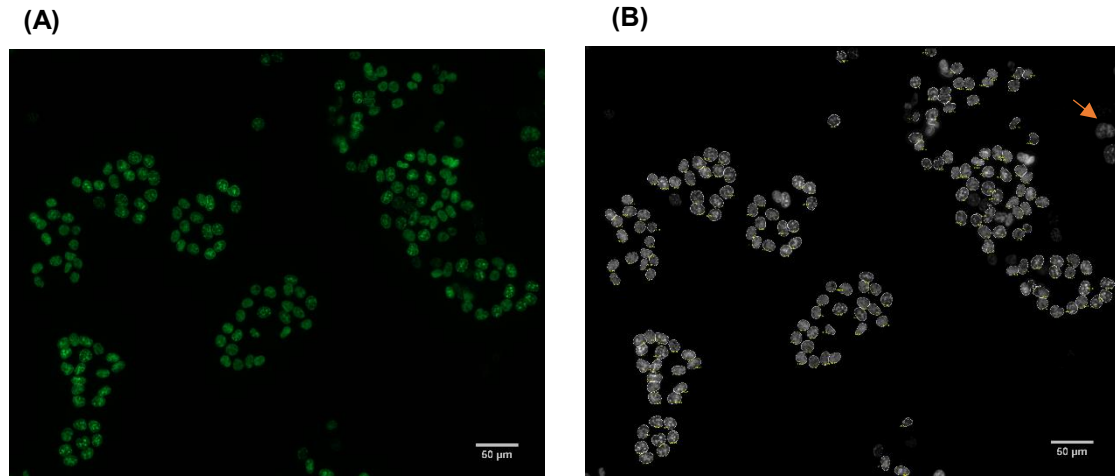


**Figure IV-2:** (A) Widefield microscopy image of experiment 9 (T2h), containing EdU-positive cells. (B) Correspondent output image with EdU-positive cells identified, obtained after running project 1. Scale: 50  $\mu\text{m}$ .

After running the R code, the histograms of Fraction of cells vs EdU *Integrated Intensity*, for each time-point (until T8h) of each experiment were obtained, as well as the file with the frequencies of cells for each bin value. It is important to mention that R code do not return any histogram or document when *CellProfiler* pipeline did not identify any object such as the cases of T0h and T0Ah. Time-points above T8h in experiments 11 and 12 were not considered in this analysis. The histogram obtained in experiment 9, time-point T4h is represented on figure IV-3, with a bin of 4. The whole set of histograms of experiment 9 are in the table VII-2 of annexes (left column).

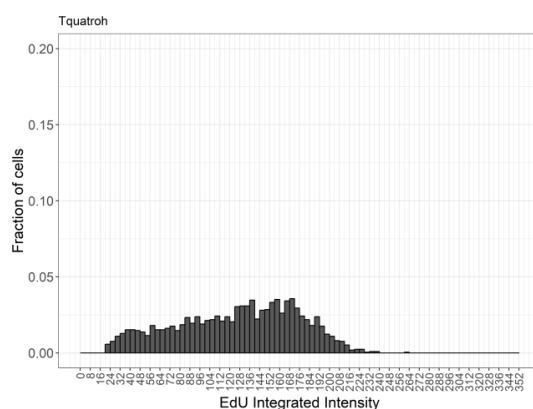


**Figure IV-3:** Histogram fraction of cells vs EdU Integrated Intensities of time-point T4h, experiment 9.

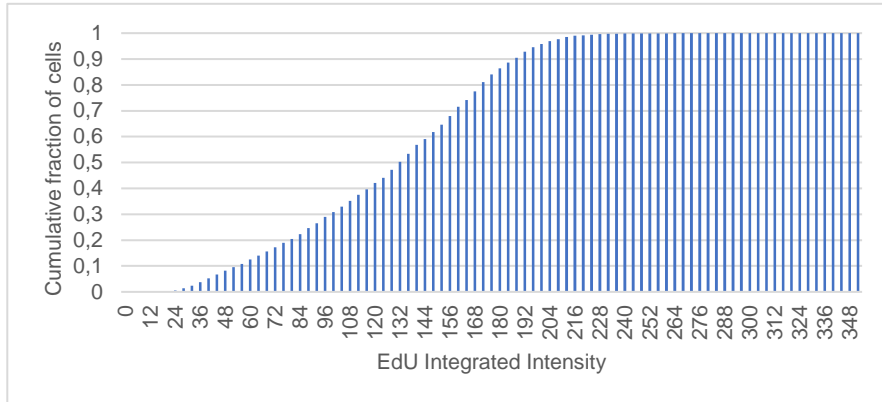


**Figure IV-4: Graph Cumulative fraction of cells vs EdU Integrated Intensity, time-point T4h, experiment 9.**

Along time, several theories have emerged trying to determine the best bin value based on experimental samples<sup>103</sup>. However, in the case of this master thesis project each time-point of each experiment corresponds to a different sample, i.e. number of cells identified using *CellProfiler*. In addition, within an experiment, the graphs of each time-point are analyzed together and, the results of each experiment are compared with each other, so the bin chosen is the same for all histograms, i.e. bin= 4.

These graphs did not allow an easy and simple perception about the time point where the maximum intensity is achieved. So, the graphs Cumulative fraction of cells vs EdU *Integrated Intensity* were created, which are much more illustrative. Figure IV-4 represents this graph for time-point T4h of experiment 9. The whole set of graphs of experiment 9 are in table VII-2 of annexes (right column).

To calculate the cumulative fraction of cells is required a prior estimation of the fraction of cells based on values of frequencies obtained from R code. It is important to mention that frequencies returned by R code (table IV-2) are the number of cells identified in each intensity interval {[0, bin[; [bin, 2bin[; ...].

**Table IV-2: Frequencies of cells for each bin value present on: CellCycle\_BinnedFrequencies\_table.txt.**

Bin	Freq
bin	Frequency 1
2bin	Frequency 2
...	...

For a certain intensity X (bin value):

$$Fraction(X) = \frac{Frequency(X)}{Total\ cells\ of\ the\ sample} \quad (1)$$

$$Cumulative\ Fraction = (Previous\ Cumulative\ Fraction) + Fraction(X) \quad (2)$$

When the cumulative fraction of cells achieves the value 1, with a correspondent intensity Y, this means that there are no identified cells in the sample with intensity higher than Y. So, the maximum Intensity of each time-point is the lowest value of EdU *Integrated Intensity* for which the cumulative

fraction of cells is approximately 1. Thus, these graphs are very useful to understand the progress of *Maximum Integrated Intensity* along time-points. Looking at the example depicted in table VII-2 of annexes, there is a clear progress until time-point T6h, followed by a slight progress between time-points T6h and T7h and, finally, stabilization between T7h and T8h.

Since this analysis was performed based on *Maximum Integrated Intensity* values, the graph Maximum EdU *Integrated Intensity* vs time-points was created for each experiment. This graph allows a better understanding of the maximum intensity progress and summarizes the essential information needed to correctly estimate S-phase duration.

In order to eliminate some artifacts, the values of *Maximum Integrated Intensity* used for tracing these graphs were the values which correspond to a fraction of 0,98 EdU-positive cells. The value of 0,98 was selected and not 1 in order to eliminate a minor fraction of cells with unusually high values of intensity. These latter cells most likely correspond to artifacts, either biological (e.g. polyploid, giant cells, clusters of cells) or technical. As an example, looking at the histogram in figure IV-3, the fraction of cells with EdU *Integrated Intensity* equal or higher than 212/216 is very low, compared to the fraction of cells presented by previous bin-intensities. So, those objects may represent artifacts, and their intensities were excluded from the graphs Maximum EdU *Integrated Intensity* vs time-points. We also tested the value of 0,95, however 0,98 seemed to be more suitable.

Since what truly matters for S-phase estimation is the time-point where maximum intensity of EdU-coupled fluorescence is reached, the value of maximum intensity itself is not relevant. In fact, different experiments present different ranges of intensities. In order to analyze the experiments, namely their behavior along time-points, the values of maximum intensities were normalized for a maximum value of 300. Table VII-3 of annexes depicts the individual graphs obtained for all experiments.

Graphs Maximum EdU *Integrated Intensity* vs time-points summarize the data from all experiments. In 12 experiments, 8 clearly reached maximum EdU intensity between T6h and T7h (experiments 2,3,4,6,7,9,10 and 12), showing that values for maximum EdU-coupled fluorescence intensity stabilized until the T8h time-point was reached; in 3 experiments (experiments 5, 8 and 11) stabilization was achieved between T6h and T7h, however this was not maintained between T7h and T8h; and in 1 additional experiments (experiments 1) intensity values did not stabilize, presenting a linear progress of *Maximum Integrated Intensity* over time (table VII-3 a of annexes).

Figure IV-5 (A) depicts the graph Maximum EdU Integrated Intensity vs time-points of experiments that reached maximum fluorescence intensity between T6h and T7h. The observed stabilization of fluorescence intensities between T6h and T8h means that maximum intensity was achieved, at least for the subset of cells that incorporated EdU for the whole S-phase, after a minimum of 6hours of EdU incorporation. A higher temporal resolution would require incorporation times with shorter increments of EdU pulsing. However, this still provides a good approximation since analyzing the data on figure IV-5 it is clear that in T7h maximum intensity was already reached. This means that the duration of S-phase is between 6-7h.

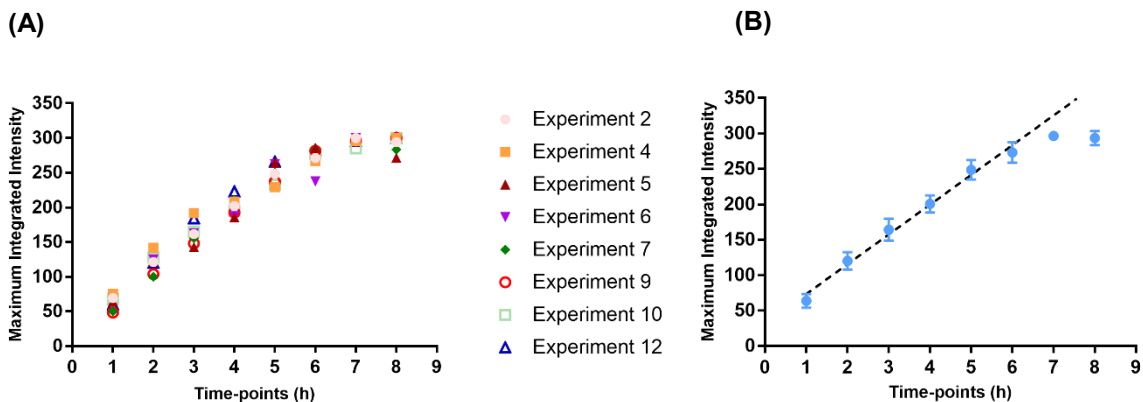


**Figure IV-5: Maximum EdU Integrated Intensities along time-points (experiments 2, 4, 5, 6, 7, 9, 10 and 12).** (A) Actual values of each experiment; (B) Average values ( $n=8$ ); The tendency line (dashed line) represents the linear increase of maximum Integrated Intensity until T6h; Values displayed as mean  $\pm$  standard deviation.

Figure IV-5 (B) represents the graph with the maximum *Integrated intensities* averages and respective standard deviations for each time-point ( $n=8$  experiments). The dashed line represents the tendency line, corresponding to the linear increase of *Maximum Integrated Intensity* along those time-points. After T6h, the values corresponding to time-points T7h and T8h stabilize, not displaying linear progression behaviour. The values for standard deviations, which represent how much the values of each experiment differ from the mean value, are low suggesting good consistency between experiments.

In sum, this analysis allowed the estimation of the duration of S-phase (in units of time) in a simple and reproducible way. In the original research where E-CFI method was established an S phase duration of 6.8 hours was obtained for the same cell-line (HCT-116) using flow cytometry, which is in excellent agreement with the data shown here using quantitative fluorescence microscopy<sup>100</sup>.

#### IV.1.2.2. Estimation of G1 and G2 phases duration times

In order to estimate G1 and G2-phases duration times, whole DNA staining in addition to EdU staining was performed with DAPI, Hoechst or PI. As already mentioned, the relative distribution of cells along the different stages of the cell cycle can be easily appreciated in “cell cycle curves” obtained by flow cytometry that depict relative amounts of DNA, i.e. 2n, 4n and intermediate between 2n and 4n (figure I-6). The E-CFI method also couples this information to that of EdU-associated fluorescence intensity to gather absolute values on the duration (in units of time) of each cell cycle stage. Here, we implemented the methodology of E-CFI for analysis of the cell cycle using fluorescence microscopy. As can be appreciated below, cell cycle curves similar to those seen by flow cytometry can also be obtained by microscopy (Figure IV-7).

The durations of G1 and G2 phases can be estimated from the dynamics of disappearance of the corresponding peaks in the population of cells that remains EdU-negative with increasing pulsing times with EdU. Indeed, over time, EdU-negative cells in G2 (4n DNA content) enter G1 (2n DNA) stage of the next cell cycle leading to a progressive exhaustion of the G2 peak. Then, expectedly, the EdU-negative

G1 peak subsides later, over a period corresponding to the sum of G1 plus G2 phases. In this way it is possible to quantify durations (in units of time) of G2 and G1 plus G2 phases, with the duration of G1 being obtained by inference i.e. by subtracting the duration of G2 phase from the total time that the G1 peak takes to disappear (since the beginning of EdU incorporation). Using E-CFI in flow cytometry, Pereira and colleagues (2017) concluded that the G1 and G2 peaks of EdU-negative cells represent robust markers for the duration of G1 and G2 phases<sup>100</sup>. During this master thesis these same peaks were obtained by fluorescence microscopy and were, in the same way, utilized to quantify G1 and G2-phases.

The quantification of the duration of G1 and G2 phases was performed in 5 experiments: 7, 8, 9, 11 and 12. Of note, experiments 11 and 12 have 10 time-points instead of 8. After staining cells (EdU and whole DNA), and acquisition of images, the following step was selecting the cells of interest (i.e., EdU-negative) in order to obtain cell cycle curves of those cells. This analysis is more complex, than the previous one (quantification of S-phase), since requires the elimination of the population of EdU-positive cells. Project 2 on *CellProfiler* (section III.1.7.2) was used, which contains a preliminary project and the main project which, in turn, is divided in part 1 and part 2.

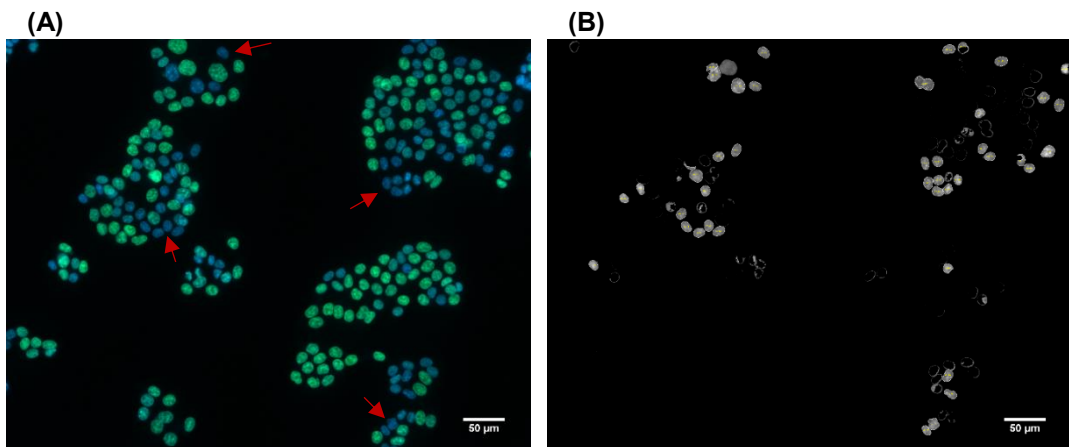
The critical step in this procedure was the correct elimination of EdU-negative cells. To do so, cells were identified in both channels to detect EdU-Alexa 488 and either DAPI or Hoechst, (Main project, part1). During this project the strategy used to calculate the threshold value was *Manual*, allowing the estimation of the best threshold values specific for each time-point since each one features a different set of intensities of EdU-coupled fluorescence. For example, time-points T1h and T2h present many more cells with low fluorescence intensities than time-points T7h and T8h, given the shorter time for incorporation of EdU in the former time points. A low threshold value in a higher time-point of EdU incorporation (eg, T7h-T8h) can lead to the identification of objects as foreground which is not truly representative. Then, the identified objects are just a set of background pixels which do not present a value of 0. Conversely, high threshold values can lead to a lack of identification of certain cells with intensities lower than threshold. So, shorter time-points of EdU incorporation (eg, T1h-T2h) will require a lower threshold value than longer ones. Therefore, the estimation of each threshold value was done using the preliminary project, as described on section II.1.7.2.1. Those values were subsequently used in the main project (part 1).

Part 1 of Main Project concerns the elimination of cells stained with EdU, while Part 2 relates to the identification of final objects, as well as the measurements and storage of all data.

In Part 1, important settings were established such as the typical diameter of identified objects (nuclei) and the methods selected for distinguishing clumped objects and draw dividing lines between them. The range of typical diameter (of nuclei) chosen was larger than the one in the project used for S-phase quantification. In that case, the main goal was the accurate identification of cells stained with EdU, leaving out several which did not conform to established parameters. Here, the aim was a total identification of cells in each channel (EdU plus DAPI or Hoechst), in order to perform a subtraction (Total cells (DAPI or Hoechst) – EdU-stained cells) to completely eliminate cells stained with EdU. For the same reason, the method for distinguish clumped objects and draw dividing lines between them was

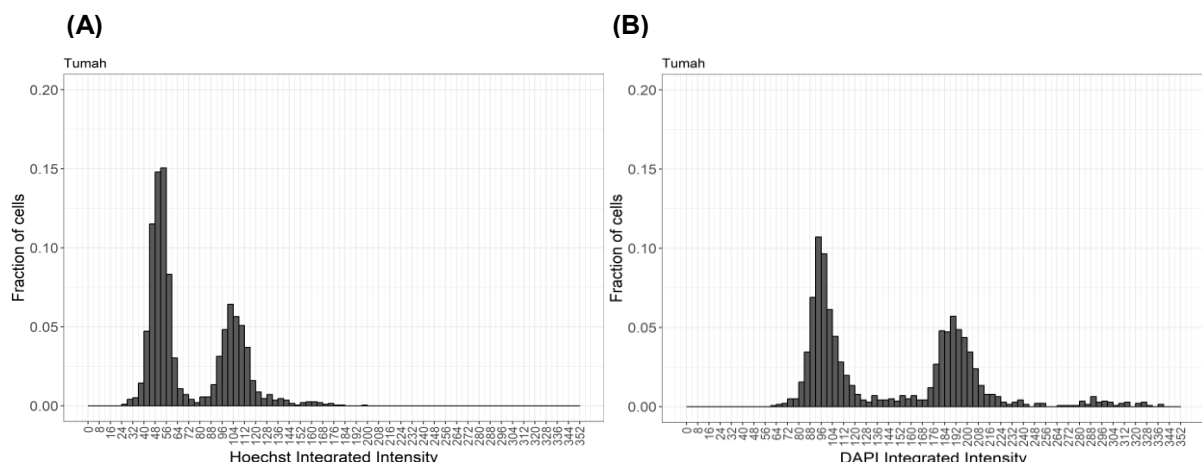
*Intensity* instead of *Shape*, since *Intensity* performs better at distinguishing clumped objects. This can lead to the presence of giant cells or cell clustering on final images of part1, however this will not represent an issue. Indeed, such types of objects will not be identified in part 2 because the diameter returns to a restricted range, and the method used to distinguish clumped objects and draw dividing lines between was, again, *Shape*.

Figure IV-6(A) depicts the original image from experiment 7, time-point T7h, with channels overlapped (blue: Hoechst, green: EdU) and (B) the final image obtained after running project 2. The red arrows indicate some examples of cells not stained with EdU which are present on figure IV-6(B) and identified as an object. The cells identified on figure IV-6(B) have the outlines underlined.



**Figure IV-6:** (A) Widefield microscopy image of experiment 7 (T7h), stained for Hoechst and EdU. (B) Correspondent output image obtained after running project 2. Scale: 50  $\mu\text{m}$ .

After establishing the settings, and running *CellProfiler* and *RStudio*, the histograms of fraction of cells vs DAPI or Hoechst *Integrated Intensity* were obtained. Figure IV-7 represents the histograms of time-point T1h of experiments (A) 7 and (B) 8, in which the DNA stain was, respectively, Hoechst and DAPI. The whole set of histograms of experiment 8 are in table VII-4 of annexes.



**Figure IV-7:** Histograms fraction of cells vs Integrated Intensity (T1h) of (A) experiment 7 (left image) and (B) experiment 8 (right image).

The shape of these histograms is very similar to the usual cell cycle curves obtained by flow cytometry, presenting intensities expected for 2n and 4n DNA contents, that is a G1 (2n) peak with approximately half the intensity of the G2 (4n) peak. This was also observed for experiments 9, 11 and 12. We note that for experiments 5 and 6, in which whole DNA was stained with PI, a double peak could not be obtained; in these experiments a single peak was seen instead. Consequently, the quantification of these experiments did not proceed. In fact, the original E-CFI method was developed using PI to achieve whole DNA staining for analysis by flow cytometry. However, a possible problem of bleed-through between channels precluded further analysis of these data<sup>104</sup>. Since results obtained with DAPI and Hoechst did not present this problem, and their handling did not require the extra step of using RNase to digest RNA, no additional experiments were done using PI.

In addition, the quantification of G1 and G2-phases of experiment 10 was not performed, because the set of input images presented an unusual blurring. Although this did not affect S-phase quantification, it did not allow an accurate identification of whole cells in order to perform the required elimination of EdU-negative cells. In this case, the blurring probably originated during the procedure of mounting the microscope coverslips in anti-fading medium.

The progression of G1 and G2 cells at successive time-points was evaluated by careful analysis of the corresponding histograms. It was clear that the G2 peak disappeared in all experiments (7, 8, 9, 11 and 12) between time-points T4h and T5h of EdU incorporation, consistent with a duration of 4-5h for G2 phase and in close agreement with previously published data for this cell line (HCT-116)<sup>100</sup>. However, this was not so clear with respect to G1 peak.

As mentioned before, the G1 peak shall disappear later than the G2 peak since EdU-negative G2 cells continuously feed into the G1 peak before being drastically reduced, as explained above. However, disappearance of the G1 peak is not always easy to appreciate, due to a decrease of cell number in higher time-points, (for example T9h and T10h of experiments 11 and 12; Table VII-5 of annexes) showing up as a progressively less well defined shape of the histograms.

In order to better analyze the data present on histograms the percentages of cells in G1 and G2 in the total population were estimated for each time-point, based on the percentage of cells within each peak. Percentages of cells in each peak were obtained in a .txt file (CellCycle\_Percentages\_table), after running R code with the required input data which in this case is the range of intensities belonging to each peak. This range was selected after analyzing each histogram, taking into account the presence of a given background level. For example, in the case of figure IV-7 (A) the range of selected G1 and G2 intensities were 40-64 and 92-120, and in the case of figure IV-7 (B) were 80-116 and 76-208, respectively. Since the typical shape of the cell cycle curve is lost over time, given the obvious (and expected) decline of EdU-negative cells, the values of more advanced time-points were chosen based on previous time-points. Selected values for all experiments are depicted in table VII-6 of annexes.

So, after obtaining the percentages of cells on G1 and G2 peaks (%G1\_peak and %G2\_peak), the number of cells was calculated (NG1 and NG2) and finally, the percentage of cell in G1 and G2-phases

were estimated (%G1\_tp and %G2\_tp) (Table VII-7 of annexes). For example, to estimate NG1 and %G1\_tp:

$$NG1 = \%G1\_peak \times (\text{Number of EdU negative cells}) \quad (3)$$

$$\%G1\_tp = \frac{NG1}{\text{Total population}} \quad (4)$$

The number of EdU negative cells (N\_EdU-) was estimated through the frequency of EdU negative cells, obtained in Main Project, part 2. The total population was estimated through the frequency of cells DAPI or Hoechst positive, obtained from the preliminary project.

The graphs containing the percentages of G1 cells in total population (%G1\_tp) vs time points and the percentages G2 cells in total population (G2 %G2\_tp) vs time-points of experiments 7, 8 and 9 are shown in Figures IV-8 (A) and IV-9 (A). The results of experiments 11 and 12 are not presented together with experiments 7, 8 and 9, since experiments 11 and 12 have two additional time-points.

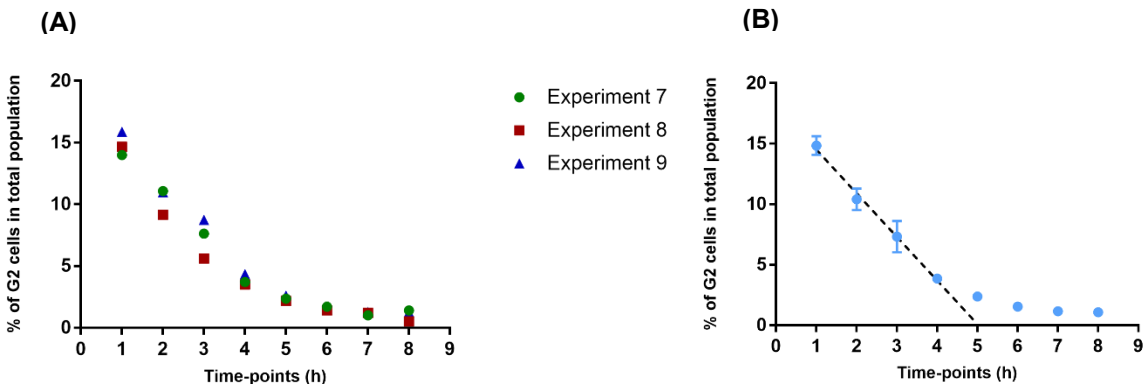


**Figure IV-8: Percentage of G2 cells in total population (%G2\_tp) along time-points (experiments 7, 8 and 9).** (A) Actual values of each experiment; (B) Average values ( $n=3$ ); The tendency line (dashed line) represents the linear decrease of the percentage G2 cells in total population until T4h; Values displayed as mean  $\pm$  standard deviation.

It is clear from the analysis of figure IV-8 (A) that, in three independent experiments, the percentage of cell in G2 in total population shows a consistent behavior over successive time-points. In all cases, a decline is seen until T4h/T5h followed by stabilization afterwards. This indicates that G2 phase lasts approximately 4-5h. These data are in agreement with our predictions and with published data on features of the cell cycle in this cell line (HCT-116)<sup>100</sup>. Figure IV-8 (B) features the average percentage of G2 cells in the total population at each time-point, and respective standard deviations. The dashed line is the tendency line, which predicts the linear decrease of the percentage of G2 cells along those time-points and emphasizes the stabilization trend that starts in time point T5h. The values of standard deviations are low meaning that the actual values do not differ much from mean values. Specially, standard deviations of time-points from T5h to T8h are almost zero, highlighting the reproducibility of this method (of note, GraphPad Prism 7.03 does not draw the error bars when error bars were shorter than the height of the symbol).

The values between experiments 7, 8 and 9 of the percentage of G1 cells in total population, over time are more divergent (Figure IV-9 (A)), presenting larger values of standard deviations (Figure IV-9 (B)). Besides that, the results of these experiments suggest that 8 time-points may not be ideal for quantifying the length of G1 plus G2, since the final stabilization expected was not observed. In addition, the tendency line represents a linear behavior until T8 (Figure IV-9 (B)). However, the remaining 5 % of EdU-negative cells at time point T8h is close to the expected percentage of G1 cells in total population in this cell line<sup>100</sup>, suggesting that additional time points although desirable may not add much information.

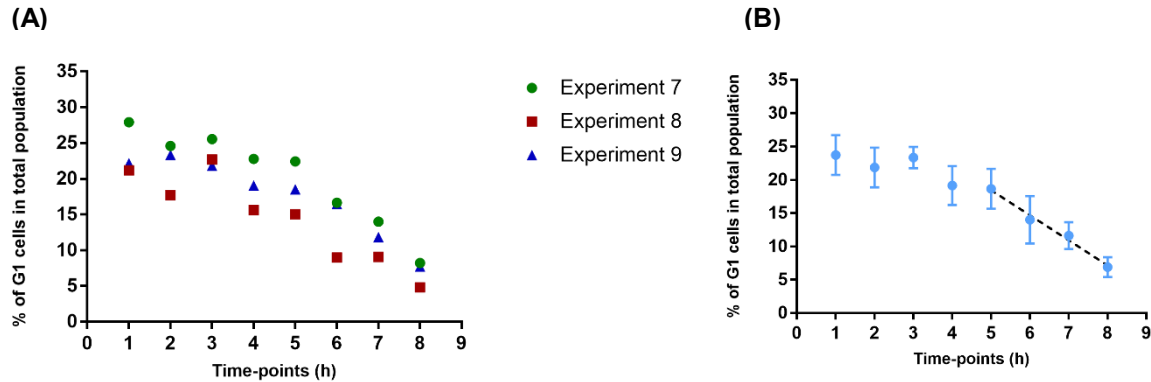


**Figure IV-9: Percentage of G1 cells in total population (%G1\_tp) vs time points (experiments 7, 8 and 9).** (A) Actual values of each experiment; (B) Average values ( $n=3$ ); The tendency line (dashed line) represents the linear decrease of the percentage of G1 cells in total population since T5h; Values displayed as mean  $\pm$  standard deviation.

Figures IV-10 (A) and (B) depict graphs of the average percentages of cells in G1 vs time points and average percentages of cells in G2 vs time points, of experiments 11 and 12, with respective standard deviations.

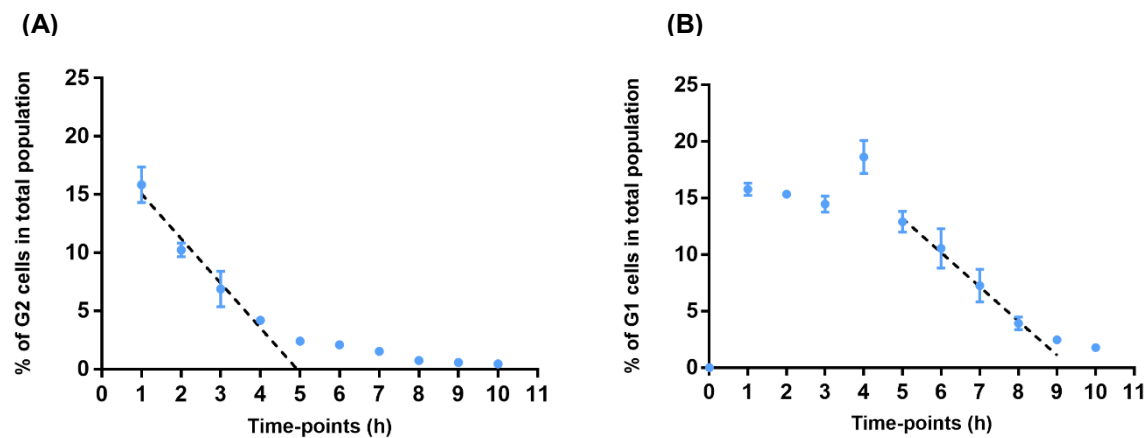


**Figure IV-10: Percentage of (A) G2 and (B) G1 cells in total population (%G2\_tp and %G1\_tp) vs time points (experiments 11 and 12;  $n=3$ ). Values displayed as mean  $\pm$  standard deviation.**

In experiments 11 and 12 we have extended the period of analysis to 10 time-points. This showed that the percentages of EdU-negative cells indeed stabilize after T9h, indicating that the sum of G1 plus G2 is approximately 9h. The duration of G1 phase was estimated by subtracting the duration of G2 phase from the total time that the G1 peak takes to vanish (~9hours in both experiments). So, the length of G1-phase is between 4 and 5 hours.

In the original research where the E-CFI method was established values of  $5.4 \pm 0.94$  h and  $3.8 \pm 0.45$  h were estimated for G1 and G2 phases, respectively, which are in close agreements with those obtained herein for the same cell line. Further experiments with 10 time-points - up until 10h of EdU incorporation - need to be performed in order to support the results of the two experiments referred above, and prove the reproducibility of this tool for quantifying not only S-phase but also G1 and G2-phases.

#### **IV.1.2.3.Influence of cell number in the estimation of S phase duration time**

Sections IV.1.2.3 and IV.1.2.4 aim to analyze if the number of identified cells influences the estimation of S, G1 and G2-phases.

Experiment 4 was used to test the influence of different sets of input images on S-phase quantification. More specifically, sets of 2, 4, 6, 9, 12 and 18 input images were analyzed using exactly the same settings as in section IV.1.2.1 (Project 1). Since the quantification of S-phase is obtained from the graphs *Maximum Integrated Intensity* vs time-points, these graphs were created for each set of input images (Figure IV-11). Of note, the connecting lines between time-points of experiments are only present to support the data analysis.

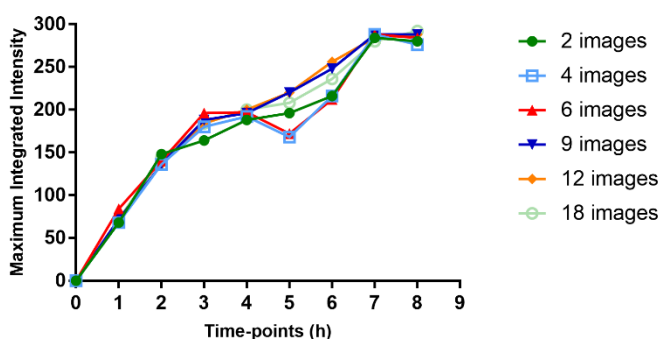


**Figure IV-11: Maximum Integrated Intensity along time-points using different sets of input images (2, 4, 6, 9, 12 and 18 images) of experiment 4.**

Looking at Figure IV-11, it is clear that the typical stabilization between T7h and T8h occurs even when the number of input images is only two. However, the values of the preceding time-points are quite divergent. As mentioned before, the maximum intensity increases over time until achieving stabilization.

When sets of 4 and 6 input images were used there was a decrease of the maximum intensity between time-points T4h and T5h. In fact, this decrease was not seen when a set of only 2 input images was used. Indeed, just the graphs corresponding to 9, 12 and 18 input images display a relatively linear increase until T6h. Although a stabilization stage (between T7h and T8h) occurred in all cases, the use of 9, 12 and 18 input images provided more consistent values (Figure IV-11). More specifically, the cells of time-point T4h incorporated EdU for one hour less than cells of time-point T5h. So, they should present lower maximum intensity values for EdU-coupled fluorescence. Since this was not verified for the cases of 2, 4 and 6 input images we conclude that this low number of input images is not sufficient to accurately estimate the length of S phase because do not correctly reflect the actual behavior of cells.

Table VII-8 and respective figure VII-1 of annexes display the number of identified cells for each set of input images along time-points. As expected, the number of identified cells increases with increasing numbers of input images. Since the minimum number of input images that originate reliable results is 9, the respective range of identified cells is between 331 (T1h) and 1954 (T8h). It is important to mention that the results from 18 or 12 input images are as reliable the results obtained with 9 input images. This means that after a minimum of identified cells is reached any further increase does not result in any substantial increase in accuracy.

In all, these findings show that the number of identified cells influences the accuracy of estimation of S phase duration time.

#### **IV.1.2.4.Influence of cell number in the estimation of G1 and G2 duration time**

Herein, the influence of the number of identified cells on G1 and G2 quantification was tested according to project 2. Different sets of input images (2, 4, 6, 9 and 12 images) from experiment 7 were used. The settings utilized for this purpose were the same already used in section IV.1.2.2.

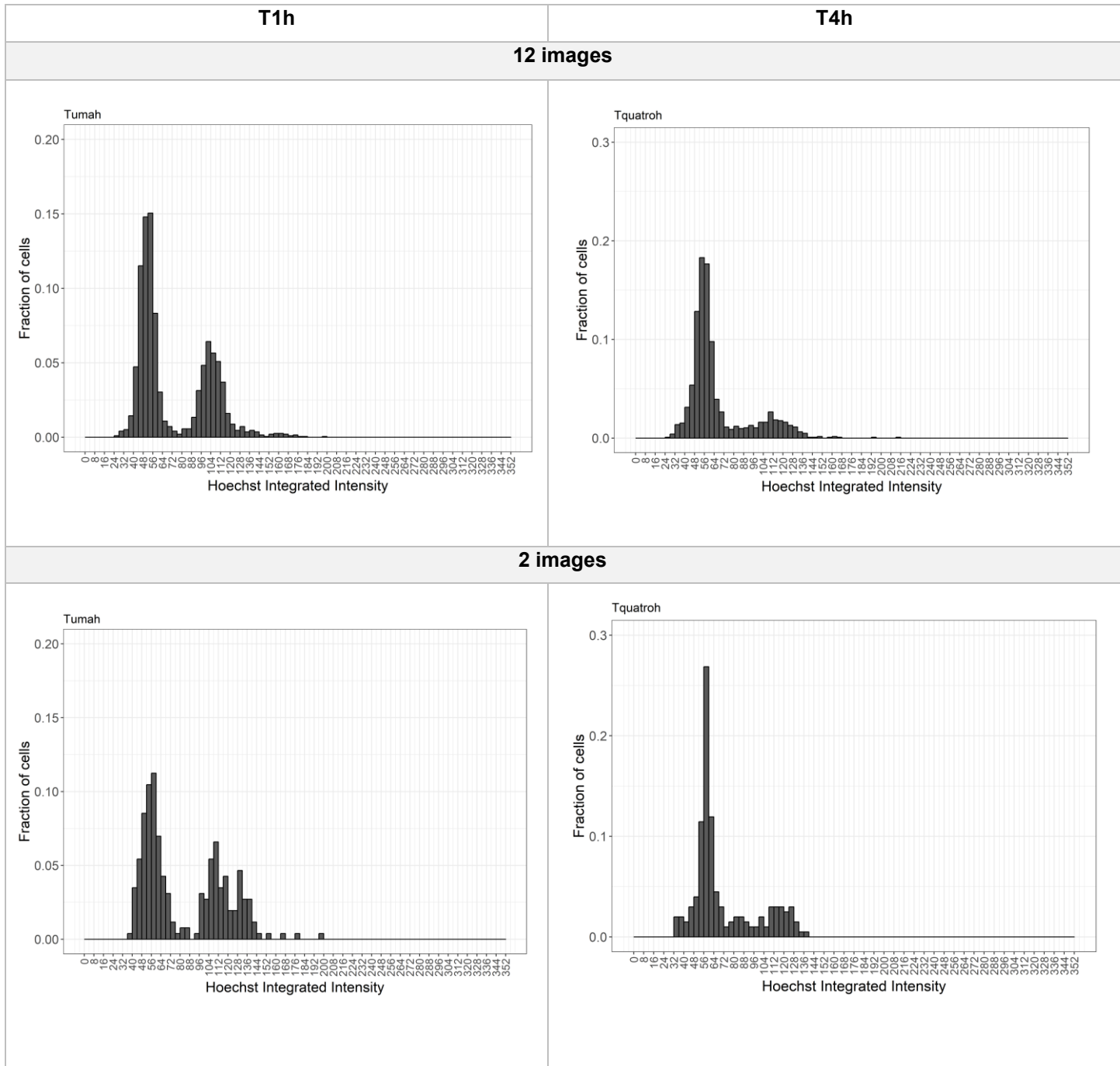
It is crucial that cell cycle curves present a defined shape, since one of the important steps during G1 and G2 quantification is the selection of the range of intensities belonging to each peak through analysis of the histograms. Also, the results of section IV.1.2.2 have shown that after a certain time-point the selection of the range of intensities has to be done in relation to previous time-points when the number of cells at a given peak (G1 or G2) is too low. So, in this chapter, time-points T1h and T4h were analyzed. T1h was chosen since its corresponding histogram is composed by the largest number of EdU-negative cells thus must ensure the correct identification of intensities attributable to G1 and G2 cells in subsequent time points. In addition, T4h was also chosen because this is the time-point at which the G2 peak practically disappears. Despite this, according to previous results from section IV.1.2.2, the histograms of this time-point still feature well defined shapes.

Table IV-3 indicates the number of EdU-negative cells identified on T1h and T4h time-points, for different numbers of input images (2, 4, 6, 9 and 12 images).

**Table IV-3: Number of cells identified on T1h and T4h for each set of input images.**

Set of input images	2	4	6	9	12
T1h	258	611	963	1404	1946
T4h	201	389	540	898	1246

**Table IV-4: Histograms (Fraction of cells vs Hoechst Integrated Intensity) of experiment 7 (T1h and T4h), for two sets of input images (12 and 2 images).**



In table IV-4 are represented the histograms of time-points T1h and T4h (experiment 7), using two sets of input images (2 and 12 input images). The histograms corresponding to the remaining sets of input images are on Table VII-9 of annexes.

It is clear that histograms obtain from only 2 input images do not feature a defined shape. Regarding histograms obtained from 4 and 6 input images (Table VII-9 of Annexes), their shape seems to be much more defined, although not as well defined as histograms obtained from 9 or 12 input images. So we cannot claim that this number of input images is enough to correctly select the range of intensities corresponding to each peak. In addition, the number of cells identified at T4h, in the cases of 4 and 6 input images, were respectively 381 and 540. This means that the histograms of subsequent time-points will comprise a smaller number of cells and thus their shape will expectedly be less well defined. Further analysis needed to be done to test this hypothesis. Finally, the histograms obtained from 9 input images were very similar with the ones obtained with 12 input images. In addition, the number of cells identified on T4h was 898, which is almost double the number of cells identified for the same time-point when 6 input images were used. In this case, looking at the histograms it seems that 9 images are enough to obtain an accurate selection of the range of intensities (in both time-points T1h and T4h) corresponding to G1 and G2 peaks. Even though in the subsequent time point the number of identified cells becomes smaller, this problem may be overcome by selecting the intensities corresponding to G1 and G2 peaks from well-defined peaks in previous time points.

These finding are in agreement with the ideas of Roukos and colleagues, which stated that the minimum number of cells needed to quantify cell stages is 500; however higher numbers of cells originate smoother and more accurate cell cycle profiles<sup>68</sup>.

To conclude, on sections IV.1.2.3 and IV.1.2.4 the influence of the number of cells on the shape of cell cycle histograms was analyzed. There must be a balance between the number of images acquired and the time spent acquiring and processing the data, since a higher number of images, giving rise to a larger number of identified cells, originate better defined cell cycle profiles but is more time consuming.

#### **IV.1.2.5. Estimation of S phase duration time using SD confocal microscopy**

The quantification of S-phase using SD confocal microscopy is relevant to prove the applicability of the E-CFI protocol using different microscopies. For this purpose, three experiments (13, 14 and 15) were performed using HCT-116 cells, EdU incorporation and detection as previously described. Project 1 was used as well to process the images obtained from SD confocal microscopy (maximum projections of z-stacks). The resolution and pixel size of widefield microscope and SD confocal microscope are different, so the typical diameter of identified cells had to be adapted. The resolution on SD is  $512 \times 512$  ( $341,33 \mu\text{m} \times 341,33 \mu\text{m}$ ), and the pixel size is approximately  $0,667 \mu\text{m}$ . In the case of the widefield microscope, the resolution is  $2252 \times 2208$  ( $624,7 \mu\text{m} \times 501,22 \mu\text{m}$ ), and the pixel size is approximately  $0,227 \mu\text{m}$ . So, with a larger pixel size a smaller number of pixels is needed in order to identify the same area. The typical range of nuclear diameters chosen was 10-25 pixels.

After processing the data, the values of maximum EdU-coupled intensities obtained were normalized for a maximum value of 300 in order to achieve better comparison between experiments. The mean values of *Maximum Integrated Intensity* were estimated as well as the correspondent standard deviations (figure IV-12).

It is noticeable that a similar tendency for stabilization is present. When comparing these data with results of section IV.1.2.1, the smaller range of maximum integrated intensities along time-points is also obvious. For example, time-point T1h showed values between 180 and 200, while in section IV.1.2.1 the range of *Maximum Integrated Intensity* values for the same time-point, was between 50 and 75. However, this just affects the initial time-points but not the stabilization at 6-7h of EdU incorporation, again consistent with a duration of S phase of 6-7h.

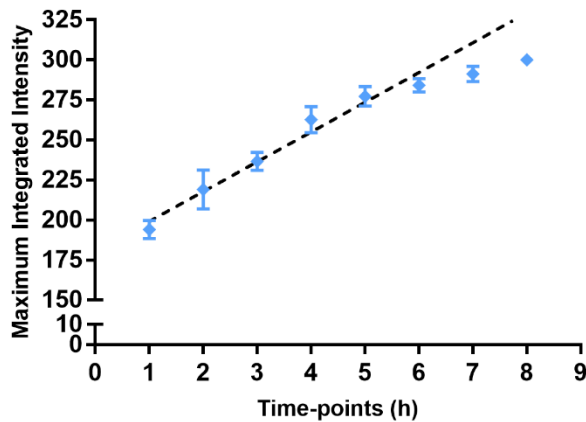
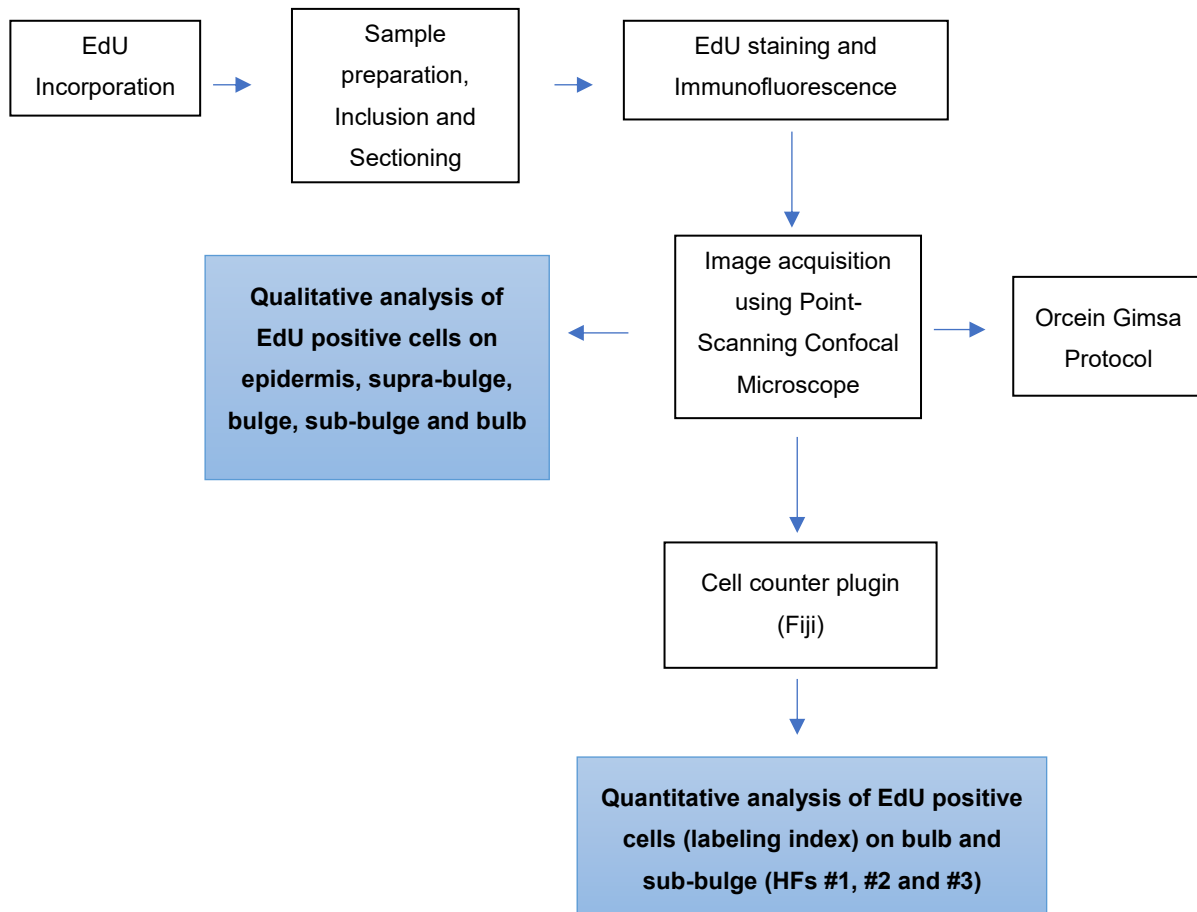


**Figure IV-12: Maximum Integrated Intensities along time-points and respective standard deviations (Experiments 13, 14 and 15; n=3). The tendency line (dashed blue line) represents the linear increase of maximum Integrated Intensity until T6h. Orange values highlight the stabilization trend. Values displayed as mean ± standard deviation**

The values increase linearly until time-point T6h, although in a smoother way than when using widefield microscopy. Time-point T7h is already significantly below the tendency line (dashed line), meaning that stabilization had already begun. These results corroborate the ones obtained on section IV.1.2.1, using widefield microscopy, indicating that the tool developed in this master thesis for cell cycle quantification can be adapted for different microscopies. However further experiments need to be done, not only to increase the number of experiments for S-phase quantification, in order to obtain more robust results, but also quantify G1 and G2-phases using this microscopy.

## IV.2. Hair follicles characterization using EdU

### IV.2.1. Outline



### IV.2.2. Qualitative analysis

Human hair follicles are in constant cycle, so besides developing a tool for cell cycle quantification using cultured cells, this master thesis aims to establish methodologies for characterizing human HF maintenance and proliferation *in vitro*, not only qualitatively but also in a quantitative manner (labeling index - LI). These tools can bring significant insights regarding hair follicle dynamics and their specific cell populations, namely HFSCs.

For this purpose, two scalp biopsies were allowed to incorporate EdU for different periods of time - experiment 1 (transplantation biopsy): 12h; experiment 2 (punch biopsy) 4h - in order to analyze the proliferation capacity in four different HF regions namely bulb, sub-bulge (between bulb and bulge), bulge and supra-bulge (between bulge and epidermis) (figure IV-13).

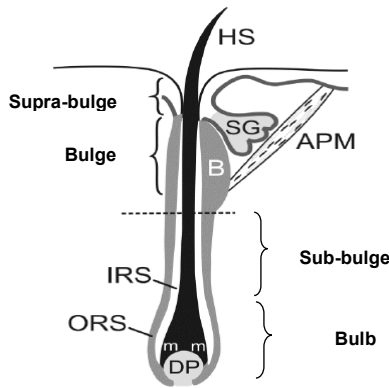
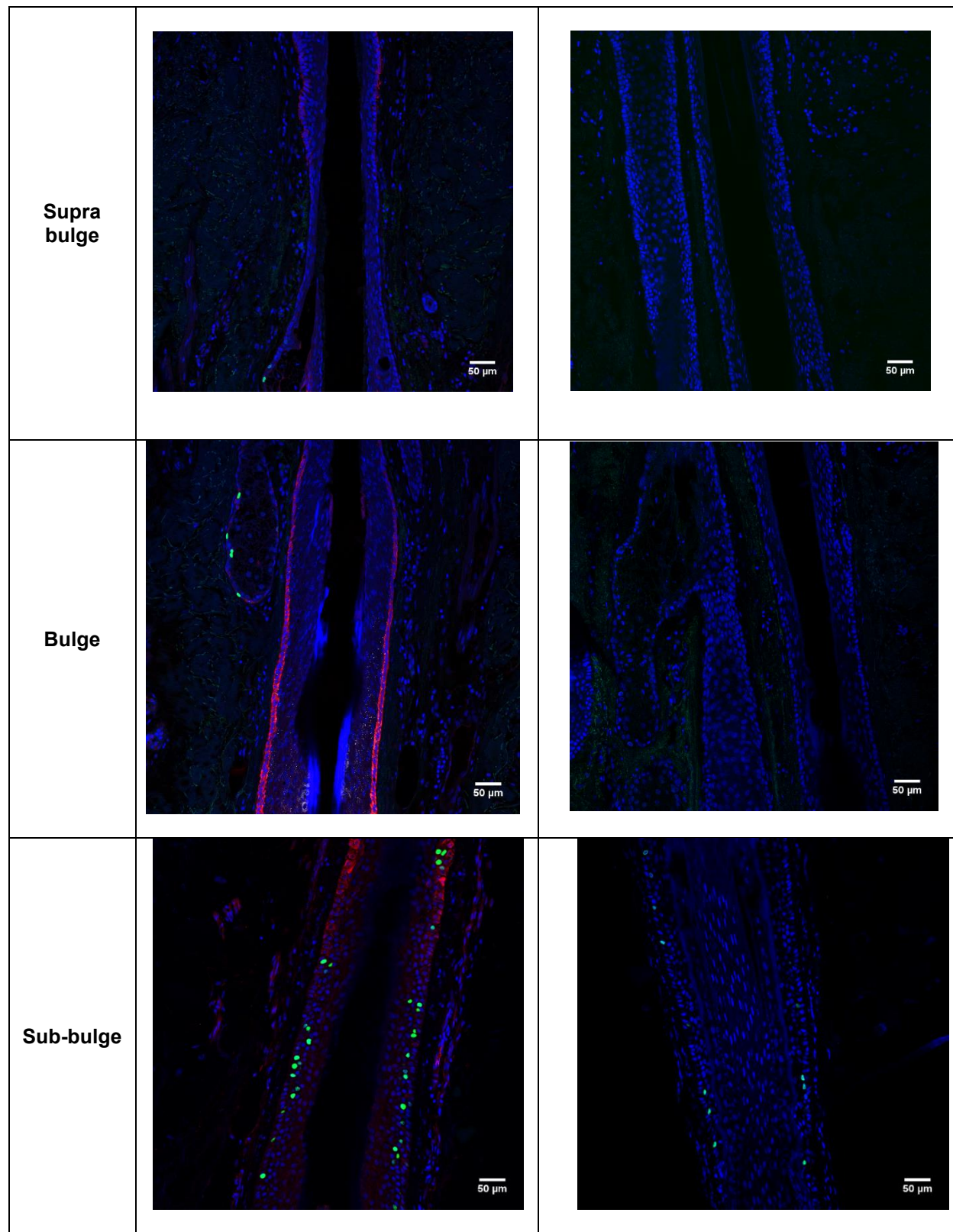


**Figure IV-13: Hair follicle regions<sup>43</sup>.** (APM: arrector pili muscle; DP: dermal papilla; m: matrix; HS: hair shaft, IRS: inner root sheath; ORS: outer root sheath; SG: sebaceous gland).

Table IV-5 contains images of different HF regions obtained through multichannel acquisition using the Confocal Microscope Zeiss LSM 710. Left column contains representative HF images from experiment 1, with merged channels where all nuclei were identified by blue fluorescence (DAPI staining), replicating DNA by green fluorescence (EdU staining) and bulge cells by red fluorescence (CK-15 staining). Right column depicts representative HF images from experiment 2, with merged channels where all nuclei were identified by blue fluorescence and replicating DNA by green fluorescence. CK-15 was used to assist the identification of bulge region. After image acquisition some of the immunolabeled HF sections were stained with Giemsa, in order to aid in the identification of HF regions during image analysis. So, CK-15 was not used to stain all HF sections. Bulge region was identified not only because of its location within the whole structure but also because of its proximity to sebaceous glands, whose shape was easily recognized in most of the bulge images, and to arrector pili, which was also recognized in some images.

**Table IV-5: Representative HF images of experiment 1 and 2 (columns) with merged channels, where blue fluorescence represent all nuclei (DAPI staining), green fluorescence represents replicating DNA (EdU staining) and red fluorescence represents bulge cells (CK-15 staining). Rows represent different anatomical regions (epidermis, supra-bulge, bulge, sub-bulge and bulb). Images were acquired in Confocal Microscope Zeiss LSM 710. Scale: 50μm.**

	Experiment 1 (Hair follicle #1)	Experiment 2 (Hair follicle #3)
Supra bulge and epidermis		



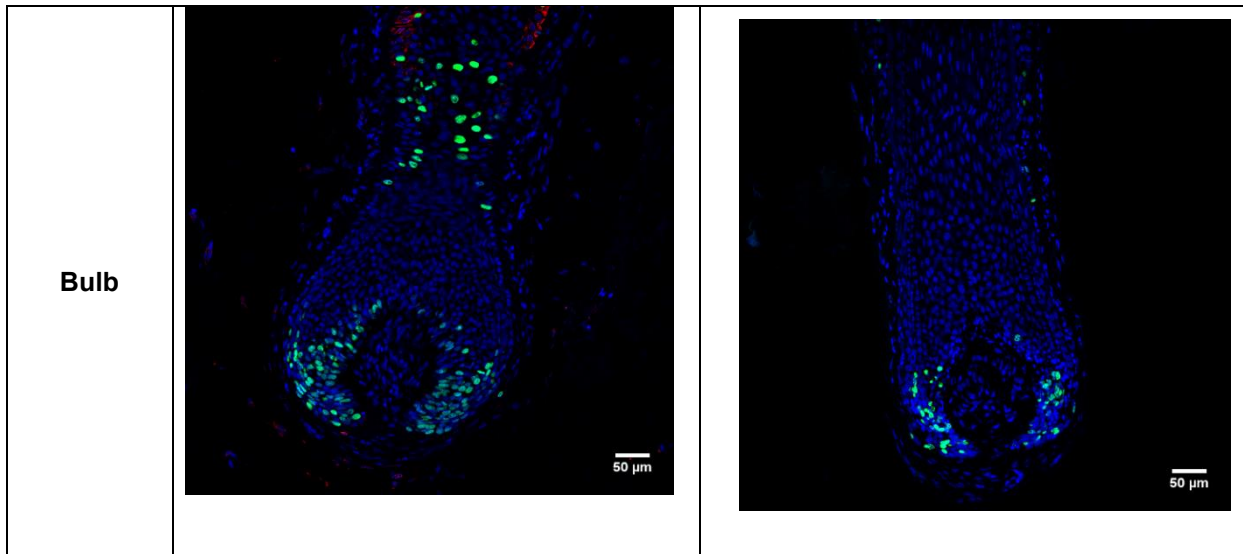
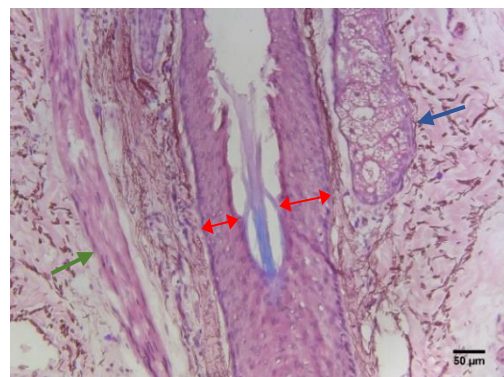


Figure IV-14 depicts an HF section comprising the bulge regions and stained with Gimsa. In this image we can easily identify the sebaceous gland (blue arrow) and the arrector pili muscle (green arrow), as well as bulge ORS (red arrows). Further images of epidermis and bulb regions stained with Gimsa are presented in annexes (Figure VII-3)



**Figure IV-14: Image of bulge region stained with Gimsa and acquired using the brightfield microscope Leica DM2500. Blue arrow represents the sebaceous gland, green arrow represents the arrector pili muscle and red arrows represent bulge ORS. Scale: 50μm.**

Before characterizing the dynamics of cell proliferation within HFs it is essential to classify the HFs with respect to their stage within the hair cycle. Distinguishing HFs in anagen from HFs in early catagen is not easy due to their anatomical similarities. A guide to studying human hair follicle cycling developed by Oh and colleagues in 2016 addressed this issue by establishing the key features of human hair follicles during each hair follicle stage. Namely, the “onion” shape of the bulb on anagen VI and the presence of melanin on dermal papilla on early catagen are two useful characteristics for distinguishing these two hair follicle stages<sup>83</sup>. For instance, hair follicle of experiment 1 (table IV-5) presents a bulb with a “onion” shape. However, we had some doubts regarding hair follicle of experiment 2 (table IV-5), due to its smaller matrix volume, in comparison with HF of experiment 1. After analyzing several contiguous sections of this hair follicle, using a brightfield microscope, we observed that the melanin was distributed around dermal papilla, and not inside it, as described in the guide for hair follicles in

anagen VI. So, both hair follicles represented on table IV-5 were considered as in anagen VI of hair cycle.

After performing a broad analysis of hair follicle images, it was clear that bulb and sub-bulge were the regions which presented the most significant distribution of proliferative cells. In supra-bulge region and epidermis EdU-positive cells were less frequent. In contrast, in bulge region EdU-positive cells were almost absent. It was also observed that, regarding experiments 1 and 2, HFs which incorporated EdU for a longer time presented significantly more EdU positive cells, as expected.

The observations regarding the bulb and bulge are in agreement with what was expected for anagen VI HFs, since the cycling part of hair follicle, (mainly the bulb region) is the one known to present the larger frequency of proliferative cells<sup>105</sup>. As mentioned before, during anagen, transit amplifying cells with origin in HFSCs colonize the matrix, proliferate and give rise to the inner root sheath and the hair shaft<sup>41</sup>. Furthermore, some researchers observed (in mouse models) that ORS progenitors are not the same as IRS and hair shaft progenitors. They describe that ORS progenitors are dispersed along ORS, instead of localized on a niche, promoting a regional growth<sup>48</sup>. Thus, since the ORS is an inward extension of the epidermis with proliferative capacity this result was not unexpected, but we note that quantitative data obtained in human hair follicles is basically non-existent.

The sebaceous glands and epidermis also showed some EdU-positive cells. Human skin is in constant renewal and it would thus be expected that the epidermis featured a significant amount of cycling cells<sup>56</sup>. However regarding HF sections of experiment 2, EdU-positive cells in the epidermis occurred mainly on peripheric regions. This probably resulted from poor penetration of EdU when punch biopsy material (3-4 mm in diameter) was utilized in HF organ cultures, since it was not observed in cultured specimens obtained in preparation for HF transplantation (1-1.5mm diameter).

Interestingly, during image acquisition sessions we observed on experiment 2 the presence of a hair follicle in catagen. Figure VII-2 (A) of annexes shows its overall structure after staining for DNA with DAPI. This HF could be classified as in catagen according to established criteria<sup>83</sup>. Expectedly, the EdU staining pattern was not the same as those seen in HFs in anagen. Bulb and sub bulge regions were almost negative for EdU staining. A few EdU-positive cells were identified in bulge region, in contrast to anagen HFs, in which the bulge was almost fully negative for EdU incorporation. Figures VII-2 (B) and (C) (annexes) depict the bulge (red arrows that identify EdU-positive cells) and bulb regions, respectively.

It is important to mention that, in the context of this thesis work, protocols for sample preparation before cryo-sectioning were also improved. This is relevant since the HF is particularly difficult to section given the coexistence within this mini-organ of structures with highly different stiffness, namely adipose tissue and keratin-rich hair shafts. To this end HFs, either obtained by punch biopsy or isolated HFs obtained in preparation for hair transplantation, were included in acrylamide in order to create a substructure within them. This helped HFs to resist the subsequent step of exposure to a high concentration (8%, w/v) of SDS. Then they were exposed to SDS (8%, w/v) in order to retrieve antigens that might be concealed by prolonged formaldehyde fixation. As control for this procedure we just

skipped the acrylamide embedding step and proceeded directly to treatment of the specimens with SDS. These specimens showed a profound disruption of HF epithelial substructures, as well as disruption of the normal architecture of the interfollicular epidermis, thus attesting to the importance of prior acrylamide embedding. Figure VII-4 of annexes shows two such examples after staining with Orcein-Gimsa where in (A) epidermis and in B) bulb region are depicted. This strongly suggested that acrylamide provides intra and extracellular framework of polymerized acrylamide that allows HFs specimens to withstand subsequent steps. Of note, cryo-sections of intact HFs are much easier to obtain using this procedure, which also yields much less of the artifacts attributable to cryo-sectioning.

### IV.2.3. Quantitative analysis: Bulb and Sub-bulge

Subsequently we quantified EdU incorporation (Labeling Index - LI), which highlights the presence of cells in S phase or that have recently passed through S phase, in the HF regions that show the highest incorporation of EdU, namely the bulb and sub-bulge ORS regions. For instance, the bulb region was quantified below Auber's line (AL), above Auber's line, and in ORS. Three hair follicles in anagen VI were thus quantified, two from experiment 1 (hair follicle #1 and hair follicle #2) and one from experiment 2 (hair follicle #3). Hair follicles #1 and #3 correspond to those shown in table IV-5. Each HF region (bulb and sub-bulge) was quantified using sets of contiguous sagittal or parasagittal images. The number of selected images for each HF area (n) varies depending on the maximum number of sections found reliable for quantification. The overall values estimated for each HF area are the averages of the values obtained for n selected images.

The cell counter plugin available on *Fiji* was used and different types of counters (or markers) were utilized to distinguish areas within each HF region and for each channel. Table VII-10 of annexes depicts an example of a bulb section quantified using cell counter plugin, where different colors represent different counters. ORS and matrix cells above Auber's line (AL) and below Auber's line on DAPI channel were identified in light pink, light blue and pink counters respectively. In Alexa 488 channel the same areas were identified using respectively blue, red and yellow counters. The following graphs (Figures IV-15 (A), (B) and (C)) show the Labeling indexes of HFs #1, #2 and #3, quantified in each bulb area (matrix Above AL, matrix below AL and ORS). The actual values obtained are in table IV-6. Since these values correspond to the average values obtained through quantification of n images, the standard deviations were as well calculated in order to understand how much the actual values differ from the average.

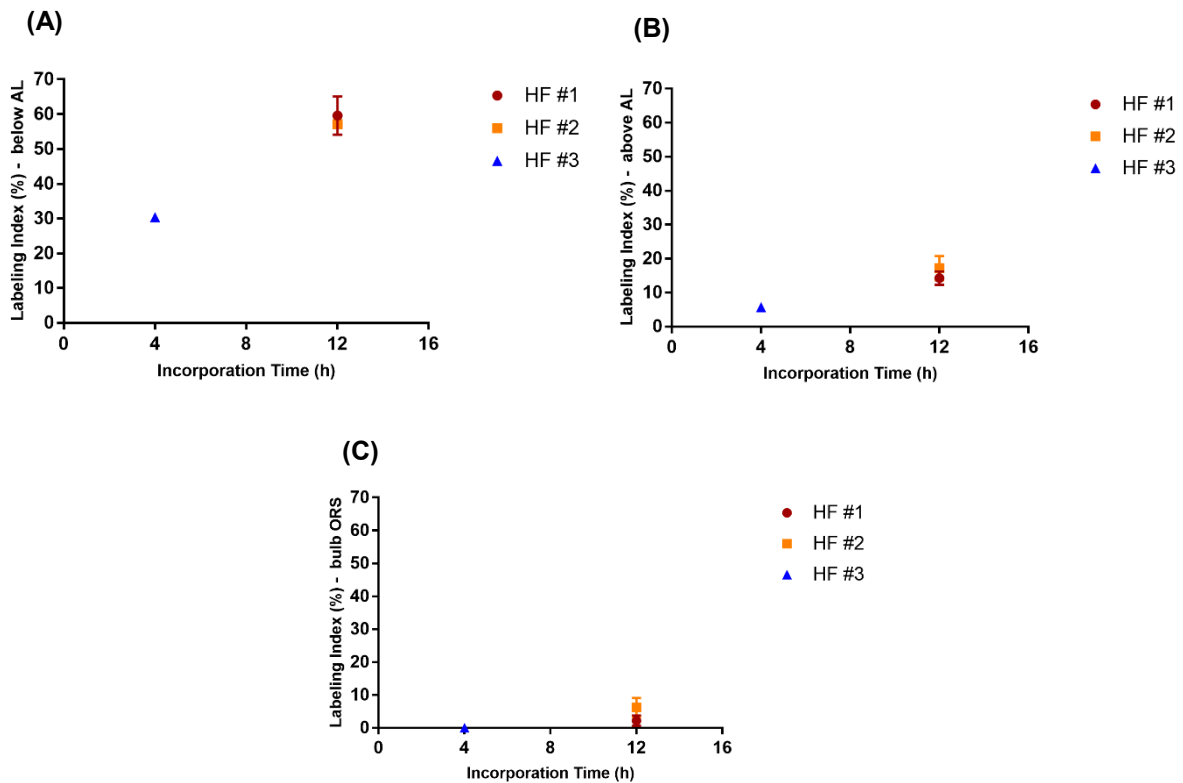


**Figure IV-15: Labeling index (%) in the hair bulb (A) below AL, (B) above AL and (C) ORS of HFs #1, #2 and #3 ( $n=5$ , 4 and 5 respectively). Values displayed as mean  $\pm$  standard deviation.**

As expected, in all areas, a higher LI was seen in HFs after 12h of EdU incorporation (hair follicles #1 and #2) when compared to a 4h incorporation time (hair follicle #3). In addition, the area below AL presented a higher percentage of EdU-positive cells than the area above AL. Finally, ORS showed the lowest values, indicating that bulb ORS has low proliferative capacity even in anagen. The values of standard deviations obtained were low. Since quantifications for the same HF were performed in contiguous sections this strongly suggests intrinsic robustness and high uniformity in cell counting procedures.

ORS sub-bulge was quantified not only through the LI but also by estimating the number of EdU-positive cells in a given ORS length (200 micrometers). For this purpose, the length of ORS quantified was measured using Fiji features. It is important to mention that each side of ORS bulge was separately quantified (part 1 and part 2 i.e. left and right sides of each optical section), since in some cases just one side was suitable for quantification due to sectioning artifacts. The minimum ORS length for quantification was approximately 180 $\mu$ m. Table VII-10 of annexes comprises an example of a sub-bulge section quantified using cell counter plugin, where different colors represent different counters. The counters used on DAPI channel were light blue (part 1) and green (part 2) and the counters used on Alexa 488 channel for identify EdU-positive cells were red (part 1) or beige (part 2).

The following graphs (Figures IV-16 (A) and (B)) feature the results of sub-bulge ORS quantifications performed on HFs #1, #2 and #3. The actual values obtained are depict in table IV-6.

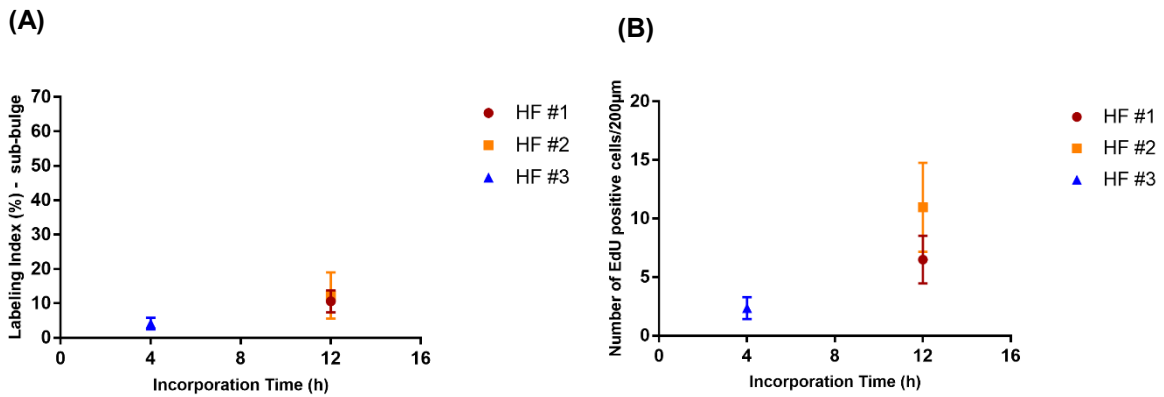


**Figure IV-16: (A) Labeling Index (%) and (B) Number of EdU positive cells in 200 micrometers of the sub-bulge ORS, of HFs #1, #2 and #3 (n=20, 4 and 18 respectively). Values displayed as mean ± standard deviation.**

Both quantifications show a similar pattern between hair follicles. As expected, in the sub-bulge we also verified that hair follicles which incorporated EdU for a longer time showed a higher number of EdU-positive cells. The standard deviations obtained here were slightly larger than the ones obtained in bulb quantification. Actually, the sub-bulge quantification was performed along all ORS. The sections near bulge region, where EdU-positive cells are less abundant, were not analyzed separately from those near the bulb. So, this slightly higher dispersion of values is not surprising. Besides that, the values obtained for HFs #1 and #2 were similar, especially in the case of the percentage of EdU-positive cells.

**Table IV-6: EdU-positive cells, LI or number, in HF regions obtained through quantification of n images.**

Bulb			
	LI below AL (%)	LI aboveAL (%)	LI in bulb ORS (%)
HF #1 (n=5)	59,6	14,3	2,2
HF #2 (n=4)	57,1	17,2	6,2
HF #3 (n=5)	30,3	5,7	0
Sub-bulge			
	LI in sub-bulge ORS (%)	Number of EdU-positive cells in 200 μm of sub-bulge ORS	
HF #1 (n=20)	10,6	6,5	
HF #2 (n=4)	12,3	11	
HF #3 (n=18)	4,1	2,4	

It is important to mention that, although some research has emerged in the last years using similar methods to study human hair follicle dynamics, most of which referred in primer for studying cell cycle dynamics of human HFs<sup>67</sup>, none presented quantitative data. The only paper found to have some quantitative data is from 1980<sup>81</sup> (mentioned before on sections I.3.2.4), and again, these data only focus on the bulb region. Also, most of the obtained data on EdU (or BrdU) labeling relates to sub-bulge regions since when using currently available methods HFs are sectioned at the adipose-dermal transition before culture (amputated HFs)<sup>105</sup>. This issue was overcome here by the use of finely trimmed HFs in preparation for HF transplantation, which proved a reliable material for culture of this mini-organ.

In sum, in this work conditions for culture and metabolic labeling (deoxy-nucleotide/EdU incorporation) of entire HFs, for improving cryo-sectioning of human HFs and for quantitation of EdU-labeled cells across different sub-regions of HFs have been established. This will predicate development of future research utilizing HFs in the recipient laboratory.

### **IV.3. Preparation of hair follicle cell suspension from human biopsies – Initial work of isolation hair follicle stem cells**

The third part of this master thesis comprises the initial work on the isolation of human HF stem cells (HFSCs), which consisted in the optimization of the protocol for preparing and culturing cell suspensions of HF epithelial cells. This is described in detail in Materials and Methods where it can be appreciated several variables that have been tested in the course of protocol optimization. Our protocols were based mainly on those described in Ohyama et al. (2006)<sup>65</sup> and Hilmi et al. (2013)<sup>88</sup>.

The protocol of preparing cell suspensions of HF epithelial cells has two main initial steps, digestion of the connective (including adipose) tissue surrounding HFs and the disruption of epithelial cells from HFs. Figure VII-5 of annexes shows two images of HFs before and after connective tissue disruption, acquired in the Phase Contrast microscope - Zeiss *Primovert*. In the last protocol tested, which is currently in use (Materials and Methods: III-3), we have used collagenase/dispase for connective tissue disruption and trypLE™ Express for disaggregation of epithelial cells from HFs. However, other alternatives have been tested, namely Dispase II (CellnTec) for connective tissue removal and Accutase (CellnTec) or trypsin (Gibco®) for epithelial cell disruption. The times and temperatures of incubation with these enzymes were tested as well. For collagenase/dispase or Dispase II we have tried several combinations such as overnight at 4°C, overnight at 37°C and 4h-5h at 37°, and it was established that overnight at 37° was the best choice. In addition, regarding trypLE™ Express or equivalent, after testing times between 20min and 3 hours it was concluded that an incubation of 20-30minutes at 37°C was enough to disrupt epithelial cells within HFs.

The way of sectioning biopsy samples in preparation for enzymatic digestions was also adjusted over time. Initially, biopsies were sectioned as much as possible into small pieces before connective tissue digestion. We realized that the mechanical force applied at this step could damage follicular structure, so now the biopsies are just cut into fragments smaller than 1 millimetre after a period of “tissue softening” of 3-4h in collagenase/dispase.

After preparing cell suspensions of HF epithelial cells different culture media were tested such as ProCHO™ 4 medium (04-919Q, Bio Whittaker®, Lonza) and William's E medium GlutaMAX™ (32551020, Gibco®). After several days of culture we observed that cells undergoing proliferation were mainly fibroblasts, not epithelial cells as aimed. By contrast, when HF cellular suspensions were cultured

in CnT-07 medium<sup>87</sup> we observed growth of individual colonies comprised of epithelial cells. Of note, these colonies are somewhat pleomorphic and, thus, further confirmation that at least some of them correspond to HFSCs needs to be obtained. In Figure IV-17 a colony formed after 9 days of culture in CnT-07 is depicted.

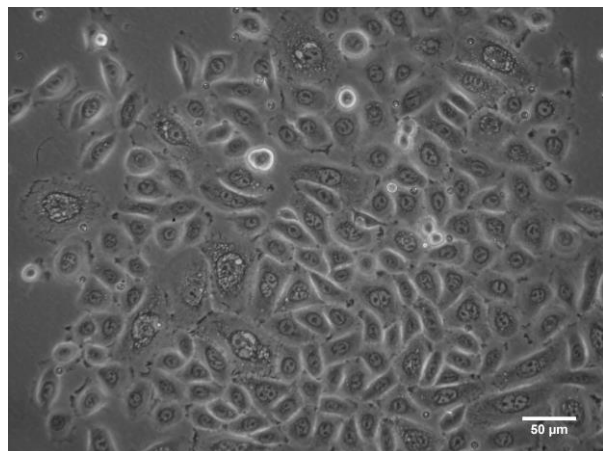


**Figure IV-17: Colony of epithelial cells formed after 9 days of culture in CnT-07 medium. Image acquired using the Phase Contrast microscope Zeiss Primovert. Scale:50µm.**

The next step of this project is to stain cultured cell with specific markers of HFSCs such as CK-15 or CD200 in order to confirm their presence before isolation. This isolation will be performed using magnetic beads, as described in Ohyama et al. (2006)<sup>65</sup>.



## V. Conclusions and Future Trends

Vitiligo is a disease whose pathophysiology remains elusive. A big challenge in this field is how to combine arresting disease progression, that is, promote the transition from active Vitiligo to stable Vitiligo, and at the same time, promote repigmentation of existing lesions. Despite all treatments that developed around the diverse proposed pathophysiologic mechanisms none proved effective<sup>3</sup>. Researchers have developed treatments based on HFSCs, in which cell suspensions are transplanted into Vitiligo lesions (Cellular Grafting). Although results are promising it is felt that much still needs to be done<sup>89</sup>. This master thesis aims to contribute to fill in this gap through developing tools for study human HF biology.

We successfully develop a tool for cell cycle quantification using E-CFI applied to microscopy, which can be used to study any cell population and tissue sections, including sections of HFs. We estimated a duration for S-phase of 6/7h, for G1-phase of 4/h5 and for G2-phase of 4/5h in HCT-116 cells. These values are very similar to the results reported by Pereira and colleagues using E-CFI and flow cytometry. They obtained  $6.8 \pm 0.35$  h,  $5.4 \pm 0.94$  h and  $3.8 \pm 0.45$  for S, G1 and G2-phase respectively<sup>100</sup>.

When the influence of number of cells on S, G1 and G2 estimations was analyzed, it was concluded that the number do influence these quantifications. It was observed that the minimum number of images needed to obtain an accurate estimation of cell cycle phases is 9. In addition, the results obtained using SD confocal microscopy suggested that this tool can be adapted for different microscopies.

The software *CellProfiler* was used to identify cells and measure their correspondent fluorescence intensities. It is important to mention that when the settings of *CellProfiler* software were adjusted they were optimized to perform the most accurate identification of cells. However, these settings are not perfect for all images, resulting in a variable proportion of objects being wrongly identified or not identified at all. Consequently, across all experiments there is an associated error when using this identification procedure. Since the results obtained are reliable and extremely similar to those recently reported for the same cell line, we can conclude that the error is acceptable and correctly minimized. We further note that the precision of the data increases by using incremental periods of EdU incorporation that are smaller than the 1h increments used here. This can be done in the future at the expense of a more time-consuming procedure for data analysis. Thus, there should be a balance between the degree of precision chosen (dictated by the established incremental periods) and the time spent processing the data.

Furthermore, using microscopy and user-friendly softwares, we were able to develop a simple and relatively fast tool that can be applied to cell cycle quantification of any cell population or tissue sections. In the future we can use this tool to quantify cell cycle of human HF cells, which would be extremely interesting towards a better understanding of human HFs and HFSCs dynamics.

In the second part of this master thesis human HFs were characterized with respect to their proliferation in vitro (using EdU), through analysing three hair follicles. HFs #1 and #2 incorporated EdU

for 12h, while HF #3 incorporated for 4h. They were individually quantified, even #1 and #2 which belong to the same biopsy. Indeed, HFs correspond to autonomous entities (“mini-organs”) with independent cycling from each other, even when belonging to the same individual<sup>105</sup>.

HFs undergo considerable alterations when they move through the distinct stages of their life cycle (anagen, catagen, telogen). These alterations refer not only to structure but also to immunology, extracellular matrix remodelling, and stem cells biology, among others. There is some doubt with respect to whether what is observed *in vitro* matches what really happens *in vivo* since signalling between HF and surrounding tissues is lost. Besides that, HFs are considered a unique model in biology whose biomedical potential needs to be explored. For example, HFs provide the most clear example of spatial separation between SCs, which reside in the bulge (ORS) region, and the corresponding transit amplifying cells, which concentrate in the HF bulb. So, studying HFs *in vitro* can bring significant insights into several fields of research<sup>105</sup>.

We qualitatively analyzed the proliferative capacity (i.e., ongoing S phase) of cells in skin sections containing epidermis and HFs regions such as matrix of bulb, sub-bulge ORS, bulge ORS (the stem cells niche) and supra-bulge ORS. In addition, we quantified EdU positive cells (labeling index) in specific areas of bulb and sub-bulge such as bulb below and above Auber’s line (AL), bulb ORS and sub-bulge ORS.

During qualitative analysis we observed that bulb matrix and sub-bulge ORS are the regions where EdU-positive cells concentrate. As expected, we verified a higher LI in HFs which incorporated EdU for 12h than in the one which incorporated EdU for only 4 hours. Also, regarding hair bulb, it was observed that the area below AL shows the larger LI (at least 3 times higher than the area above AL). The labeling indexes obtained below AL of HFs #1 and #2 were between 57% and 60%, and approximately 30% in HF #3. Meanwhile, the labeling indexes above AL of HFs #1 and #2 were between 14% and 18% and approximately 6% in HF #3. We also observed that sub-bulge ORS presented higher values for cells that transversed S-phase (EdU-positive cells) than bulge ORS. Our results are in agreement with the described patterns of cellular proliferation in HFs (in human HFs only data for bulb is available), except for epidermis. A low percentage of EdU-positive cells were seen in the epidermis probably due to a poorly penetration of EdU into biopsy specimens (experiment 2). This was, however, circumvented by the use of HFs isolated in preparation for hair transplantation which have smaller amounts of connective tissue surrounding HFs.

ORS has a different source of progenitors from IRS and hair shaft, and the direction of movement of their keratinocytes during and after proliferation is not fully understood. In addition, it is known that ORS is a prominent source of cytokines and growth factors whose role is essential during hair cycle, namely in hair shaft production<sup>67;106</sup>. So there is a need of better understanding the dynamics of ORS and this master thesis aims to contribute to this field by presenting a robust method for studying HF dynamics. In the future the methodologies implemented here for HF culture and deoxy-nucleotide incorporation *ex-vivo*, and for cell cycle analysis using microscopy can be applied to address these issues. These methodologies may also be applied to the study of the action of drugs on HFs viability<sup>83</sup>. Ultimately,

these methods shall be useful to address factors and conditions that influence the proliferation of HFSCs, with relevance in Vitiligo.

The third part of this thesis corresponds to the initial steps towards isolation of HF stem cells. After a process of optimization, we obtained cultures of HF epithelial cells that grow robustly using Cnt-07 medium. These cells are in the process of expansion before checking for the presence of cytokeratin 15 (CK-15) and the cell surface antigen CD200, both markers of bulge HFSCs<sup>64;65</sup>.

In conclusion, the tools developed during this master thesis research will be useful for studying the dynamics of cell populations within human HFs including HFSCs, generating relevant knowledge to be subsequently applied to the study of disorders such as Vitiligo.



# VI. References

1. Alikhan, A., Felsten, L. M., Daly, M. & Petronic-Rosic, V. Vitiligo: A comprehensive overview: Part I. Introduction, epidemiology, quality of life, diagnosis, differential diagnosis, associations, histopathology, etiology, and work-up. *J. Am. Acad. Dermatol.* **65**, 473–491 (2011).
2. Manuscript, A. Revised classification/ nomenclature of vitiligo and related issues: the Vitiligo Global Issues Consensus Conference. **25**, 1–28 (2013).
3. khaled Ezzedine, Viktoria Eleftheriadou, Maxine Whitton, N. van G. Vitiligo. *Lancet* 74–84 (2015).
4. Kim, H. Y. & Kang, K. Y. Epidermal grafts for treatment of stable and progressive vitiligo. *J. Am. Acad. Dermatol.* **40**, 412–217 (1999).
5. Mohammed, G. F., Gomaa, A. H. & Al-Dhubaibi, M. S. Highlights in pathogenesis of vitiligo. *World J. Clin. Cases* **3**, 221 (2015).
6. Hann, S. K., Park, Y. K., Lee, K. G., Choi, E. H. & Im, S. Epidermal changes in active vitiligo . *J. Dermatol.* **19**, 217–222 (1992).
7. Tortora, G. J. & Derrickson, B. Chapter 17: The lymphatic system and immunity. in *Introduction to the human body. The essentials of anatomy and physiology*. 445–446 (wiley john & sons, 2010).
8. Le Poole, I. C., van den Wijngaard, R. M., Westerhof, W. & Das, P. K. Presence of T cells and macrophages in inflammatory vitiligo skin parallels melanocyte disappearance. *Am. J. Pathol.* **148**, 1219–28 (1996).
9. Cui, J., Arita, Y. & Bystryn, J.-C. Characterization of Vitiligo Antigens. *Pigment Cell Melanoma Res.* **8**, 53–59 (1995).
10. Hull, S. C., Glanz, K., Steffen, A. & Wilfond, B. S. Recruitment approaches for family studies: Attitudes of index patients and their relatives. *IRB Ethics Hum. Res.* **26**, 12–18 (2004).
11. Nath, S. K., Majumder, P. P. & Nordlund, J. J. Genetic Epidemiology of Vitiligo: Multilocus Recessivity Crossvalidated. *Am. Soc. Hum. Genet.* 981–90 (1994).
12. Alkhateeb, A., Fain, P. R., Thody, A., Bennett, D. C. & Spritz, R. a. Epidemiology of vitiligo and associated autoimmune diseases in Caucasian probands and their families. *Pigment cell Res.* **16**, 208–214 (2003).
13. Jin, Y., Birlea, S. A. & Fain, P. R. Variant of TYR and Autoimmunity Susceptibility Loci in Generalized Vitiligo. *N. Engl. J. Med.* 1686–97 (2010).
14. Morrone, A. *et al.* Catecholamines and vitiligo. *Pigment Cell Melanoma Res.* **5**, 65–69 (1992).
15. Al'Abadie, M. S. K., Senior, H. J., Bleehen, S. S. & Gawkrodger, D. J. Neuropeptide and neuronal

- marker studies in vitiligo. *Br. J. Dermatol.* **131**, 160–165 (1994).
16. Lazarova, R., Hristakieva, E., Lazarov, N. & Shani, J. Vitiligo-related neuropeptides in nerve fibers of the skin. *J. Metab. Dis.* **108**, 262–267 (2000).
  17. Lee, A. Y., Kim, N. H., Choi, W. I. & Youm, Y. H. Less keratinocyte-derived factors related to more keratinocyte apoptosis in depigmented than normally pigmented suction-blistered epidermis may cause passive melanocyte death in vitiligo. *J. Invest. Dermatol.* **124**, 976–983 (2005).
  18. Taieb, A. *et al.* Guidelines for the management of vitiligo: The European Dermatology Forum consensus. *Br. J. Dermatol.* **168**, 5–19 (2013).
  19. Barnes, P. J. How corticosteroids control inflammation: Quintiles Prize Lecture 2005. *Br. J. Pharmacol.* **148**, 245–254 (2006).
  20. Dinarello, C. A. Anti-inflammatory Agents : Present and Future. *Cell* **140**, 935–950 (2013).
  21. Williams, C. R. & Gooch, J. L. Calcineurin inhibitors and immunosuppression – a tale of two isoforms. *Expert Rev. Mol. Med.* **14**, 1–10 (2012).
  22. Köse, O., Arca, E. & Kurumlu, Z. Mometasone cream versus pimecrolimus cream for the treatment of childhood localized vitiligo. *J. Dermatolog. Treat.* **21**, 133–9 (2010).
  23. Felsten, L. M., Alikhan, A. & Petronic-Rosic, V. Vitiligo: A comprehensive overview: Part II: Treatment options and approach to treatment. *J. Am. Acad. Dermatol.* **65**, 493–514 (2011).
  24. Carlie, G., Ntusi, N. B. A., Hulley, P. A. & Kidson, S. H. KUVA (khellin plus ultraviolet A) stimulates proliferation and melanogenesis in normal human melanocytes and melanoma cells in vitro. *Br. J. Dermatol.* **149**, 707–717 (2003).
  25. Alberts, B., Johnson, A. & Lewis, J. Extracellular Control of Cell Division, Cell Growth, and Apoptosis. in *Molecular Biology of the Cell* (Garland Science, 2002).
  26. Wu, C. S. *et al.* Effects of psoralen plus ultraviolet A irradiation on cultured epidermal cells in vitro and patients with vitiligo in vivo. *Br. J. Dermatol.* **156**, 122–129 (2007).
  27. Valkova, S., Trashlieva, M. & Christova, P. Treatment of vitiligo with local khellin and UVA: Comparison with systemic PUVA. *Clin. Exp. Dermatol.* **29**, 180–184 (2004).
  28. Buckley, D. A. & Rogers, S. Multiple keratoses and squamous carcinoma after PUVA treatment of vitiligo. *Clin. Exp. Dermatol.* **21**, 43–45 (1996).
  29. Xiao, B.-H., Wu, Y., Sun, Y., Chen, H.-D. & Gao, X.-H. Treatment of vitiligo with NB-UVB: A systematic review. *J. Dermatolog. Treat.* **26**, 340–346 (2015).
  30. Yones, S. S., Palmer, R. A., Garibaldinos, T. M. & Hawk, J. L. M. Randomized Double-blind Trial of Treatment of Vitiligo. *Arch. Dermatology* **143**, 578–584 (2007).
  31. Hadi, S. *et al.* Treatment of vitiligo using the 308-nm excimer laser. *Photomed. Laser Surg.* **24**,

- 354–357 (2006).
32. Radakovic-Fijan, S., Fürnsinn-Friedl, A. M., Höngsmann, H. & Tanew, A. Oral dexamethasone pulse treatment for vitiligo. *J. Am. Acad. Dermatol.* **44**, 814–817 (2001).
  33. Njoo, M., Westerhof, W., Bos, J. & Bossuyt, M. A Systematic review of autologous transplantation methods in vitiligo. *Arch. Dermatology* **134**, 1543–1549 (1998).
  34. Wong, D. J. & Chang, H. Y. StemBook: Skin tissue engineering. (2009). Available at: <http://www.stembook.org/node/582.html>. (Accessed: 3rd May 2017)
  35. Bensouilah, J. & Buck, P. Chapter I: Skin structure and function. in *Aromadermatology: Aromatherapy in the Treatment and Care of Common Skin Conditions*. 1–11 (Radcliffe Publishing, 2001).
  36. Weller, R., Hunter, J., Savin, J. & Dahl, M. Chapter 2: The function and structure of the skin. in *Clinical Dermatology* 10–33 (Blackwell Publishing, 2008).
  37. Tortora, G. J. & Derrickson, B. Chapter 5: The integumentary system. in *Introduction to the human body. The essentials of anatomy and physiology*. 100–117 (wiley john & sons, 2010).
  38. McGrath, J. A., Uitto, J. & Pope, F. M. Chapter 3: Anatomy and Organization of Human Skin. in *Rook's Textbook of Dermatology* 1–53 (Wiley-Blackwell, 2004). doi:10.1002/9781444317633.ch3
  39. Agrawal, C. M., Ong, J. L., Appleford, M. R. & Mani, G. Chapter 2: Basic properties of materials. in *Introduction to Biomaterials. Basic Theory with Engineering Applications*. 19–46 (Cambridge University Press, 2014).
  40. Ines Brajac, M. V. D. P. M. K. Human Hair Follicle: An Update on Biology and Perspectives in Hair Growth Disorders Treatment. *Hair Ther. Transplant.* **4**, 4–9 (2014).
  41. Schneider, M. R., Schmidt-Ullrich, R. & Paus, R. The Hair Follicle as a Dynamic Miniorgan. *Curr. Biol.* **19**, R132–R142 (2009).
  42. Ross, M. H. & Pawlina, W. Chapter 15: Integumentary System. in *Histology: a Text and Atlas with correlated Cell and Molecular Biology* 488–512 (Lippincott Williams & Wilkins, 2010).
  43. Rishikaysh, P. et al. Signaling involved in hair follicle morphogenesis and development. *Int. J. Mol. Sci.* **15**, 1647–1670 (2014).
  44. Balañá, M. E., Charreau, H. E. & Leirós, G. J. Epidermal stem cells and skin tissue engineering in hair follicle regeneration. *World J. Stem Cells* **7**, 711–727 (2015).
  45. Cotsarelis, G. & Millar, S. E. Towards a molecular understanding of hair loss and its treatment. *Trends Mol Med* **7**, 293–301 (2001).
  46. Fuchs, E., Merrill, B. J., Jamora, C. & Dasgupta, R. At the Roots of a Never-Ending Cycle. *Dev.*

- Cell* **1**, 13–25 (2001).
47. Krause, K. & Foitzik, K. Biology of the Hair Follicle: The Basics. *Semin. Cutan. Med. Surg.* **25**, 2–10 (2006).
  48. Legué, E. & Nicolas, J.-F. Hair follicle renewal: organization of stem cells in the matrix and the role of stereotyped lineages and behaviors. *Development* **132**, 4143–4154 (2005).
  49. NIH Stem Cell Information Home Page. Chapter 1: The Stem Cell. *Stem Cells: Scientific Progress and Future Research Directions*. (2001). Available at: <https://stemcells.nih.gov/info/2001report/chapter1.htm>.
  50. Kumar, A., Mohanty, S., Gupta, S. & Sm, P. Stem Cells of the Hair Follicular Tissue : Application in Cell Based Therapy for Vitiligo. *Hair Ther. Transplant.* **5**, 1–5 (2015).
  51. Alonso, L. & Fuchs, E. Stem cells of the skin epithelium. *PNAS* **100**, 11830–11835 (2003).
  52. Cotsarelis, G., Sun, T. T. & Lavker, R. M. Label-retaining cells reside in the bulge area of pilosebaceous unit: Implications for follicular stem cells, hair cycle, and skin carcinogenesis. *Cell* **61**, 1329–1337 (1990).
  53. Beaver, C. M., Ahmed, A. & Masters, J. R. Clonogenicity: Holoclones and meroclones contain stem cells. *PLoS One* **9**, (2014).
  54. Rochat, a, Kobayashi, K. & Barrandon, Y. Location of stem cells of human hair follicles by clonal analysis. *Cell* **76**, 1063–73 (1994).
  55. Tiede, S. *et al.* Hair follicle stem cells: Walking the maze. *Eur. J. Cell Biol.* **86**, 355–376 (2007).
  56. Blanpain, C. & Fuchs, E. Epidermal stem cells of the skin. *Annu. Rev. Cell Dev. Biol.* **22**, 339–73 (2006).
  57. NIH Stem Cell Information Home Page. Chapter 4: The Adult Stem Cell. *Stem Cells: Scientific Progress and Future Research Directions*. (2001). Available at: <https://stemcells.nih.gov/info/2001report/chapter4.htm>.
  58. Cotsarelis, G. Epithelial stem cells: a folliculocentric view. *J. Invest. Dermatol.* **126**, 1459–1468 (2006).
  59. Ito, M. *et al.* Stem cells in the hair follicle bulge contribute to wound repair but not to homeostasis of the epidermis. *Nature* **437**, 1351–1354 (2005).
  60. Reuter, K. & Niemann, C. The Sebaceous Gland Stem Cell Niche. in *Tissue-Specific Stem Cell Niche* 27–43 (2015).
  61. Mull, A. N., Zolekar, A. & Wang, Y. Understanding Melanocyte Stem Cells for Disease Modeling and Regenerative Medicine Applications. 30458–30469 (2015). doi:10.3390/ijms161226207
  62. Nishimura, E. K. Melanocyte Stem Cells: a melanocyte reservoir in hair follicles for hair and skin

pigmentation. *Pigment Cell Melanoma* 401–410 (2011).

63. Narisawa, Y., Hashimoto, K. & Kohda, H. Immunohistochemical demonstration of keratin 19 expression in isolated human hair follicles. *J. Invest. Dermatol.* **103**, 191–195 (1994).
64. Lyle, S. *et al.* The C8/144B monoclonal antibody recognizes cytokeratin 15 and defines the location of human hair follicle stem cells. *J. Cell Sci.* **111**, 3179–3188 (1998).
65. Ohyama, M. *et al.* Characterization and isolation of stem cell– enriched human hair follicle bulge cells . **116**, (2006).
66. Xu, X., Lyle, S., Liu, Y., Solky, B. & Cotsarelis, G. Differential expression of cyclin D1 in the human hair follicle. *Am. J. Pathol.* **163**, 969–978 (2003).
67. Purba, T. S. *et al.* A primer for studying cell cycle dynamics of the human hair follicle. *Exp. Dermatol.* **25**, 663–668 (2016).
68. Roukos, V., Pegoraro, G., Voss, T. C. & Misteli, T. Cell cycle staging of individual cells by fluorescence microscopy. *Nat. Protoc.* **10**, 334–348 (2015).
69. Cooper, G. M. The Eukaryotic Cell Cycle. in *The Cell: A Molecular Approach* (2000).
70. Darzynkiewicz, Z. & Huang, X. Analysis of cellular DNA content by flow cytometry. *Curr. Protoc. Immunol.* **5**, 5–7 (2004).
71. Salic, A. & Mitchison, T. J. A chemical method for fast and sensitive detection of DNA synthesis in vivo. *Proc. Natl. Acad. Sci. U. S. A.* **105**, 2415–2420 (2008).
72. Zhao, H. *et al.* DNA damage signaling, impairment of cell cycle progression, and apoptosis triggered by 5-ethynyl-2'-deoxyuridine incorporated into DNA. *Cytom. Part A* **83**, 979–988 (2013).
73. GmbH, R. D. & GmbH, R. D. Exposure to continuous bromodeoxyuridine (BrdU) differentially affects cell cycle progression of human breast and bladder cancer cell lines. *Cell Prolif.* **49**, 195–206 (2004).
74. Ferro, A. *et al.* Blue intensity matters for cell cycle profiling in fluorescence DAPI-stained images. *Lab. Investig.* **97**, 615–625 (2017).
75. Spring, K. R. & Davidson, M. W. MicriscopuU: Introduction to Fluorescence Microscopy. Available at: <https://www.microscopyu.com/techniques/fluorescence/introduction-to-fluorescence-microscopy>. (Accessed: 6th October 2017)
76. Rottenfusser, R., Wilson, E. E. & Davidson, M. W. Zeiss: Introduction to Fluorescence Microscopy. Available at: <http://zeiss-campus.magnet.fsu.edu/articles/basics/fluorescence.html>. (Accessed: 6th October 2017)
77. Abramowitz, M. & Davidson, M. W. Olympus: Fluorescence Filters. Available at: <https://www.olympus-lifescience.com/es/microscope->

resource/primer/techniques/fluorescence/filters/. (Accessed: 7th October 2017)

78. Dailey, M. E., Shaw, S. L., Swedlow, J. E. & Andrews, P. D. Zeiss: Live-Cell Imaging. Available at: <http://zeiss-campus.magnet.fsu.edu/articles/livecellimaging/techniques.html>. (Accessed: 6th October 2017)
79. Combs, C. A. Fluorescence Microscopy: A concise guide to Current Imaging Methods. *Curr. Protoc. Neurosci.* 1–19 (2010). doi:10.1002/0471142301.ns0201s50.Fluorescence
80. Toomre, D. K., Langhorst, M. F. & Davidson, M. W. Zeiss: Introduction to Spinning Disk Microscopy. Available at: <http://zeiss-campus.magnet.fsu.edu/articles/spinningdisk/introduction.html>.
81. Weinstein, G. D. & Mooney, K. M. Cell Proliferation Kinetics in the Human Hair Root. *J. Invest. Dermatol.* **74**, 43–46 (1980).
82. Kloepper, J. E. *et al.* Methods in hair research: how to objectively distinguish between anagen and catagen in human hair follicle organ culture. *Exp. Dermatol.* 305–312 (2009).
83. Oh, J. W. *et al.* A guide to studying human hair follicle cycling in vivo. *136*, 34–44 (2016).
84. Panteleyev, A. A. Putting the human hair follicle cycle on the map. *J. Invest. Dermatol.* **136**, 4–6 (2016).
85. Reed, N. D. & Manning, D. D. Long-term maintenance of normal human skin on congenitally athymic (nude) mice. *Proc. Soc. Exp. Biol. Med.* **143**, 350–353 (1973).
86. Cui, J., Shen, L. Y. & Wang, G. C. Role of hair follicles in the repigmentation of vitiligo. *The Journal of investigative dermatology* **97**, 410–6 (1991).
87. CellnTec: Cnt-07 media. Available at: <http://cellntec.com/products/cnt-07/>. (Accessed: 17th October 2017)
88. Hilmi, A. B. M. *et al.* A simple culture method for epithelial stem cells derived from human hair follicle. *Cent. Eur. J. Biol.* **8**, 432–439 (2013).
89. Vinay, K. & Dogra, S. Stem cells in vitiligo: Current position and prospects. *Pigment Int.* **1**, 8–12 (2014).
90. Mohanty, S., Kumar, A., Dhawan, J., Sreenivas, V. & Gupta, S. Noncultured extracted hair follicle outer root sheath cell suspension for transplantation in vitiligo. *Br. J. Dermatol.* **164**, 1241–1246 (2011).
91. El-Zawahry, B. M. *et al.* Effect of Procedural-Related Variables on Melanocyte–Keratinocyte Suspension Transplantation in Nonsegmental Stable Vitiligo. *Dermatologic Surg.* **43**, 226–235 (2017).
92. Geel, N. Van, Goh, B. K., Wallaeys, E., Keyser, S. De & Lambert, J. A review of non-cultured

- epidermal cellular grafting in vitiligo Full Text Introduction Methods for Data Collection. **4**, 17–19 (2011).
93. Krüger, C. & Schallreuter, K. U. A review of the worldwide prevalence of vitiligo in children/adolescents and adults. *Int. J. Dermatol.* **51**, 1206–1212 (2012).
94. Parsad, D. A New Era of Vitiligo Research and Treatment. *J. Cutan. Aesthet. Surg.* **6**, 63–64 (2013).
95. Suzuki, T., Fujikura, K., Higashiyama, T. & Takata, K. DNA Staining for Fluorescence and Laser Confocal Microscopy. *J. Histochem. Cytochem.* **45**, 49–53 (1997).
96. ThermoFisherScientific. Fluorescence SpectraViewer. Available at: <http://www.thermofisher.com/pt/en/home/life-science/cell-analysis/labeling-chemistry/fluorescence-spectraviewer.html>. (Accessed: 18th May 2017)
97. Zeiss Axio Observer. Available at: [https://imm.medicina.ulisboa.pt/facility/bioimaging/doku.php?id=zeiss\\_cell\\_observer](https://imm.medicina.ulisboa.pt/facility/bioimaging/doku.php?id=zeiss_cell_observer).
98. CellProfiler Software. Available at: [cellprofiler.org](http://cellprofiler.org). (Accessed: 23rd May 2017)
99. CellProfiler Manual. Available at: <http://cellprofiler.org/manuals/current/>. (Accessed: 22nd May 2017)
100. Pereira, P. D. *et al.* Quantification of cell cycle kinetics by EdU (5-ethynyl-2'-deoxyuridine)-coupled-fluorescence-intensity analysis. *Oncotarget* **8**, 40514–40532 (2017).
101. Fiji.
102. T. Ferreira, W. R. ImageJ User Guide IJ 1.46r. *IJ 1.46r* 185 (2012). doi:10.1038/nmeth.2019
103. Wand, M. Data-Based Choice of Histogram Bin Width. *51*, 59–64 (1997).
104. Abramowitz, M., Herman, B., Murphy, D. B. & Davidson, M. W. Olympus: Anatomy of the Fluorescence Microscope. Available at: <https://www.olympus-lifescience.com/en/microscope-resource/primer/techniques/fluorescence/anatomy/fluoromicroanatomy/>. (Accessed: 7th October 2017)
105. Langan, E. A., Philpott, M. P., Kloepffer, J. E. & Paus, R. Human hair follicle organ culture: theory, application and perspectives. *Exp. Dermatol.* **24**, 903–911 (2015).
106. Danilenko. Growth factors and cytokines in hair follicle development and cycling recent insights from animal models and the potentials for clinical therapy. *Mol. Med. Today* (1996).



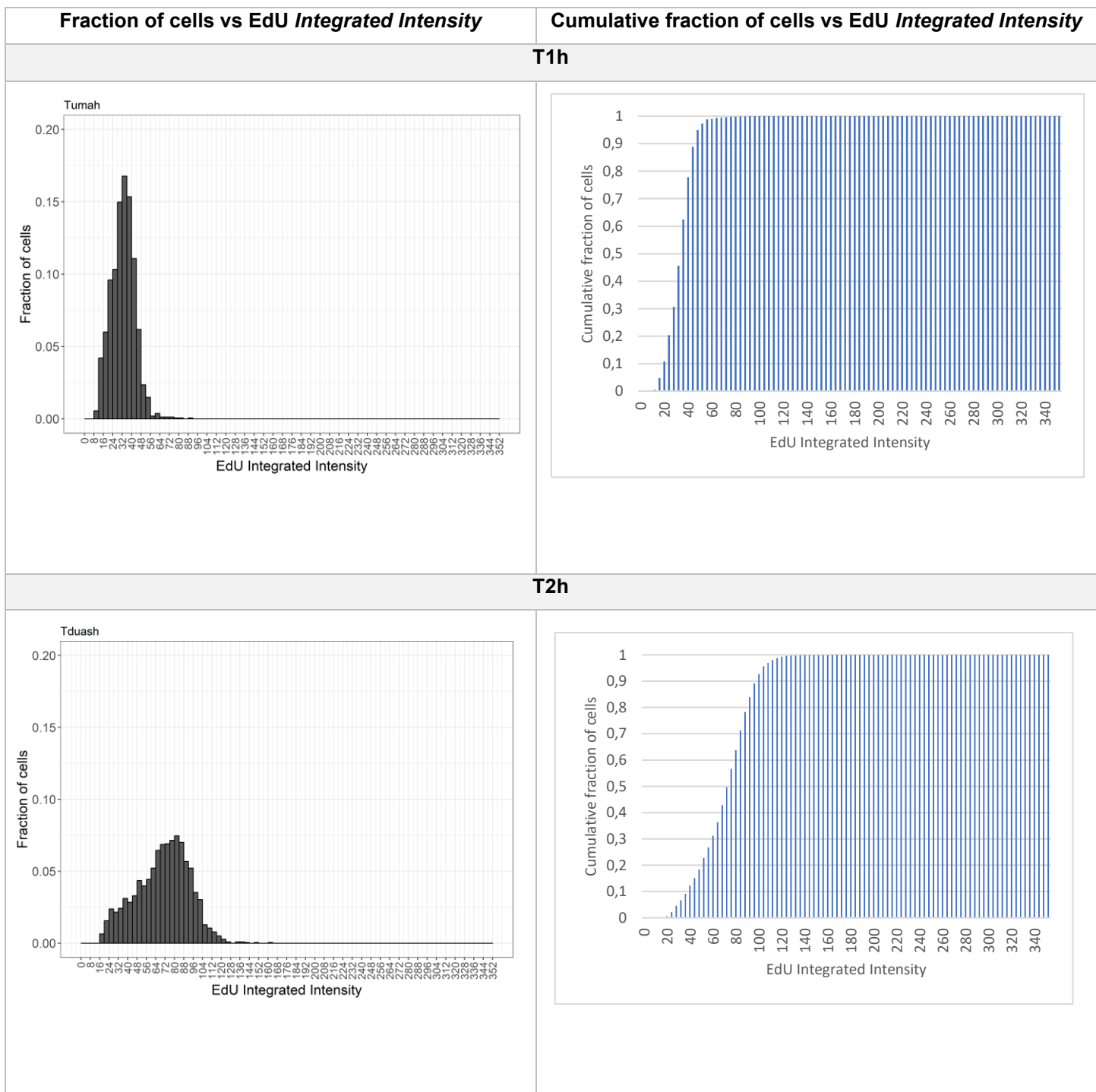
# VII. Annexes

**Table VII-1: Values of threshold selected on Preliminary Project for DAPI or Hoechst channel (whole DNA stain) and Alexa 488 Channel**

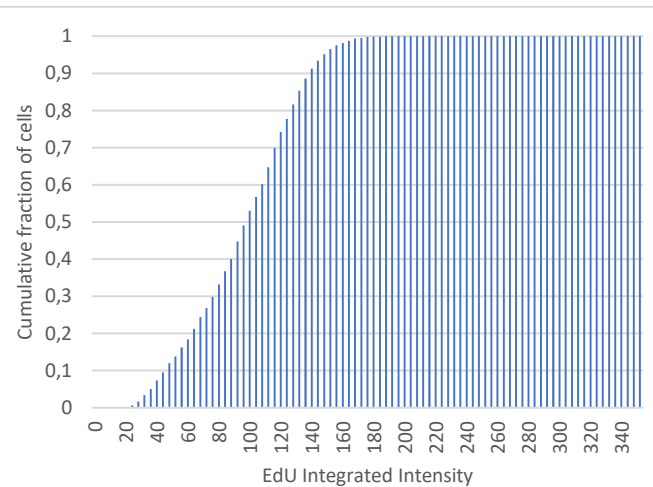
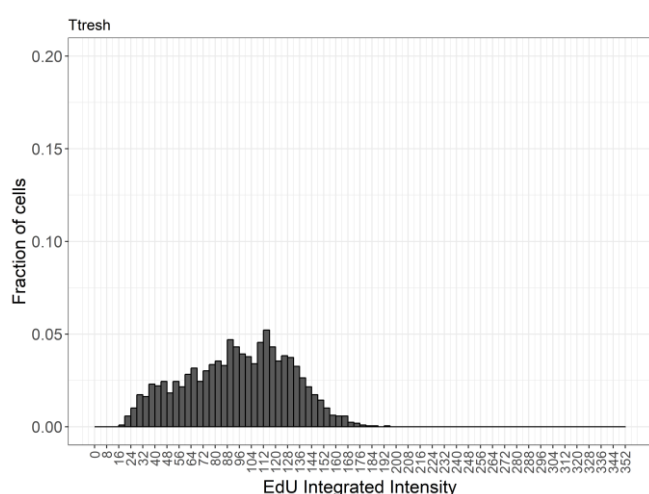
Experiments	Time-points	Whole DNA stain channel	Alexa 488 Channel
7	1	0,0025	0,0025
	2	0,003	0,003
	3	0,006	0,006
	4	0,006	0,006
	5	0,0075	0,0075
	6	0,0085	0,0085
	7	0,0095	0,0095
	8	0,01	0,01
8	1	0,035	0,0025
	2		0,0045
	3		0,005
	4		0,006
	5		0,007
	6		0,008
	7		0,009
	8		0,01
9	1	0,03	0,005
	2		0,005
	3		0,013
	4		0,013
	5		0,016
	6		0,016
	7		0,016
	8		0,016
11	1	0,035	0,0025
	2		0,005
	3		0,007
	4		0,008
	5		0,009
	6		0,009
	7		0,009
	8		0,009
	9		0,009
	10		0,009
12	1	0,05	0,003
	2		0,005
	3		0,006
	4		0,008
	5		0,008
	6		0,01

	7		0,011
	8		0,012
	9		0,013
	10		0,014

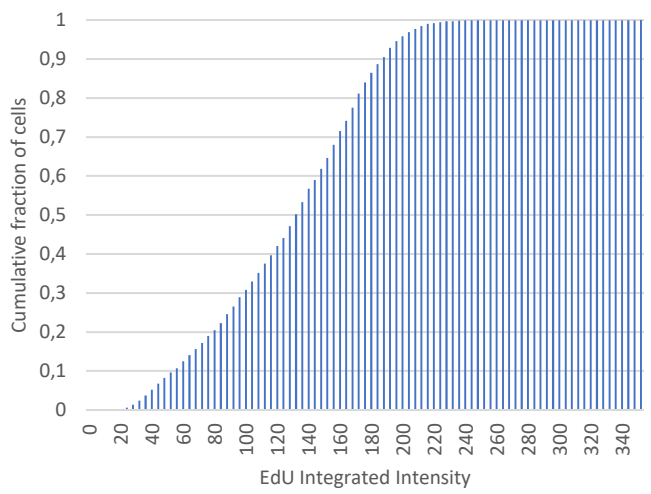
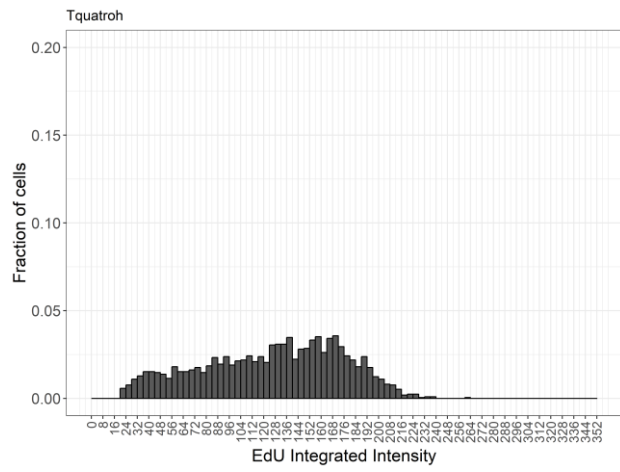
**Table VII-2: Graphs fraction of cells vs EdU Integrated Intensity and cumulative fraction of cells vs EdU Integrated Intensity of each time-point (T1h-T8h), Experiment 9.**



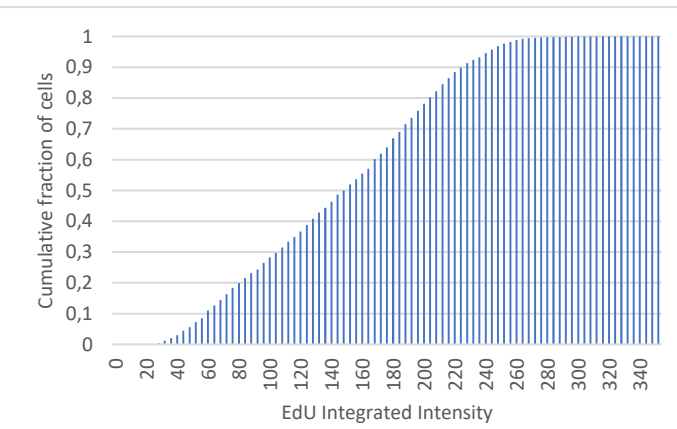
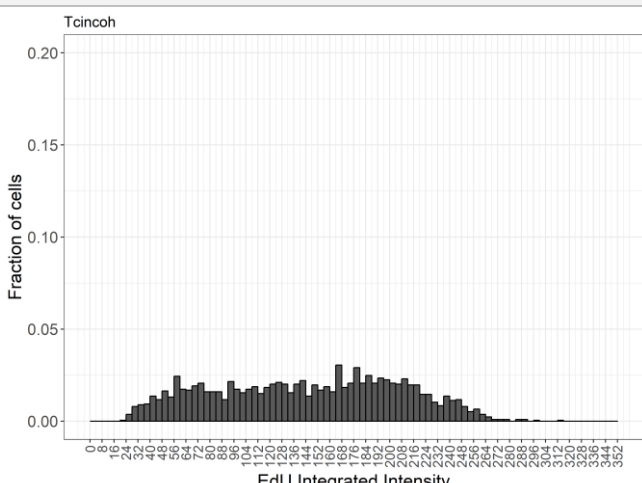
### T3h



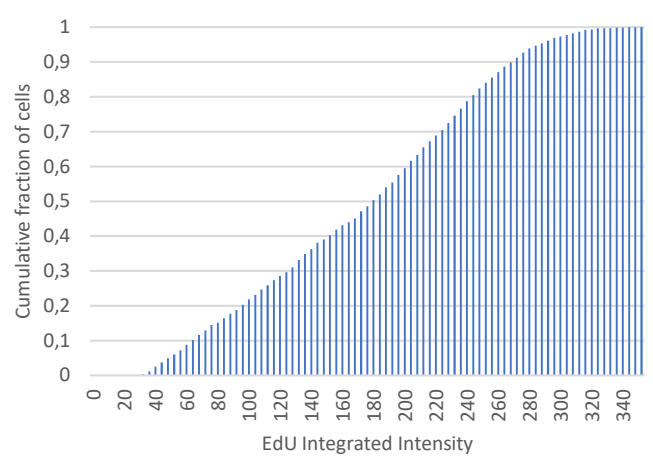
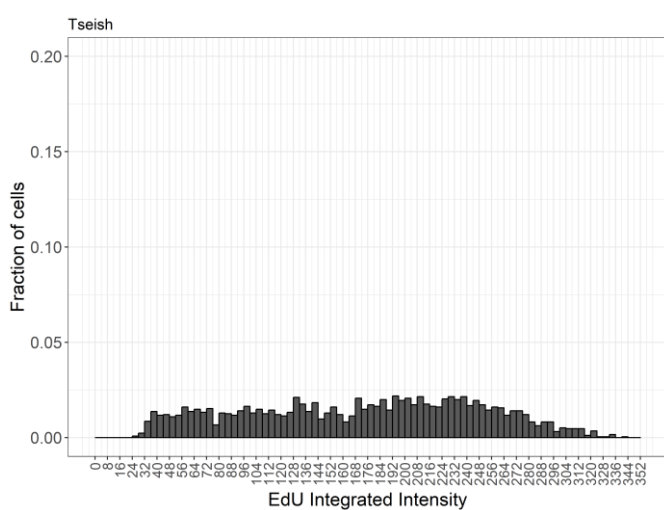
### T4h



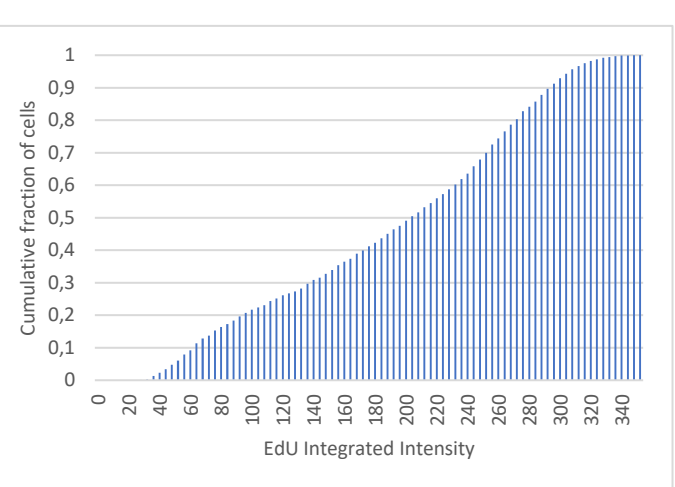
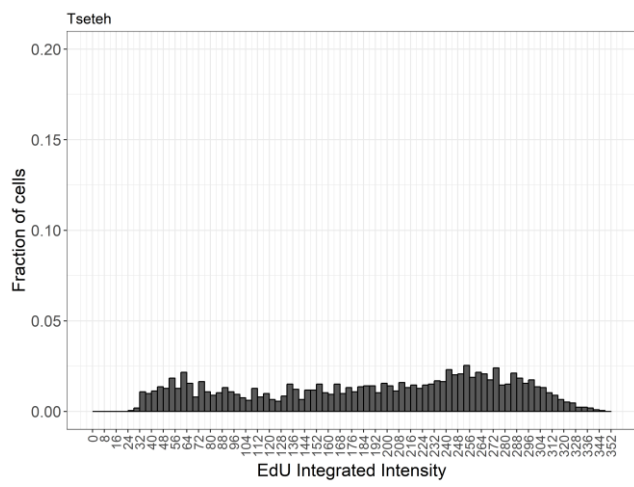
### T5h



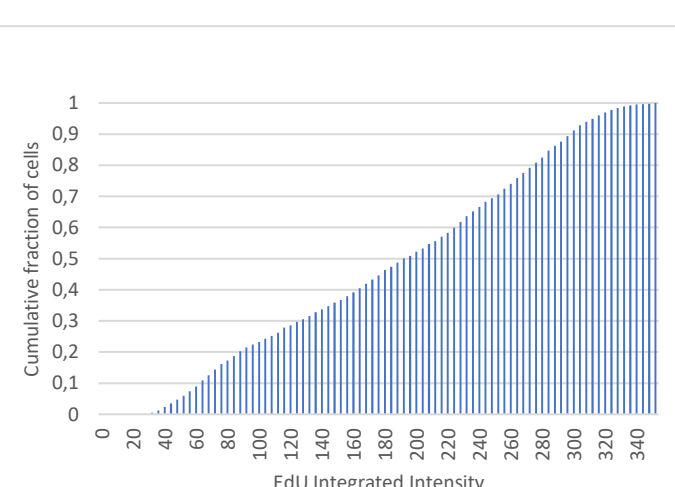
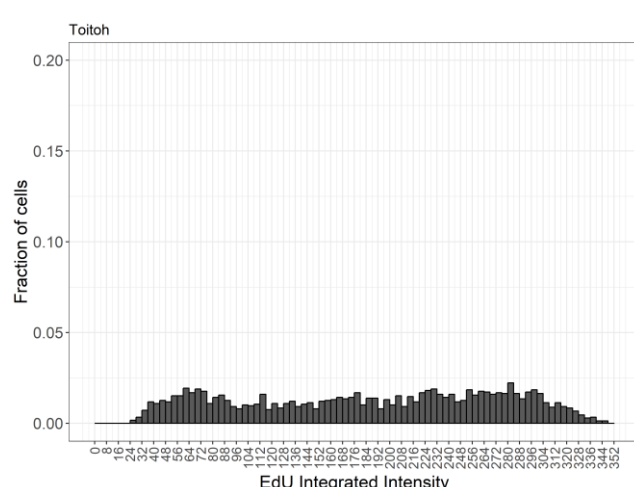
**T6h**



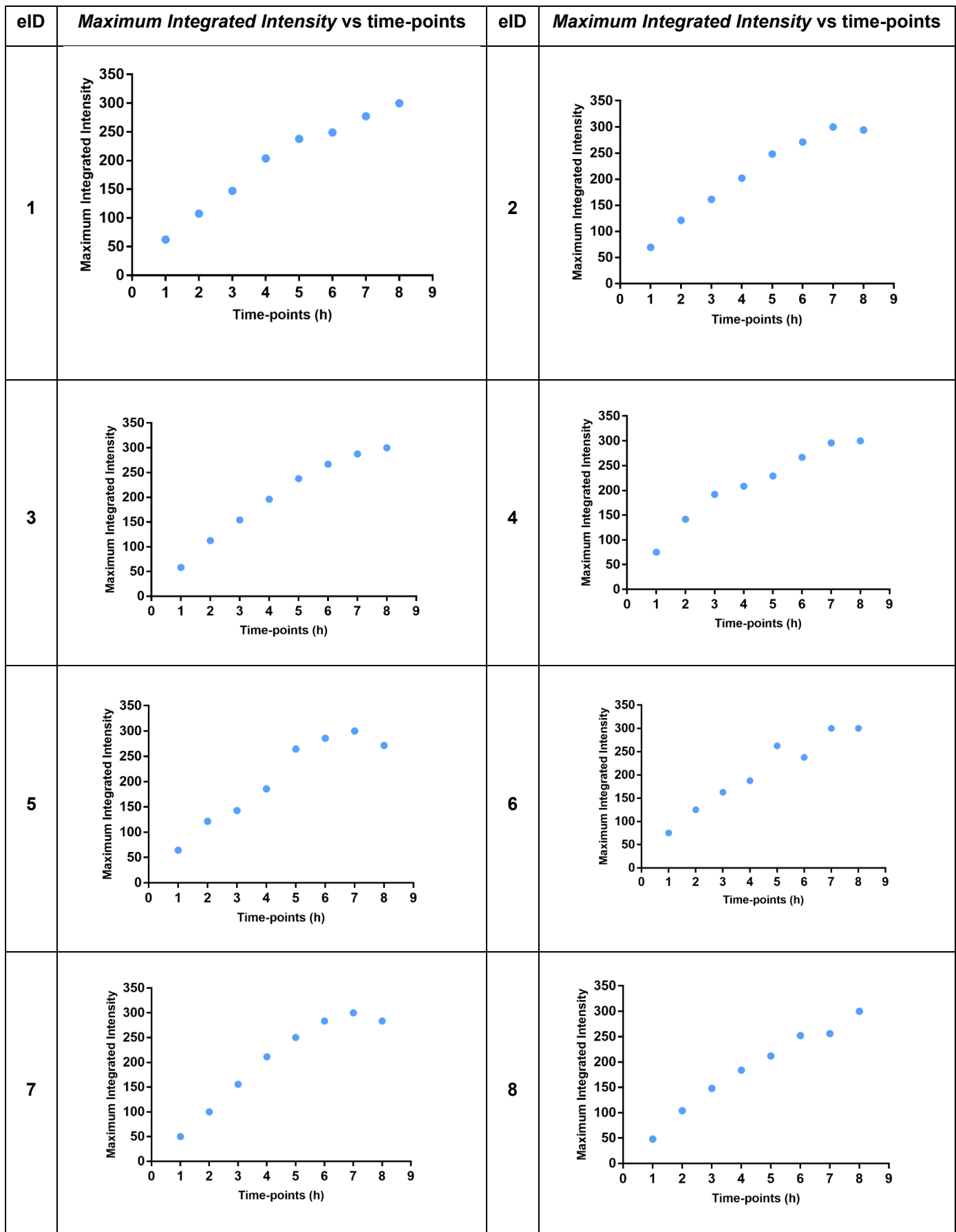
**T7h**

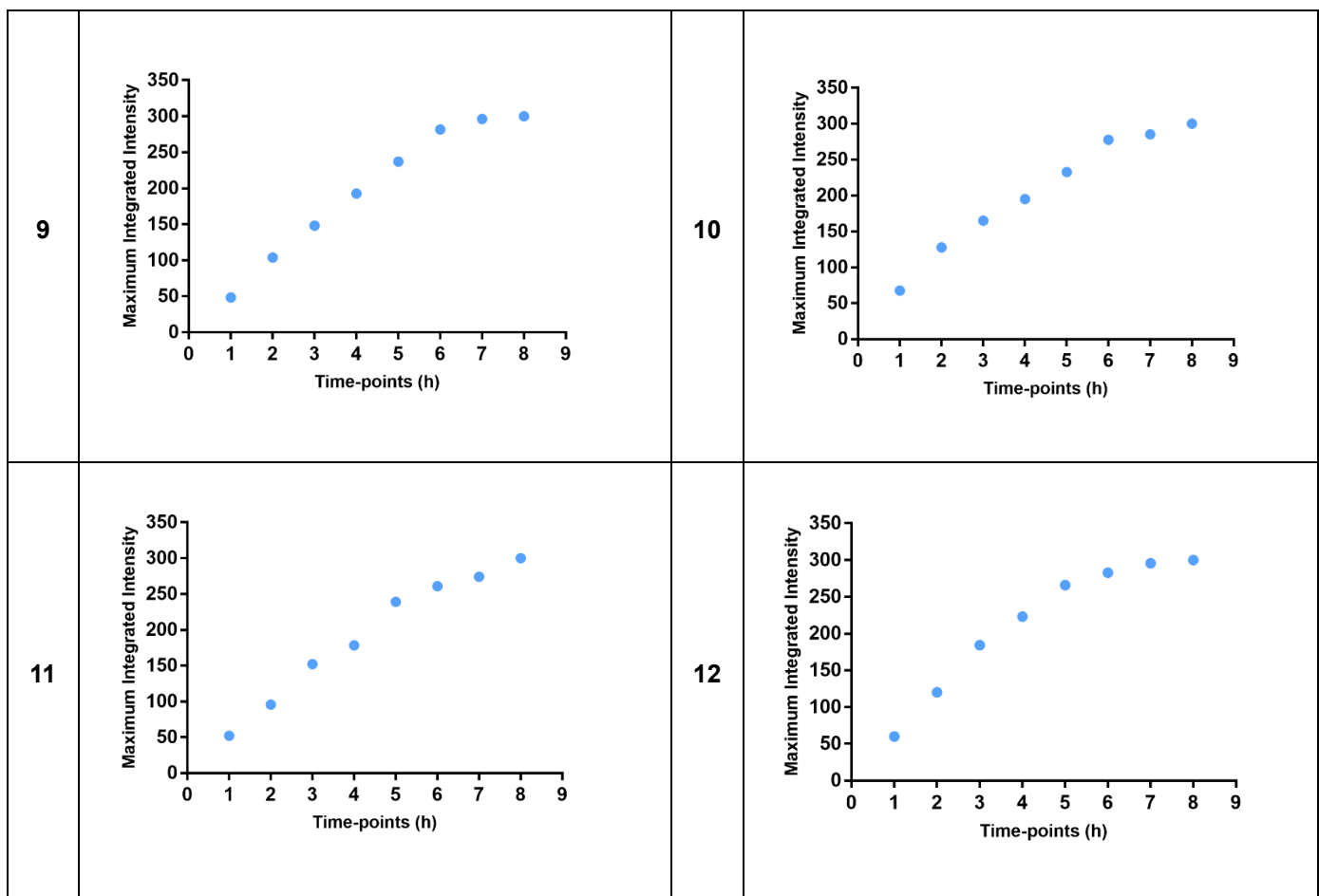


**T8h**

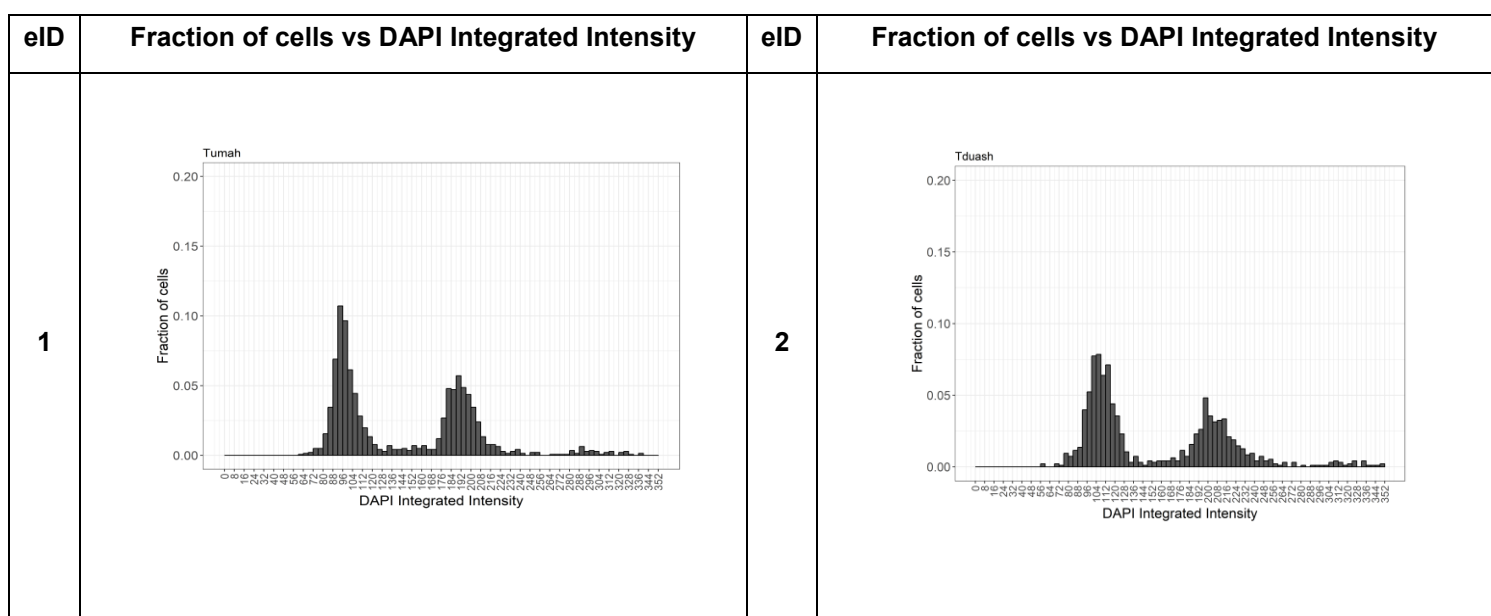


**Table VII-3: Graphs Maximum Integrated Intensity vs time-points of each experiment (1-12).**





**Table VII-4: Histograms (Fraction of cells vs DAPI Integrated Intensity) of each time-point (T1h-T8h), experiment 8**



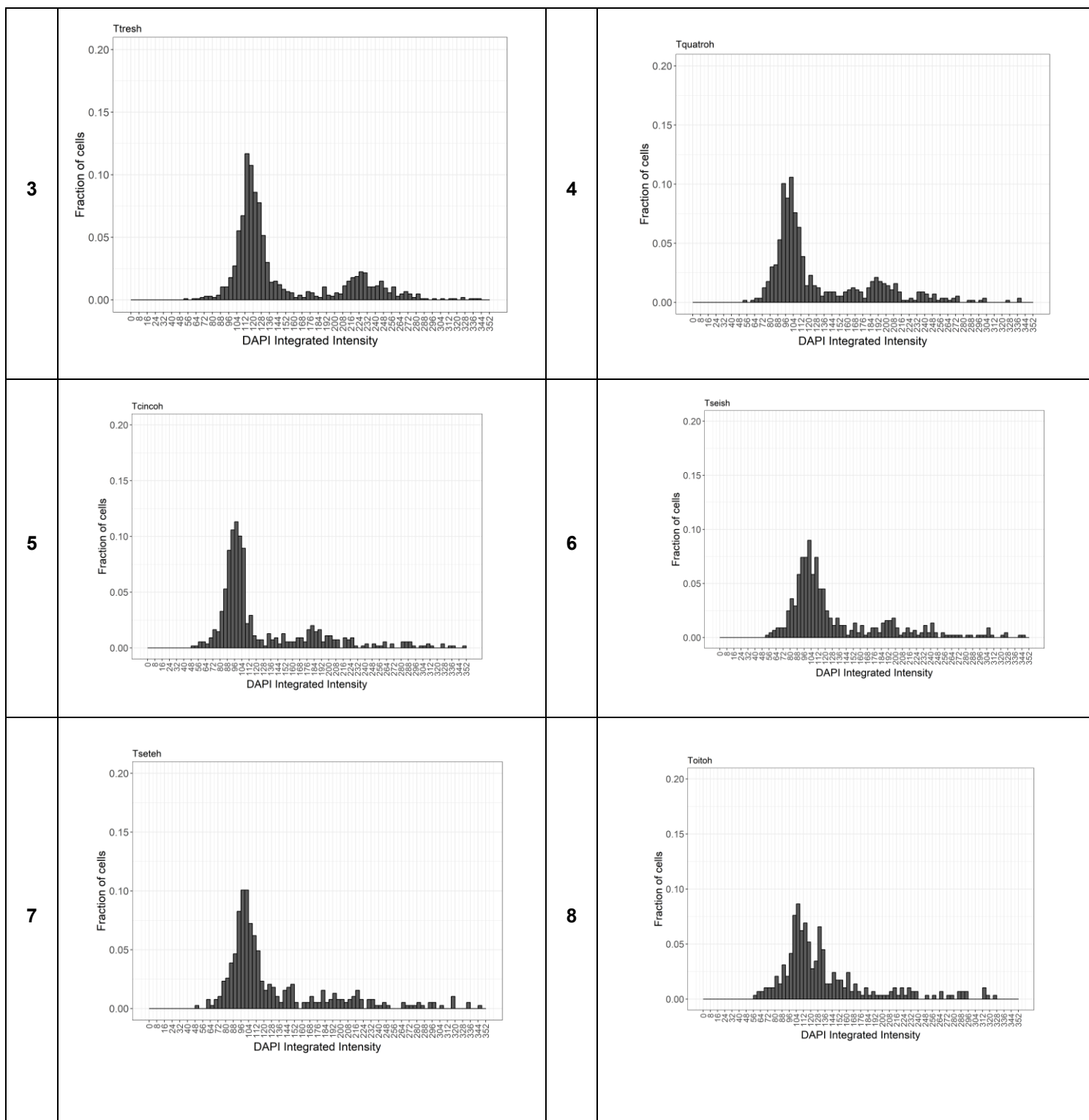


**Table VII-5: Histograms (Fraction of cells vs DAPI Integrated Intensity) of time-point (T9h-T10h), experiments 11 and 12**

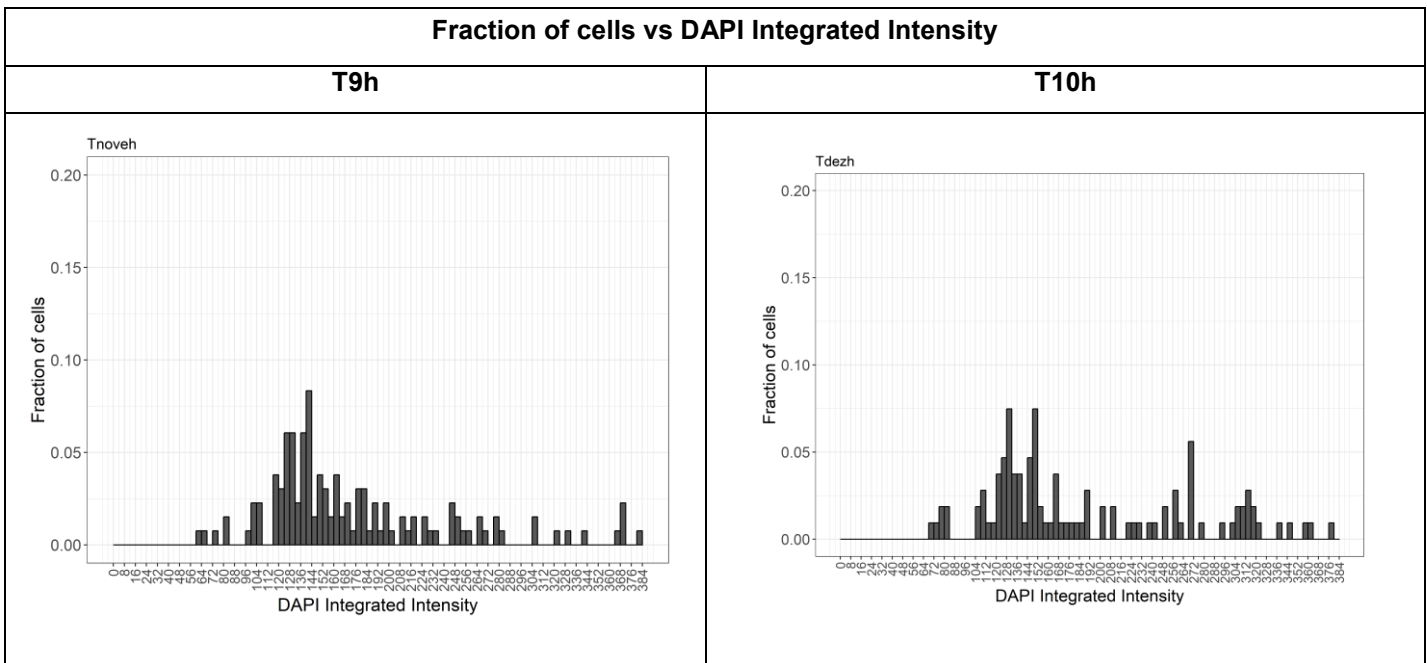


**Table VII-6: Range of G1 and G2 intensities selected based on histograms.**

Experiment 7									
<b>T1h</b>	G1: 40-64 G2: 92-120	<b>T2h</b>	G1: 40-64 G2: 96-116	<b>T3h</b>	G1: 44-68 G2: 100-124	<b>T4h</b>	G1: 44-68 G2: 100-124	<b>T5h</b>	G1: 40-76 G2: 96-120
<b>T6h</b>	G1: 40-76 G2: 96-120	<b>T7h</b>	G1: 40-76 G2: 96-120	<b>T8h</b>	G1: 40-76 G2: 96-120				
Experiment 8									
<b>T1h</b>	G1: 80-116 G2: 176-208	<b>T2h</b>	G1: 92-128 G2: 188-220	<b>T3h</b>	G1: 100-136 G2: 208-248	<b>T4h</b>	G1: 80-118 G2: 180-216	<b>T5h</b>	G1: 80-120 G2: 180-216
<b>T6h</b>	G1: 80-120 G2: 180-216	<b>T7h</b>	G1: 80-120 G2: 180-216	<b>T8h</b>	G1: 80-120 G2: 180-216				
Experiment 9									
<b>T1h</b>	G1: 84-140 G2: 172-244	<b>T2h</b>	G1: 72-112 G2: 156-196	<b>T3h</b>	G1: 80-120 G2: 168-208	<b>T4h</b>	G1: 88-128 G2: 176-216	<b>T5h</b>	G1: 96-136 G2: 184-224
<b>T6h</b>	G1: 96-136 G2: 184-224	<b>T7h</b>	G1: 88-128 G2: 176-216	<b>T8h</b>	G1: 88-128 G2: 176-216				
Experiment 11									
<b>T1h</b>	G1: 116-160 G2: 236-296	<b>T2h</b>	G1: 116-160 G2: 236-296	<b>T3h</b>	G1: 136-192 G2: 256-336	<b>T4h</b>	G1: 116-160 G2: 236-296	<b>T5h</b>	G1: 128-168 G2: 224-288

<b>T6h</b>	G1: 128-168 G2: 224-288	<b>T7h</b>	G1: 116-160 G2: 236-296	<b>T8h</b>	G1: 116-160 G2: 236-296	<b>T9h</b>	G1: 116-160 G2: 236-296	<b>T10h</b>	G1: 116-160 G2: 236-296
<b>Experiment 12</b>									
<b>T1h</b>	G1: 144-208 G2: 296-376	<b>T2h</b>	G1: 144-204 G2: 296-376	<b>T3h</b>	G1: 152-232 G2: 328-408	<b>T4h</b>	G1: 128-192 G2: 292-376	<b>T5h</b>	G1: 140-200 G2: 288-368
<b>T6h</b>	G1: 128-168 G2: 224-288	<b>T7h</b>	G1: 128-192 G2: 292-376	<b>T8h</b>	G1: 128-192 G2: 292-376	<b>T9h</b>	G1: 128-192 G2: 292-376	<b>T10h</b>	G1: 128-192 G2: 292-376

**Table VII-7: Sum-up of values used to estimate the percentage of G1 and G2 cells in total population.**

Experiments	Time-points	Total Population	N_EdU-	%G1_peak	%G2_peak	NG1	NG2	%G1_tp	%G2_tp
7	1	4008	1946	57,45	28,83	1118	561	27,89	14,00
	2	3656	1538	58,39	26,33	898	405	24,56	11,08
	3	3773	1507	63,97	19,11	964	288	25,55	7,63
	4	3717	1246	67,90	11,08	846	138	22,76	3,71
	5	3937	1221	72,32	7,62	883	93	22,43	2,36
	6	4219	1038	67,63	6,94	702	72	16,64	1,71
	7	4093	858	66,78	4,78	573	41	14,00	1,00
	8	3679	559	54,03	9,30	302	52	8,21	1,41
8	1	3194	1430	47,27	32,73	676	468	21,16	14,65
	2	2621	965	48,08	24,87	464	240	17,70	9,16
	3	2920	1076	61,52	15,24	662	164	22,67	5,62
	4	2169	569	59,58	13,36	339	76	15,63	3,50
	5	2346	552	63,95	9,24	353	51	15,05	2,17
	6	2899	450	57,78	9,11	260	41	8,97	1,41
	7	2569	387	60,21	8,01	233	31	9,07	1,21
	8	2855	290	47,24	5,17	137	15	4,80	0,53
9	1	3522	1634	47,72	34,21	779,71	558,92	22,14	15,87
	2	4170	1774	54,79	25,80	972,04	457,67	23,31	10,98
	3	4019	1657	52,85	21,22	875,71	351,63	21,79	8,75
	4	3382	1160	55,53	12,66	644,10	146,81	19,04	4,34
	5	3304	1053	58,08	8,18	611,62	86,17	18,51	2,61
	6	3790	1051	59,36	5,41	623,87	56,81	16,46	1,50
	7	3010	656	54,20	5,83	355,57	38,26	11,81	1,27
	8	3094	490	48,79	7,97	239,08	39,06	7,73	1,26
11	1	3173	1450	30,96	35,32	448,94	512,15	14,15	16,14
	2	3239	1269	37,39	23,36	474,45	296,42	14,65	9,15
	3	2352	744	42,45	23,54	315,82	175,16	13,43	7,45
	4	3040	976	60,32	12,64	588,68	123,32	19,36	4,06
	5	3054	787	46,51	8,89	366,00	70,00	11,98	2,29
	6	3489	704	41,37	9,57	291,28	67,36	8,35	1,93
	7	3352	437	42,48	10,02	185,65	43,80	5,54	1,31
	8	3241	271	39,07	8,96	105,87	24,28	3,27	0,75

	9	2546	127	43,48	9,42	55,22	11,96	2,17	0,47
	10	2897	111	38,74	14,41	43	16	1,48	0,55
12	1	2952	1184	40,71	35,73	482	423	16,33	14,33
	2	2827	1046	41,11	29,25	430	306	15,21	10,82
	3	3827	1134	46,38	18,08	526	205	13,74	5,36
	4	3088	961	55,15	13,42	530	129	17,16	4,18
	5	3005	751	55,39	10,12	416	76	13,84	2,53
	6	2499	531	58,00	10,17	308	54	12,32	2,16
	7	2139	323	57,59	11,15	186	36	8,70	1,68
	8	3089	258	53,88	8,53	139	22	4,50	0,71
	9	2905	180	41,67	10,00	75	18	2,58	0,62
	10	2860	130	46,15	7,69	60	10	2,10	0,35

**Table VII-8: Number of identified cells (EdU positive) along time-points (rows), for each set of input images (columns; 2, 4, 6, 9, 12 and 18 images).**

	2 images	4 images	6 images	9 images	12 images	18 images
0	0	0	0	0	1	3
1	70	185	268	331	447	581
2	183	387	570	749	1045	1642
3	257	368	556	821	1147	1769
4	164	362	502	796	1135	1657
5	219	542	761	1148	1554	2135
6	313	662	985	1294	1732	2735
7	242	599	808	1291	1796	2695
8	455	1108	1503	1953	2507	3991

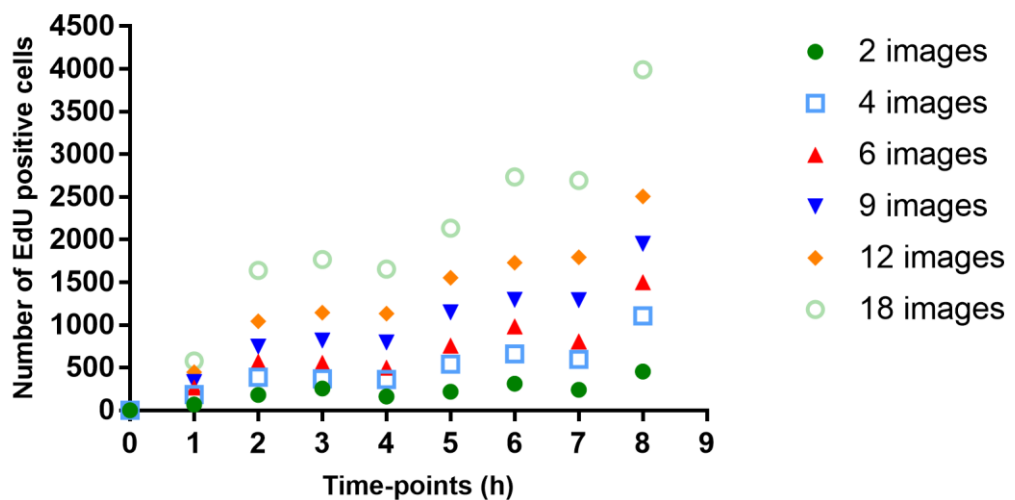
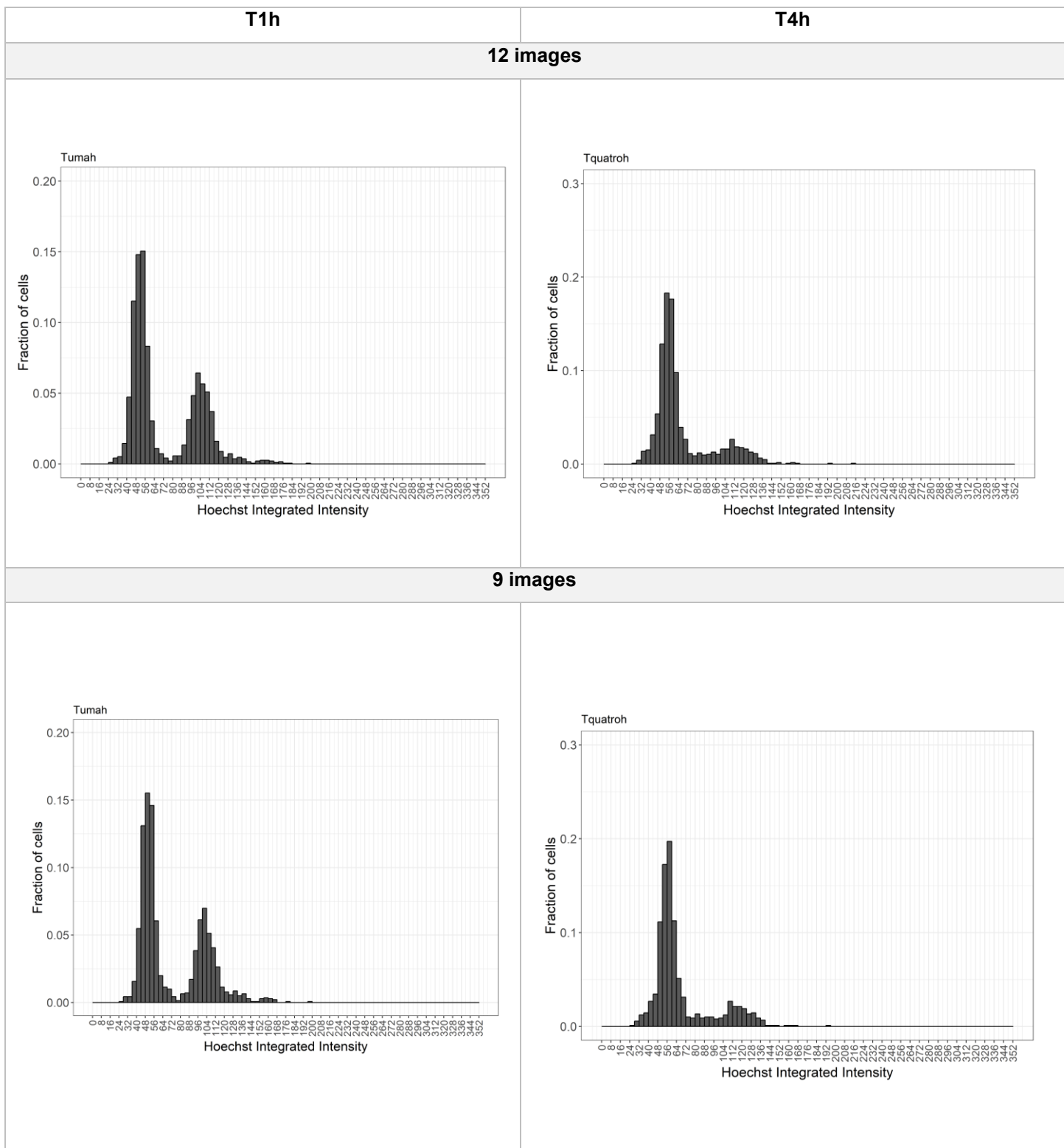
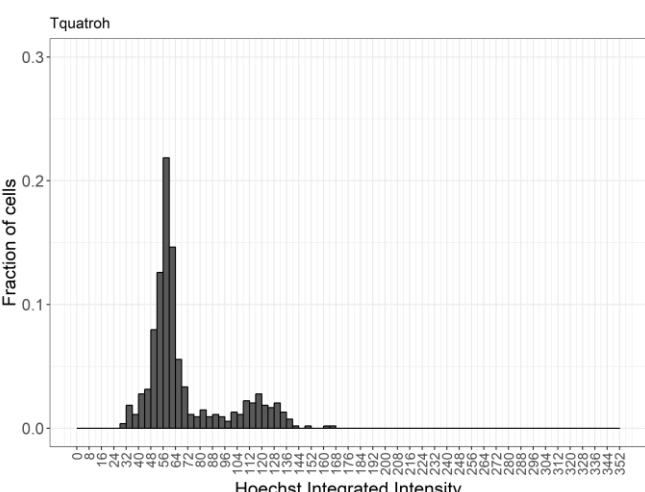
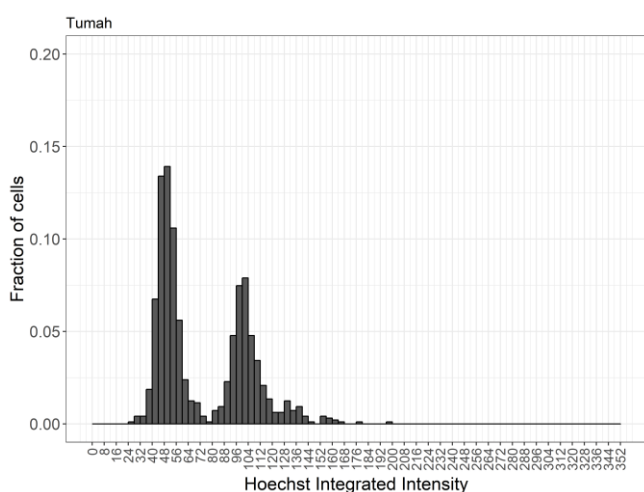


**Figure VII-1: Graph containing the number of identified cells (EdU positive) along time-points, for each set of input images (2, 4, 6, 9, 12 and 18 images).**

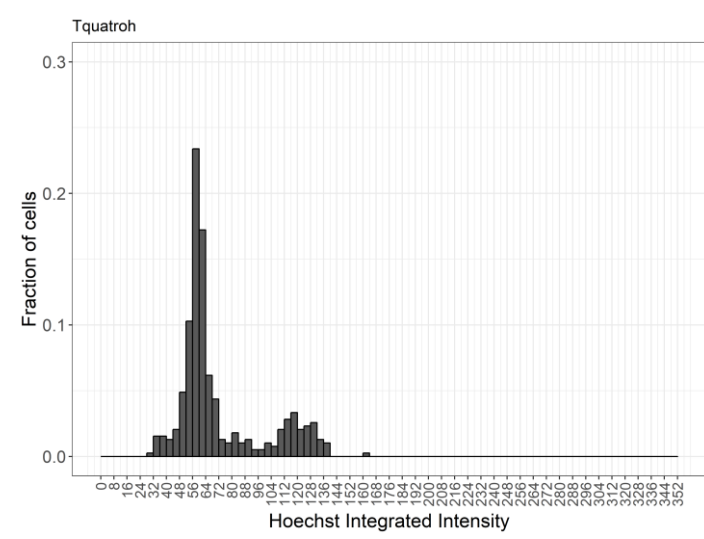
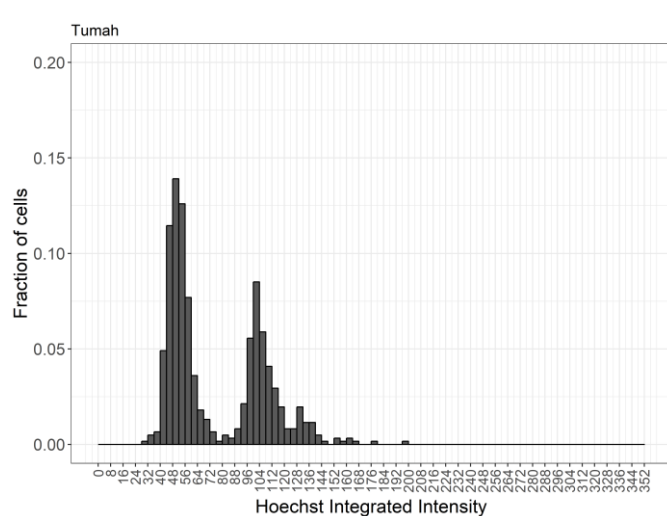
**Table VII-9: Histograms (Fraction of cells vs Hoechst Integrated Intensity) of experiment 7 (T1h and T4h), for different sets of input images (2, 4, 6, 9, 12 images)**



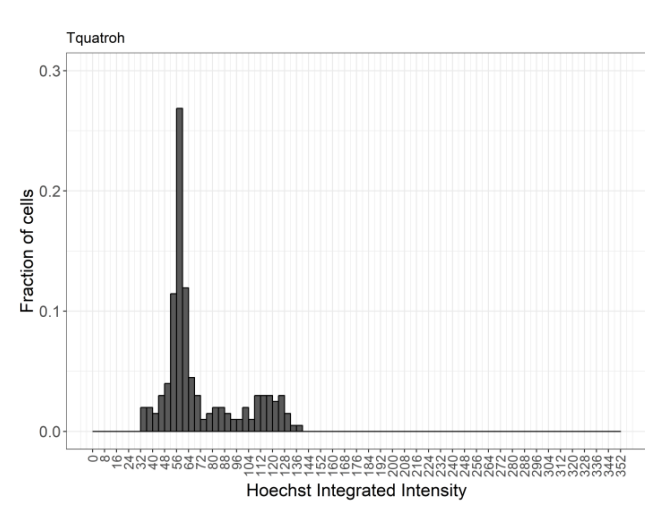
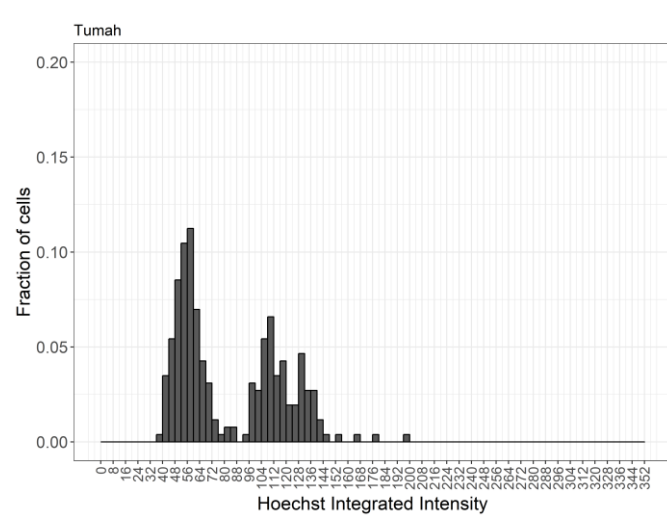
### 6 images



### 4 images



### 2 images



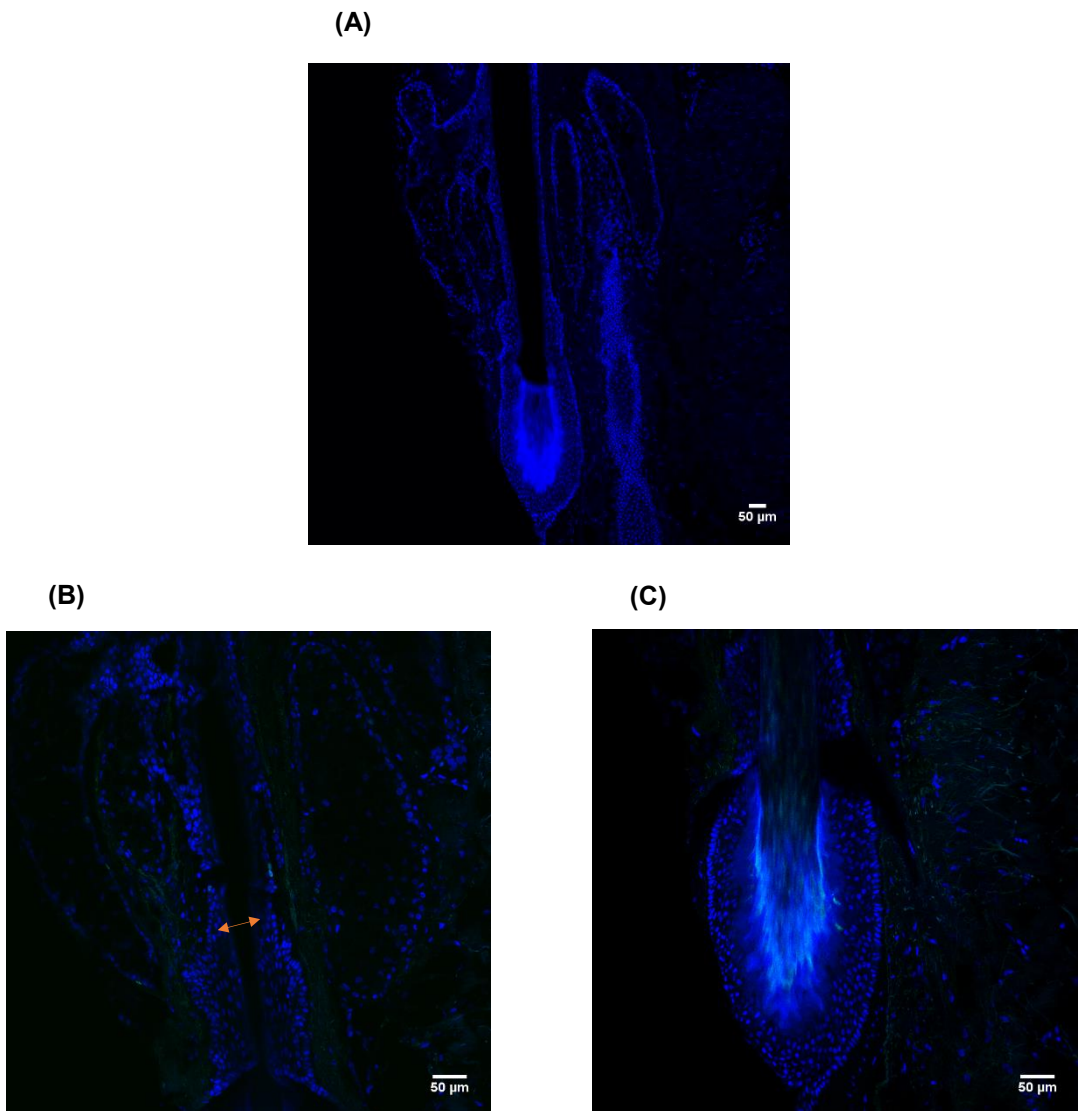


**Figure VII-2:** Images of hair follicle in catagen obtained on Confocal Point-Scanning Microscope Zeiss LSM 710. (A) represents the overall structure (channel: DAPI). (B) and (C) represent bulge and bulb respectively (multichannel acquisition: DAPI and Alexa 488). The red crosses identifies EdU-positive cells. Scale: 50μm

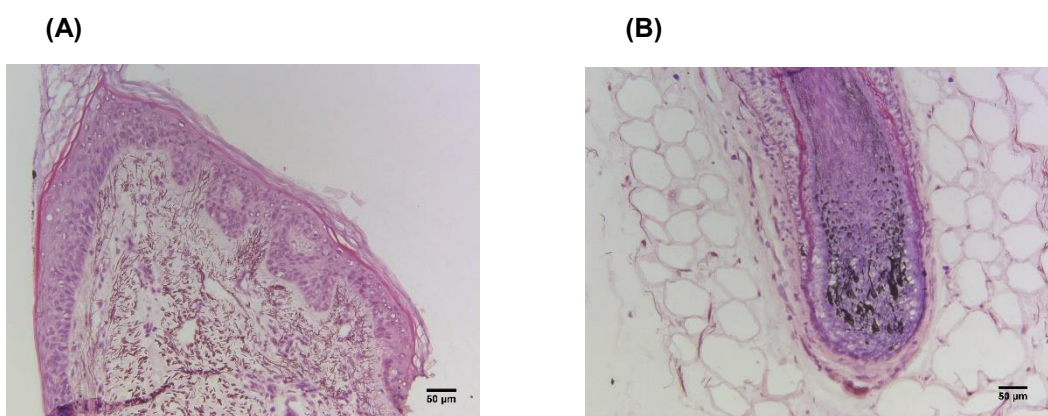


**Figure VII-3:** Images of (A) epidermis and (B) HF bulge stained with Gimsa and acquired using the brightfield microscope Leica DM2500. B) represents a para-sagittal section of HF which do not contain dermal papilla. The melanin is present in matrix Scale: 50μm.

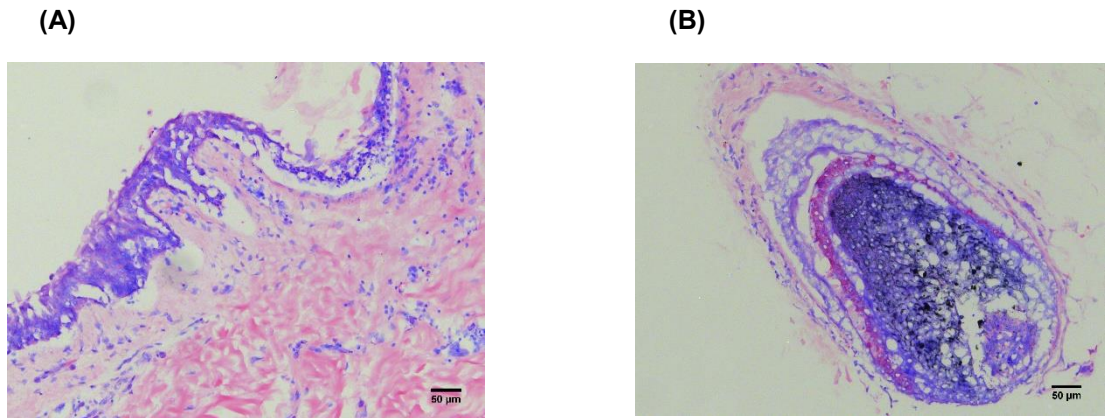


**Figure VII-4:** Images of HFs stained with Gimsa and acquired using the brightfield microscope Leica DM2500. They present the endothelium destroyed by SDS when any protective structure as acrylamide was used. (A) epidermis; (B) bulb. Scale: 50μm.

**Table VII-10:** Images exported from cell counter plugin of Fiji, where different types of counters (with different colors) were used to distinguish quantified areas and channels.

HF regions	DAPI	Alexa 488
Bulb		
Sub-bulge		

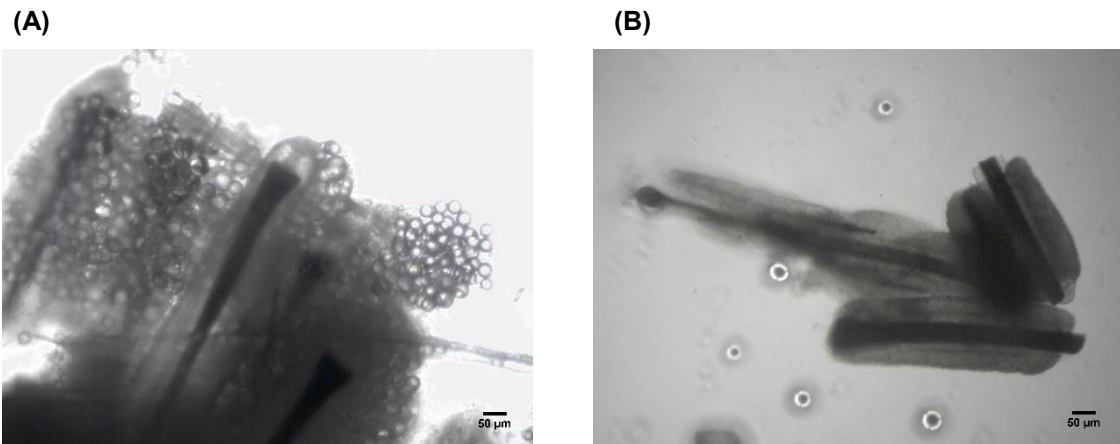


**Figure VII-5:** Human hair follicles before (A) and after (B) collagenase/dispase incubation. Images acquired using the Phase Contrast microscope Zeiss Primovert.

```

 In selection  Match case  Whole word  Regex  Wrap
26
27 setwd('D:/Maria/Tese/CellProfiler+R/PROJECT2_DNAstain/9 - E005sc/3/output_parte2')
28
29 ##### CLEAR WORKING SPACE AND LOAD THE REQUIRED PACKAGES
30
31 rm(list = ls())
32
33 library(data.table)
34 library(ggplot2)
35 library(stringr)
36
37 ## SET HISTOGRAM GRAPHICAL AND BINNING PARAMETERS
38
39 E005SC.max <- 352 # Set the maximum value for the Integrated Intensity histogram and binning table
40
41 E005SC.binwidth <- 4 # Set the bin width for the Integrated Intensity histogram and binning table
42
43 # Set the width and height in inches for the Integrated Intensity histogram.png file
44 E005SC.width <- 8
45 E005SC.height <- 6
46
47 dir.create('R_output') # Create the R_output subdirectory in the working directory
48
49 # Set levels for timepoint column. The names of the timepoints appearing in the
50 # vector must exactly match the ones previously set in the filenames.
51 treat.Levels <- c('Tresh')
52
53 ##### READ AND PROCESS CP2 ANALYSIS RESULTS FROM NUCLEI.TXT FILE
54 # Read the .txt file containing the CP2 cell cycle analysis results:
55 nuc.dt <- fread('Nuclei.txt')
56
57 # Format: DAPI_{timepointName}_{FieldNumber}.tif. The timepoint name should
58 # include only letters and the field name only numbers.
59 split.pat <- '/E005SC_{[A-Z,a-z]}{[0-9]+}_R3D\\.{tif$}'
60
61 # Extract the timepoint and field number from the filenames
62 <
63
64
65
66
67
68
69
70
71
72
73
74
75
76
77
78
79
80
81
82
83
84
85
86
87
88
89
90
91
92
93
94
95
96
97 <
98
99
100
101
102
103
104
105
106
107
108
109
110
111
112
113
114
115
116
117
118
119
120
121
122
123
124
125
126
127
128 <

```

Figure VII-6: R code